A New Class of Adsorptive Photocatalysts for Enhanced Adsorption and

Destruction of 4-chlorophenol and perfluorooctanoic acid

By

Fan Li

A dissertation submitted to the Graduate Faculty of
Auburn University
in partial fulfillment of the
requirements for the Degree of
Doctor of Philosophy

Auburn, Alabama
December 14, 2019

Keywords: concentration-&-destroy, titanate, adsorption, photocatalytic
degradation, 4-chlorophenol, perfluorooctanoic acid

Copyright 2019 by Fan Li

Approved by

Dongye Zhao, Chair, Elton and Lois Endowed Professor of Civil Engineering
Mark O. Barnett, Professor of Environmental Engineering
Natalie Cápiro, Assistant Professor of Civil Engineering
Xinyu Zhang, Associate Professor of Chemical Engineering
Yucheng Feng, Professor of Crop, Soil and Environmental Sciences

Abstract

Four novel Ti-based adsorptive photocatalysts, namely titanate nanosheets (TNS), graphene grafted titania/titanate nanosheets (G/TNS), activated carbon modified titanate nanotubes (TNTs@AC), and iron doped, activated carbon supported anatase nanotubes (Fe/TNTs@AC), were synthesized based on commercial activated carbon and titanium oxide. The composite materials were thoroughly characterized, and tested for enhanced adsorption and photocatalytic degradation of some persistent organic pollutants (POPs) such as 4-chlorophenol (4-CP) and perfluorooctanoic acid (PFOA). The photocatalysts were synthesized through a one-step facial alkaline hydrothermal process   followed by proper metal doping and calcination. While titanate (TNS or TNTs) alone acted as an cation exchanger for taking up various metal cations such as Pb^{2+} and Cd^{3+}, AC-modified TNTs was able to effectively adsorb hydrophobic contaminants such as 4-CP, and upon deposition of iron (hydr)oxide, Fe/TNTs@AC was able to effectively adsorb PFOA. All materials offered excellent photocatalytic activity under UV irradiation/solar light. Taking advantage of the unique properties of these composites, we developed an unique "Concentrate-and-Destroy" strategy for treating trace concentrations of POPs. First, low concentrations of a contaminant is pre-concentrated on photoactive sites on the material surface, then the pre-concentrated contaminant is destroyed upon UV or solar light irradiation. The effective photocatalytic degradation also regenerates the material, allowing for repeated uses of the material without involving expensive chemical

ii

regeneration and without generating the process waste residual as is the case for

conventional adsorption processes.

Overall, the adsorptive photocatalysts and the new "Concentrate-&-Destroy"

strategy represent a significant advancement in the treatment of POPs. The new materials

hold the promise to treat some of the most challenging contaminants in water in a more

cost-effective manner.

Acknowledgments

I would like to deeply thank my academic advisor, Dr. Dongye Zhao, for providing me with the opportunity to purse my Ph.D. degree under his guidance. I really appreciate his support, continuous encouragement, patience and guidance in accomplishing my career goals.

I am also equally thankful to my graduate committee members: Dr. Mark Barnett, Dr. Clifford Lange, Dr. Natalie Cápiro, Dr. Xinyu Zhang, and the university reader Dr. Yucheng Feng for their valuable time and insightful advice on various research problems.

I would like to thank my wife, Yu Mei, for empowering me with unconditional love, infinite patience, deep sympathy, and absolute trust. I would also like to express my sincere gratitude and appreciation to my parents. Without your love, support, and encouragement, I would not have been capable of completing this study.

Then, I would like to thank all my lab mates and technician for keeping a wonderful and decent research environment. I also want to thank all my friends who inspired me with your kindness and knowledge, especially Dr. Wen Liu, Dr. Xinquan Cheng, Dr. Zongsu Wei, Dr. Ke He, Dr. Melissa Boersma, and Mr. Tao Ye. Additionally, I wish to express my gratitude to Strategic Environmental Research and Development Program (SERDP) (ER18–1515) and the Auburn University IGP program for financial support of my study and research at Auburn University.

At last, I would like to thank my Lord of life, Jesus Christ. You walk with me day and night. You bring me peace and joy. You show me wisdom and truth. Worthy is your name. You deserve all the praise!

Table of Contents

viii

List of Figures

xii

List of Table

Chapter 1. Introduction

1.1. Backgroud

Industrial wastewater offers substantial threats to the eco-system and human health.

Persistent organic pollutant (POPs) is the category of pollutants which people are concerned

about more and more. As a probe chemical which were used in experiments, occurrence and

distribution of 4-Chlorophenol (4-CP) in the environment were massively reported. 4-CP was

mainly used as material of dye and medical synthesis. Also, 4-CP was used as refined mineral oil

solvent. Meanwhile, 4-CP was a hazardous compound which would be harmful to skin and eye

and toxic to aquatic life. Thus, the study of 4-CP removal would be very necessary. Regularly,

advanced oxidation processes (AOPs) degradation and carbon adsorption were two main

methods that water plant applied to remove 4-CP. But both methods are still facing several

technical problems such as carbon regeneration, low concentration pollutant residual, and high

cost.

In recent year, per- and polyfluoroalkyl substances (PFAS), as an emerging pollutant

category, attract more and more research communities' attention. PFASs have been world widely

used as surfactants, fire-fighting foams, metal coating materials and pesticides in people's daily

life for almost half century. In years of 2000 and 2001, people realized that PFASs were

massively released in the environment during the period of industrial production and application

of PFASs. After the fourth meeting of the Parties of the Stockholm Convention, most common

used long-chain PFASs (PFCA has more than 6 C or PFSA has more than 4 C, e.g.

perfluorooctanoic acid) were added into list of persistent organic pollutants (POPs). Although

3M company, the major global producer, began to cease producing these long-chain PFASs from year of 2002 and gradually used some short-chain PFASs (e.g. PFBA and PFBS, C2-6 PFCA and C2-4 PFSA) as alternates, the market demands were still increasing. At same time, other companies, especially in China and India, were keeping producing both long-chain and short-chain PFASs. As the consequences, the short-chain PFASs production and application began to increase rapidly. After more than one decade of studies, research community found that the distribution of PFASs are becoming much wider than it used to be. In terms of regional distribution, east China, India, coastal area of U.S. and Canada, and drainage basin of River Rhine in EU were major areas where were greatly affected by the PFASs issue. In terms of medium of distribution in the environment, people can clearly see a spreading trend that from land/solid waste to groundwater/river, then to atmosphere and ocean, even the snow/ice in polar area. Perfluorooctanoic acid (PFOA), as one of the most frequently detected PFAS, was used as the probe chemical for PFASs removal study.

After decades of research and application, people found that using photocatalytic degradation method would be a promising process for 4-CP removal. Ti based nanomaterials (e.g. nano-TiO2 and titanate nanotubes) had been proved to be an effective photocatalyst. Thus, my study basically focused on optimization of Ti based nanomaterial and development of more sustainable and more effective methods for removal of chlorophenols and other similar organic pollutants.

1.2. Overall objectives:

a) Simultaneously remove multiple contaminants (e.g. heavy metal and POPs) from

wastewater through adsorption and photocatalysis to achieve clean water for reuse.

b) Understanding the photocatalytic degradation process of POPs including degradation pathway, intermediates, and final products so that we can make sure we did not release more toxic compound into eco-system.

c) Enhance the photocatalytic activity to achieve better POPs degradation and switch UV light to solar light as light source to achieve lower energy consumption.

d) Find a way to utilize photocatalysis technique in real drinking water/wastewater treatment plant.

1.3. Hypothesis

a) To enhance photocatalysis activity, transition metal (e.g. cobalt, nickel, and iron) and other semiconductor (e.g. carbon, CNT, and graphene) composition can be utilized to prevent photo-generated electron-hole recombination by rapidly transfer of electron.

b) To enhance photocatalytic activity, the crystal structure of Ti-based catalyst should be optimized to achieve narrowed energy band gap (usually larger crystallite size structure) so that catalyst can absorb/response light with wider wavelength range (from UV light to visible light).

c) To promote photocatalytic degradation of POPs, the contact between catalysis and target pollutants would be. critical factor. The longer contact time and shorter distance would enhance photo-redox reaction before oxidants and reductants quench.

d) To utilize the photocatalytic technique in real drinking/wastewater treatment plant, pre-concentration is need since light cannot travel long distance in water. Thus, reuse of sorbent

3

(heterogeneous photocatalyst), following "concentrate-&-destroy" approach, will be a possible solution.

Chapter 2. Simultaneous removal of Cr(VI) and 4-chlorophenol through photocatalysis by titanate nanosheets: Synergetic promotion effect and self-doping

TNS was able to simultaneously remove both Cr(VI) and 4-CP in binary systems through enhanced photocatalytic reduction of Cr(VI) to Cr(III) and oxidation of 4-CP. More than 99% of Cr(VI) and 4-CP were removed within 120 min through photocatalysis by TNS at pH 7 in the binary system. Moreover, the removal rates in binary system were much higher than in the single-solute systems, with the apparent first-order rate constants for Cr(VI) and 4-CP being 3.1 and 2.6 times higher, respectively, compared to those in the single-solute systems. TEM and XRD analyses indicated that TNS was composed of anatase and titanate, of which anatase acted as the photocatalysis center and titanate was the primary adsorption site. The synergetic effect in the binary system was due to simultaneous photo-reduction of Cr(VI) and photo-oxidation of 4-CP, which effectively facilitated separation of the electron-hole pairs. As the reaction proceeds, reduced Cr(III) was adsorbed by TNS, which further broadened the light absorbing range of TNS and resulted in more photo-excited more reactive oxygen species (ROS).

2.1. Introduction

Industry-induced wastewaters exhibit great threats to ecosystems and human health. Generally, components of wastewaters are complicated, with co-existence of multiple contaminants, such as heavy metals and organic pollutants (Correia et al. 1994, Edwards and Kjellerup 2013, He et al. 2011), leading to difficult treatment by technical processes. For

example, Cr(VI) and chlorinated phenols (CPs) are found to coexist in tannery wastewaters (Tripathi and Garg 2014, Tripathi et al. 2011). Cr(VI) is a common heavy metal with high toxicity, resulting from its carcinogenicity and teratogenicity (Costa 1997). While CPs are emerging containments and persistent organic pollutants (POPs), which widely exist in wastewaters originating from industrial processes of tanning, manufacturing preservatives, pesticides and antifouling agents (Crittenden et al. 1997, Sorokin et al. 1995, Sze and McKay 2012). Although lots of techniques like adsorption, membrane, bio-process, direct chemical oxidation and advanced oxidation processes (AOPs, like Fenton reaction), are used to solve the Cr(VI) or/and CPs pollution problems (Ahmaruzzaman 2008, Aksu and Yener 2001, Barrera-Diaz et al. 2012, He et al. 2010, Huang et al. 2012, Quintelas et al. 2006, Scott and Ollis 1995, Yin et al. 2014), the processes are somewhat not so efficient, low-cost and simple to operation. Moreover, methods which can complete remove of Cr(VI) through reduction and degrade of CPs are undoubtedly better than only adsorption or phase separation. Therefore, development of promising and high-efficient technologies for treatment of combined polluted wastewaters is an urgent need in the environmental remediation area.

Photocatalysis using titanium related nanomaterials (including TiO_2 and titanate) seems a good choice for solving the nerve-wracking problem, considering reduction of Cr(VI) and completely degradation of CPs (Liu et al. 2014a, Qiu et al. 2012). TiO_2 is the most common photocatalyst for degradation of organic compounds, of cause, including CPs (Cheng et al. 2007, Daghrir et al. 2013, Ku et al. 1996). In recent years, titanate nanomaterials (especially titanate nanotubes, TNTs) have drawn great interests due to their good ion-exchange property, leading to

wide use as metal cations adsorbents (e.g. Pb(II), Cd(II), Cr(III), radionuclides, etc.) (Bavykin et al. 2006, Kasuga et al. 1999, Liu et al. 2013c, Liu et al. 2016, Sun and Li 2003, Wang et al. 2013b, Xiong et al. 2011). However, pure titanate possesses two main defects: (1) low adsorption capacity for metal anions (like Cr(VI) and As(V)) and organics (Liu et al. 2013a, Niu et al. 2013, Wang et al. 2013a, Wang et al. 2015), and (2) weak photocatalytic activity because of the immediate recombination of photo-generated electron-hole pairs (Liu et al. 2014a, Liu et al. 2015, Yu et al. 2006). Therefore, combination of TiO_2 and titanate is an available method for simultaneous removal of both heavy metals and organics through initial photocatalysis and subsequent adsorption. Namely, Cr(VI) can be photo-reduced to Cr(III) by TiO_2 and then adsorbed by titanate, and organic compound (e.g. CPs) can be directly photo-degraded in the meanwhile. Previous studies paid attention to the photocatalytic reduction of Cr(VI) by TiO_2 or combination of TiO_2 and TNTs (Liu et al. 2014a, Qiu et al. 2012), and to the photocatalytic degradation of CPs by single TiO_2 (Cheng et al. 2007, Crittenden et al. 1997), but little information is on the simultaneous removal of Cr (including both Cr(VI) and Cr(III)) and CPs through photocatalysis and adsorption, and moreover, the undergoing mechanism in this complex system is also lacking.

Based on the above scenarios, we proposed a facile one-step method to synthesize a composite nanomaterial, TNS, composed of TiO_2 and titanate, which shows both good adsorptive and photocatalytic performance. The prepared TNS were used to simultaneously remove coexisting Cr(VI) and 4-CP. The main objectives of this study are to: (1) prepare a promising titanate based material which can simultaneous removal of both Cr(VI) and 4-CP; (2)

achieve the   goal of complete removal of Cr(VI) and Cr(III); (3) clearly elucidate the mechanisms for photocatalytic removal of Cr(VI) and 4-CP, and possible different mechanisms with co-existence of these two pollutants; and (4) test the reusability of the synthesized material.

2.2. Materials and methods

2.2.1. Chemicals

All chemicals used in this study were of analytical grade or better and used without further purification. Nano-scale TiO_2 (anatase, 99.7%, mean size of 25 nm) were used as precursor to synthesis TNS, which was purchased from Sigma-Aldrich (St. Louis, MO, USA). NaOH (purity > 98.0%) and absolute ethanol (also used to synthesize TNS) were obtained from Acros Organics (Fair Lawn, NJ, USA). Analytical $K_2Cr_2O_7$, $CrCl_3 \cdot 6H_2O$ and 4-CP were purchased from Acros Organics (Fair Lawn, NJ, USA). Deionized (DI) water (Millipore Co., 18.2 MΩ·cm) was used to prepare all the solutions.

2.2.2. Preparation and characterization of TNS

TNS were synthesized through a short-cut hydrothermal method (Li et al., 2015). Specifically, 0.8 g of TiO_2 powder was added into 80 mL of 8 mol/L NaOH solution and stirred for 12 h. After that, the mixture was transferred into a Teflon reactor with stainless steel coating, and then heated at 130 °C for 3 h. Then the suspension was washed with DI water until the supernatant was neutral. Finally, TNS were dispersed with ethanol and obtained after dried at 80 °C for 4 h.

Morphology of TNTs were got on a Tecnai F30 FEG transmission electron microscopy (TEM, FEI, USA), operating at 300 kV. Crystal phase of the sample was conducted on a

Dmax/2400 X-ray diffractometer (XRD, Rigaku, Japan) with Cu $K\alpha$ radiation source ($\lambda = 1.5418$ Å) at a scan rate (2θ) of 4°/min. Specific surface area of TNS was got on an ASAP 2010 adsorption apparatus (Micromeritics, USA) through nitrogen adsorption-desorption isotherms at -196 °C according to the Brunauer-Emmett-Teller (BET) theory. Nitrogen adsorption volume at a relative pressure (P/P_0) of 0.99 was used for the measurement. Zeta potentials of the materials under various pH were detected using a Nano-ZS90 Zetasizer (Malvern Instruments, UK), to determine the point of zero charge (pH_{PZC}). UV-vis diffuse reflectance spectra (DRS) of the materials were conducted on a UV-2400 spectrophotometer (Shimadzu, Japan), and reflectance measurements were converted to adsorption spectra using the Kubelka-Munk function.

2.2.3. Adsorption of Cr and 4-CP by TNS

Adsorption of Cr(VI), Cr(III) and 4-CP by TNS were tested under different solution pH, respectively. With 5 mg/L of Cr or 4-CP (50 mL) mixed with 0.025 g TNS, the pH of the mixture was adjusted fro0m 2 to 9 using dilute HCl or NaOH solution. After shaken (200 rpm, 25±2 °C) for 4 hours and filtered through 0.22 μm polytetrafluoroethylene (PTFE) membrane, the Cr or 4-CP concentration in the supernatant was determined.

Total Cr concentration was measured on an inductively coupled plasma-mass (ICP-MS, X Series II, Thermo Fisher Scientific, USA), while Cr(VI) concentration determined through a dinitrodiphenyl carbazide spectrophotometric method at 540 nm on a UV-vis spectrophotometer (UV1800, Shimadzu, Japan). Cr(III) concentration was calculated as the difference between total Cr and Cr(VI). 4-CP concentration was measured using a high-performance liquid

chromatography (HPLC, Agilent 1200 Series, USA) equipped with a C18 column (SB-AQ, 5 μm, 4.6 mm × 250 mm) and a diode array detector (DAD). Mixture of methanol (HPLC grade, BDH, USA) and ultrapure water (v/v of 60:40) was used as mobile phase. Samples were injected into the instrument at a flow rate of 1 mL/min and were analyzed at an UV absorbance wavelength of 280 nm. Adsorption capacity (q_e) and removal efficiency (R) of Cr or 4-CP is calculated by:

$$q_e = \frac{(C_0 - C_e)V}{m} \qquad (2\text{-}1)$$

$$R = \frac{(C_0 - C_e)}{C_0} \times 100\% \qquad (2\text{-}2)$$

where q_e (mg/g) is the adsorption capacity of Cr or 4-CP on TNS at equilibrium; C_0 and C_e (mg/L) is the initial and equilibrium concentration of Cr or 4-CP, respectively; V (L) is the total volume of the solution, and m (g) is the mass of added TNS.

2.2.4. Photocatalysis of Cr(VI) and 4-CP by TNS

Photocatalytic experiments were carried out in a cuboid quartz reactor (total volume of 300 mL, 5×5×12 cm) as shown in Fig.S1. A high-pressure mercury lamp (150 W, 365 nm) was used as the UV light source, which was placed beside the reactor in parallel and cooling air was injected to maintain the reaction temperature of 25±2 °C. The UV light density in the reactor center was measured as 2.5 mW/cm². Light was turned on to start the photocatalytic reaction immediately after Cr or 4-CP was mixed with TNS. The photocatalytic experiment was carried out through the following two scenarios: (1) Photocatalysis of single Cr(VI) and 4-CP. 5 mg/L of Cr(VI) or 4-CP (200 mL in total volume) was mixed with 0.5 g/L TNS respectively to start the

9

photocatalytic reaction. (2) Photocatalysis of coexisting Cr(VI) and 4-CP. With a fixed Cr(VI)

concentration of 5 mg/L, coexisting 4-CP concentration varied as 2.5, 5 and 10 mg/L to conduct

the photocatalytic reaction. All the photocatalytic experiments were conducted at pH 5, 7 and 9,

respectively. Blank photocatalytic experiments were also carried out without addition of

materials while with light on.

Langmuir-Hinshelwood (L-H) model is introduced to describe the photocatalysis process,

which is expressed as (Rizzo et al. 2009, Satterfield 1970, Valente et al. 2006) :

$$-\frac{dC_t}{dt} = r = k_r \frac{K_L C_t}{1 + K_L C_t} \qquad (2\text{-}3)$$

in which r (mg/(L·min)) is the photocatalytic reaction rate, k_r (mg/(L·min)) is the

photocatalytic reaction rate constant, and K_L (L/mg) is the Langmuir constant for adsorption.

Regarding the conditions of $K_L C_t \ll 1$, $t = 0$ and $C_t = C_0$, Equation (3) can be simplified as the

first-order kinetic model:

$$\ln(C_0 / C_t) = k_1 t \qquad (2\text{-}4)$$

where k_1 (min^{-1}) is the first-order apparent rate constant.

The degradation intermediates of 4-CP were also determined using a gas chromatograph-

mass (GC-MS, Agilent 7890A GC coupled with the 5975C Series mass spectrometry). After the

4-CP was degraded in the binary system at 10 min, TNS was separated and 10 mL of supernate

was mixed with 5 mL of dichloromethane in a separatory funnel to extract the formed

intermediates. Anhydrous Na$_2$SO$_4$ was then added to totally remove water. After filtered with

0.22 μm PTFE membrane, the organic compounds in the extraction solution were analyzed on

the GC-MS, equipped with an Agilent DB EUPAH column (121-9627, 20 m × 180 μm × 0.14 μm). GC was operated in a full scan mode, and spiltless (2.0 μL) injection was carried out at 240 °C. The oven temperature was programmed from 60 °C, and then increased to 240 °C at a rate of 10 °C/min and held for 5 min. The mass spectrometry was operated at the electron impact mode.

2.2.5. Hydroxyl radicals measurement

The amount of hydroxyl radicals (•OH) formed in the photocatalysis reaction was detected by a photoluminescence (PL) technique using terephthalic acid as the probe molecule. Terephthalic acid can react readily with •OH to form a highly fluorescent product, 2-hydroxyterephthalic acid, whose intensity is proportional to the amount of •OH. Specifically, 0.02 g of materials was dispersed into a mixture of 0.5 mmol terephthalic acid and 2 mmol NaOH occupying a total volume of 200 mL in the quartz reactor. After irradiated under UV light for 10 min, samples were taken and immediately filtered through a 0.22 μm membrane. PL spectra of the samples were measured by a Hitachi F-4500 fluorescence spectrophotometer with photomultiplier tube (PMT) R928 excited at 320 nm.

2.2.6. Material reuse

After photocatalysis of coexisting Cr(VI) and 4-CP with both concentration of 5 mg/L at pH 7, TNS were filtered though a 0.22 PTFE membrane and air-dried for reuse. Specifically, 0.2 g of TNS was immersed into 0.5 mol/L HNO_3 (500 mL) for 8 h to desorb Cr(III) from the material. After that, the material was immersed into 0.5 mol/L NaOH (500 mL) for 8 h to regenerate. Finally, TNS was reused for photocatalysis of coexisting Cr(VI) and 4-CP at pH 5, and the proposed photocatalysis-desorption-regeneration process lasted for 5 cycles.

2.3. Results and discussion

2.3.1. Morphology and crystalline of TNS

Morphology of nano-TiO$_2$ and TNS is shown in **Figure 2-1** and **Figure 2-2**, respectively.

The procurer, nano-TiO$_2$ is a kind of nano-sphere with a mean diameter of 25 nm (**Figure 2-1**).

While after hydrothermal treatment, these TiO$_2$ nanoparticles transformed into nanosheets, which

are more like ribbons (**Figure 2-2a**). High resolution TEM (HRTEM) further indicates that of the

ribbons has uniform interlayer distance of 0.70 nm, which is in accordance with the crystal plane

of titanate (020) (**Figure 2-2b**) (Chen et al. 2002). In addition, anatase crystalline (101) also can

be observed in TNS (**Figure 2-2c**) (Zhang et al. 2011), suggesting the synthesized TNS is a

composite material containing both titanate and anatase.
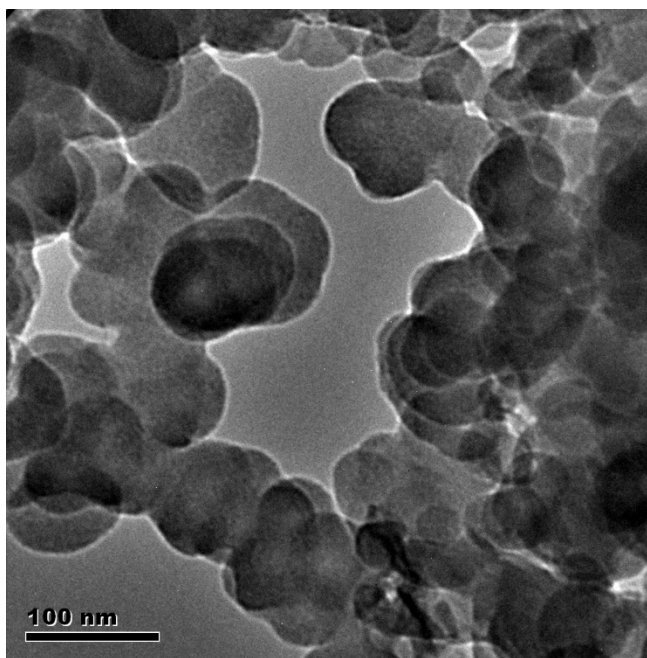
Figure 2-1. TEM image of nano-TiO$_2$.
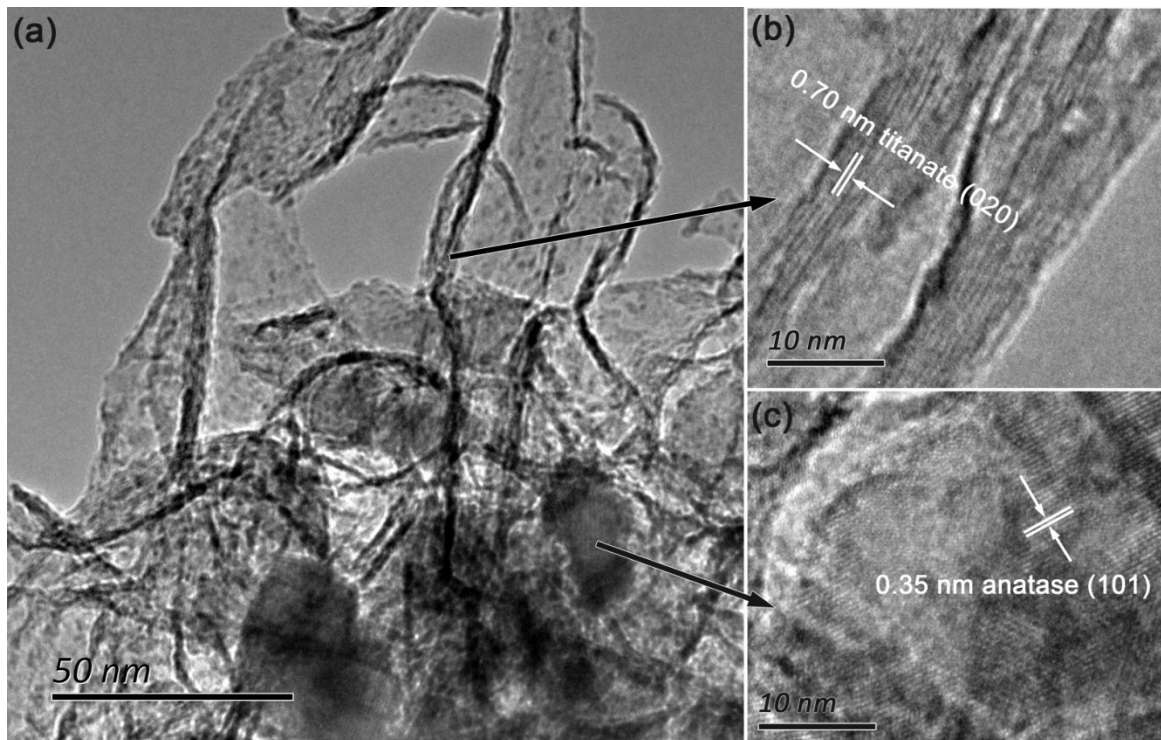
Figure 2-2. TEM images of (a) TNS and HRTEM of (b) titanate and (c) anatase in TNS.

Figure 2-3 presents the XRD patterns of nano-TiO_2 and TNS. For TiO_2, all the peaks

belong to crystalline of anatase (JCPDS 21-1272) (Gu et al. 2012, Yang et al. 2008). After

synthesis of TNS, the peaks at 25.3°, 37.9°, 53.9° and 54.9° assigned to anatase still remain,

epically the A(101) peak. However, new peaks at 9.6°, 28.4°, 48.1° and 62.7° attributed to

crystal diffraction of titanate also appeared (Liu et al. 2013c, Ma et al. 2005, Sun and Li 2003).

Specifically, the peak at 9.6° (020) represents the interlayer distance of titanate, which is 0.70 nm

for the prepare TNS in this study (**Figure 2-2b**) (Chen et al. 2002, Liu et al. 2013c, Sun and Li

2003). Moreover, the resulting titanate nanosheets are a kind of sodium tri-titanate with a

chemical formula of $Na_xH_{2-x}Ti_3O_7$ ($x = 0-0.75$, depending on the remaining sodium content),

which is composed of layered corrugated ribbons formed through edge-sharing of triple [TiO_6]

octahedrons as a skeletal structure and H^+/Na^+ located in interlayers (Liu et al. 2013c, Sun and Li 2003).
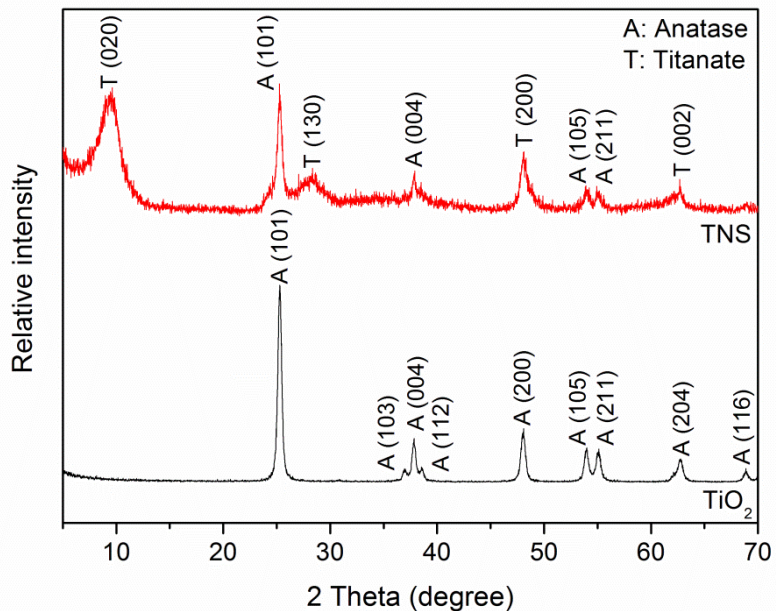
Figure 2-3. XRD patterns of nano-TiO$_2$ and TNS.

Furthermore, TNS exhibit large specific surface area of 147.9 m^2/g and total single pore volume of 0.47 cm^3/g (**Figure 2-4**). In addition, the N$_2$ adsorption-desorption isotherms of TNS is consistent with type IV isotherms with H3 hysteresis loops according to BDDT classification (**Figure 2-4b**), indicating the presence of mesopores (2–50 nm) in the material (Brunauer et al. 1940). Due to the low point of zero charge (pH$_{PZC}$ = 3.2) (**Figure 2-5**), TNS can easily capture metal cations (Cr(III) in this study), followed by ion-exchange with the interlayered H^+/Na^+ (primary Na$^+$) (Liu et al. 2014b, Liu et al. 2013c).
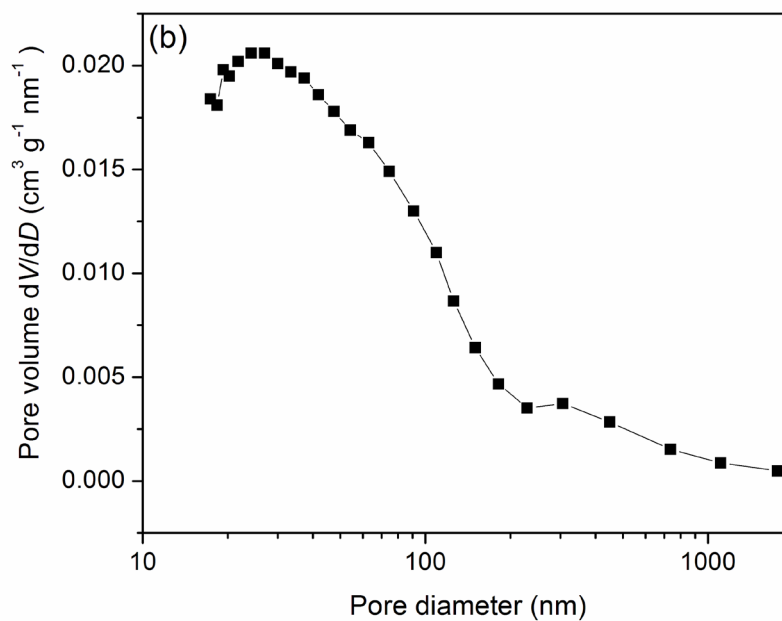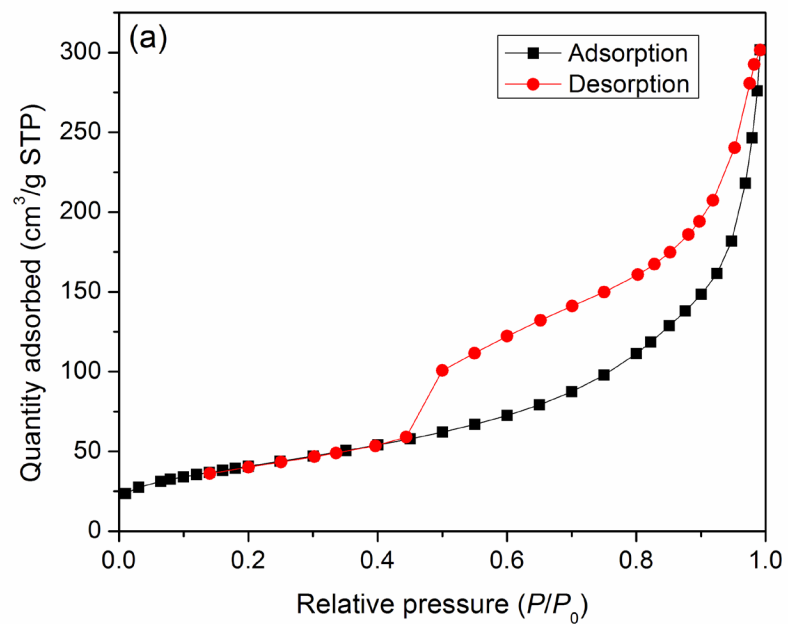
Figure 2-4. (a) N_2 adsorption-desorption isotherms and (b) pore size distributions of TNS.
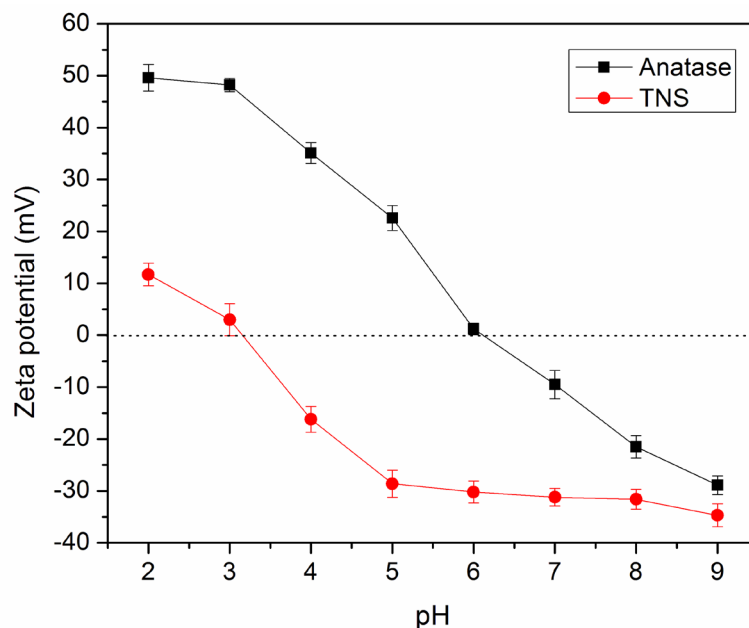
Figure 2-5. Zeta potentials of nano-TiO$_2$ and TNS at different pH.

2.3.2. Adsorption of Cr(VI), Cr(III) and 4-CP by TNS

Adsorption of Cr(VI), Cr(III) and 4-CP by TNS at different pH are displayed in **Figure 2-6**. Obviously, variations of Cr(VI) and Cr(III) adsorption capacities with increasing pH are different. The adsorption capacity of Cr(VI) decreased with increasing pH, e.g., from 1.9 to 0.8 mg/g when pH increased from 2 to 3, and then dramatically dropped to ca. 0 mg/g at pH $\geq$7. In addition, the Cr(VI) adsorption capacity was quite small in the whole pH ranges (< 2 mg/g), which was due to the low pH$_{PZC}$ of TNS (3.2). Cr(VI) exists as oxyanions (mainly HCrO$_4^-$ and CrO$_4^{2-}$) at pH 2−9, so the less positively charged (pH $\leq$ 3) or negatively charged (pH $\geq$ 4) TNS were hard to capture Cr(VI) anions, resulting in low adsorption capacity. However, Cr(III) adsorption capacity increased with increasing pH. At pH 2 and 3, the positively charges TNS could adsorb less Cr(III) cations (Cr^{3+} and Cr(OH)$^{2+}$) (**Figure 2-7b**). However, there was a

16

charge transformation for TNS from pH 3 to 4 (**Figure 2-5**), leading to great enchantment on

Cr(III) adsorption capacity from 2.1 to 7.6 mg/g. When pH future increased, more negative

charges locating on TNS resulted in larger adsorption capacity, which could reach up to 9.7 mg/g

at pH 5 as well as a high removal efficiency of 97.1%. Precipitation of Cr(III) (Cr(OH)$_3$

formation) occurred when pH $\geq$ 6, resulting in large Cr(III) adsorption capacities at higher pH

above 6. Adsorption behaviors of Cr(VI) and Cr(III) by TNS as a function of pH are similar to

the results using other titanate nanomaterials, like titrate nanotubes (Liu et al. 2013a, Liu et al.

2014a), due to the similar basic composition of sodium tri-titanate.
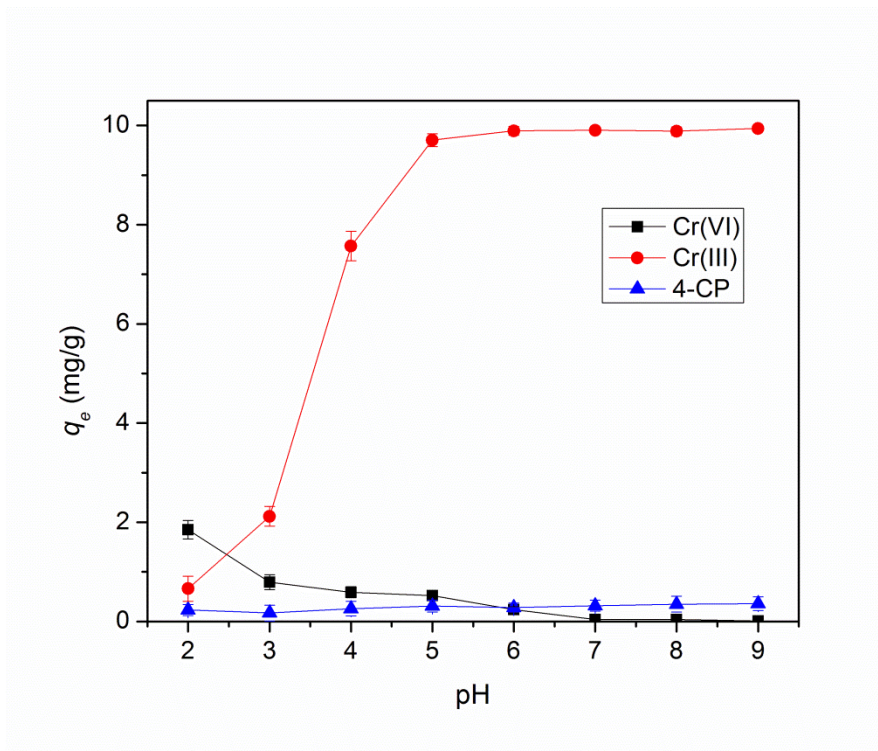
Figure 2-6. Adsorption of Cr(VI), Cr(III) and 4-CP by TNS at different pH. (Experimental condition: Initial Cr and 4-chorophenol = 5 mg/L, TNS dosage = 0.5 g/L, temperature =25±2 °C).
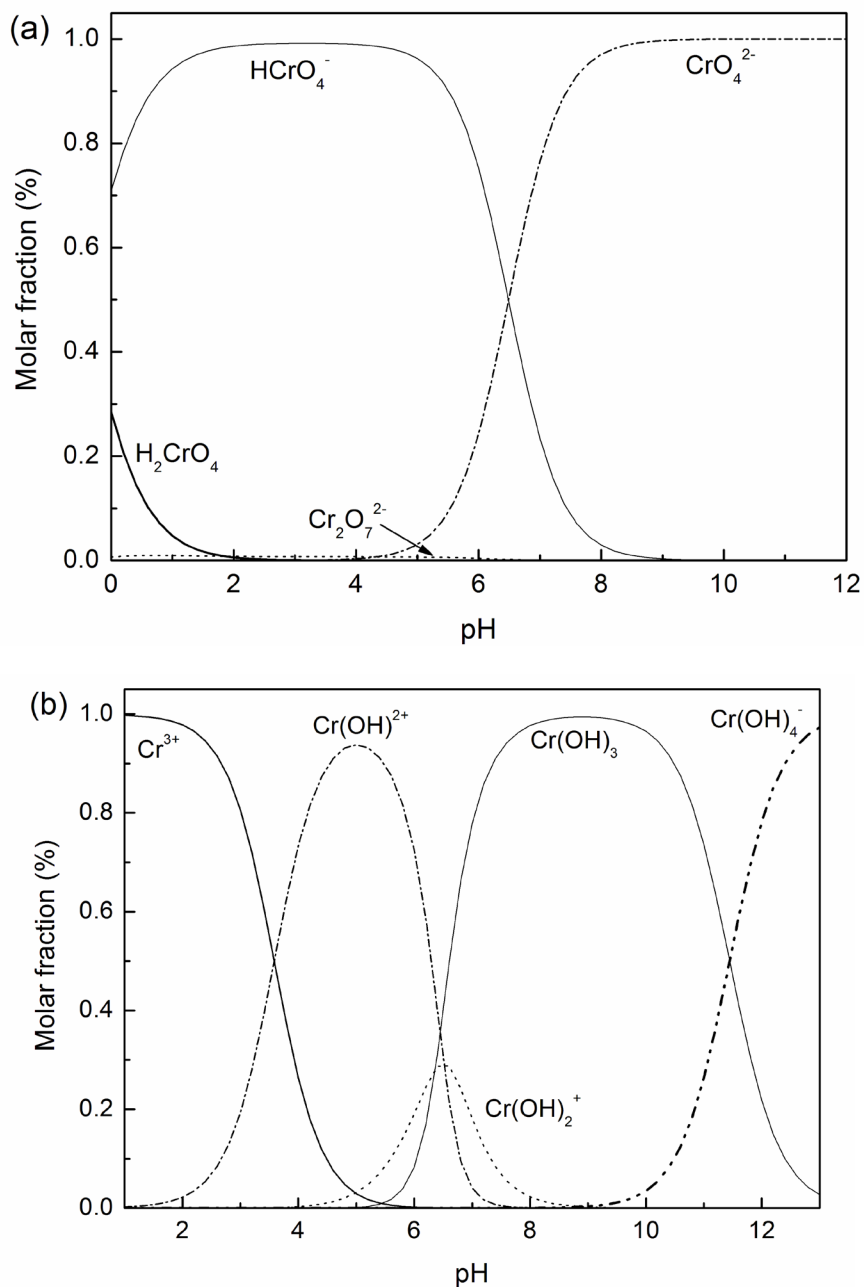
Figure 2-7. Distribution of (a) Cr(VI) and (b) Cr(III) species depending on solution pH.

It should be noticed that the adsorption capacity of 4-CP was relatively low (< 0.4 mg/g) regardless of change of pH. Considering the inorganic structure of TNS (sodium titanate) and 4-CP with a pK_a value of 9.41 (Kim and Choi 2005), the material can hardly capture the molecular

4-CP in the experimental pH ranges (2−9). Therefore, adsorption only is not available for removal of Cr(VI) and 4-CP, and photocatalysis is necessary.

2.3.3. Photocatalysis of Cr(VI) and 4-CP by TNS in single system

Solution pH of 5, 7 and 9 was selected to represent the acidic, neutral and alkaline condition respectively, and effects on photocatalytic reduction of Cr(VI) at by TNS were studied. **Figure 2-8** shows removal of total Cr and Cr(VI), as well as formation of Cr(III) over time. For Cr(III), "C_t/C_0" means the ration of formed Cr(III) in the aqueous solution to initial total Cr. Generally, total Cr and Cr(VI) in the aqueous solution gradually decreased when irradiation time moved on. There was almost no Cr(III) accumulated in solution except at initial time for pH 5, leading to overlap curves for total Cr and Cr(VI). Formation and removal of Cr(III) simultaneously proceeded in the solution, i.e., Cr(III) formed through photocatalytic reduction of Cr(VI) while was then immediately adsorbed by TNS. Cr(III) precipitation at higher pH resulted in its more rapid removal as there was no Cr(III) could be detected even at 10 min for pH 7 and 9.

Photocatalytic reduction of Cr(VI) by TNS was more quickly at lower pH, which is also shown as higher apparent rate constant (k_1) (**Table 2-1**). When pH increased from 5 to 9, the k_1 value decreased from 0.0240 to 0.0087 min^{-1}, indicating lower photocatalytic activity of TNS for Cr(VI) reduction at alkaline conditions. Moreover, there was no Cr(III) remained in solution at 210 min for all the conditions, so the final Cr (total) and Cr(VI) removal efficiency was equivalent, which was 99.6%, 97.2% and 84.8% at pH 5, 7 and 9, respectively. Results on effect of pH are consistent with the previous studies, which reported acidic condition facilitates photo-

19

reduction of Cr(VI) (Liu et al. 2014a, Vinu and Madras 2008, Wang et al. 2009), and H^+-included reactions proceed as:

$$H_2CrO_4 + 6H^+ + 3e^- = Cr^{3+} + 4H_2O \qquad (2\text{-}5)$$

or

$$HCrO_4^- + 7H^+ + 3e^- = Cr^{3+} + 4H_2O \qquad (2\text{-}6)$$

Apparently, existence of abundant H^+ is benefit to the reduction of Cr(VI) oxyanions. However, existing of OH^- will inhibit the Cr(VI) reduction because:

$$CrO_4^{2-} + 4H_2O + 3e^- = Cr(OH)_3 + 5OH^- \qquad (2\text{-}7)$$
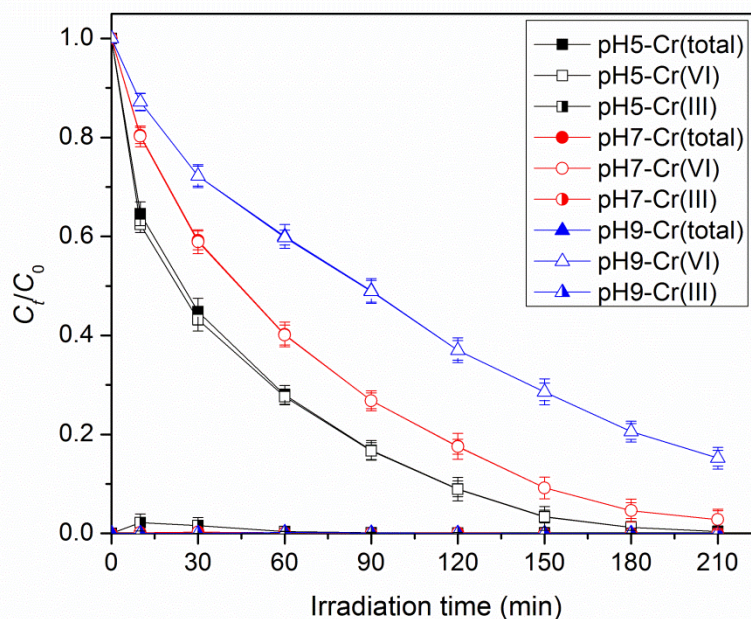
Figure 2-8. Variation of Cr(total), Cr(VI) and Cr(III) in the photocatalysis process at different pH. (Experimental condition: Initial Cr(VI) = 5 mg/L, TNS dosage = 0.5 g/L, temperature =25±2 °C).

Table 2-1. Parameters of first-order kinetics for photocatalytic reduction of Cr(VI) in binary

system

Co-existing 4-CP concentration (mg/L)	First-order model	
	k_1 (min^{-1})	R^2
0	0.0164	0.9903
2.5	0.0428	0.9678
5	0.0502	0.9756
10	0.0735	0.9874

Not like Cr(VI), higher pH facilitated 4-CP photo-degradation as displayed in Fig. 5. The k_1 value for 4-CP photocatalytic degradation increased from 0.0221 min^{-1} for pH 5 to 0.0399 min^{-1} for pH 9 (**Table 2-1**). It is worth noting that although photocatalytic activity of TNS for 4-CP photo-degradation varied at different pH, the removal rates were all over 99% at 210 min, indicating extreme high efficiency for 4-CP removal using TNS. OH$^-$ can promote the formation of hydroxyl radical (•OH), which is considered to be the primary reactive oxygen species (ROS) for organic compounds oxidation (Doong et al. 2001), and the mechanism will be further discussed in detail.
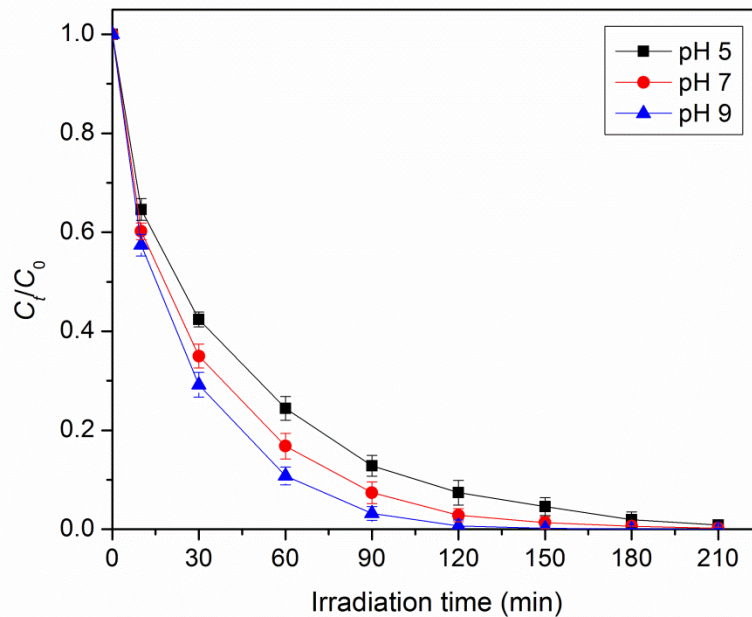
Figure 2-9. Variation of 4-CP in the photocatalysis process at different pH. (Experimental condition: Initial 4-CP = 5 mg/L, TNS dosage = 0.5 g/L, temperature =25±2 °C).

2.3.4. Photocatalysis of Cr(VI) and 4-CP by TNS in binary system

Increase of pH promoted photo-reduction of Cr(VI) while inhibited photo-degradation of 4-CP. Therefore, solution pH was set as 7 to achieve both high removal efficiencies of Cr(VI) and 4-CP in binary system. **Figure 2-10a** plots the removal of coexisting Cr(VI) and 4-CP with same initial concentration (5 mg/L) in the photocatalytic process, and removal efficiencies in single systems are also compared. It can be observed that removal of Cr(VI) was greatly promoted with coexistence of 4-CP, as the k_1 value (0.0502 min^{-1}) was ca. 3.1 times of that for Cr(VI) photo-reduction without 4-CP (0.0164 min^{-1}). Moreover, total Cr and Cr(VI) removal efficiencies were as high as 99.7 % at 120 min, which were almost similar to that at 210 min in single system. In addition, there was no Cr(III) accumulated in solution for binary system either due to high

22

adsorption capacity of TNS. Photocatalytic degradation of 4-CP was also enhanced in the binary

system, besides k_1 (0.0737 min^{-1}) exhibited ca. 2.6 times of that for 4-CP photo-degradation in

single system (0.0289 min^{-1}), 98.1 % removal of 4-CP was also achieved even at 60 min.

Therefore, synergetic promotion on photocatalytic removal of Cr(VI) and 4-CP by TNS was

found when they coexisted in solution, and this synergetic effect was closely related to the

photocatalytic mechanism involved in the reactions.
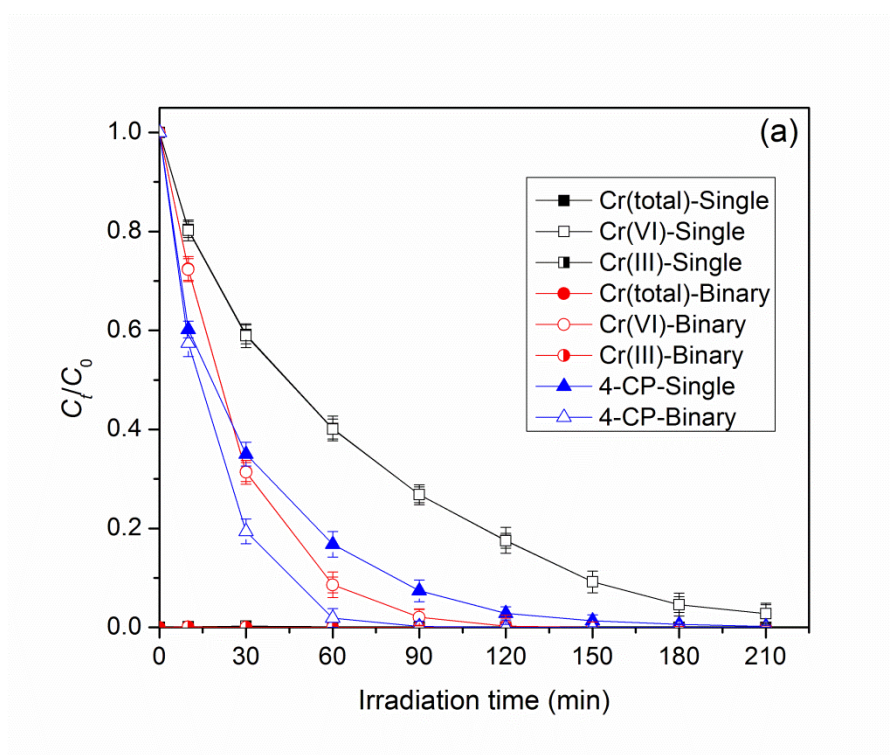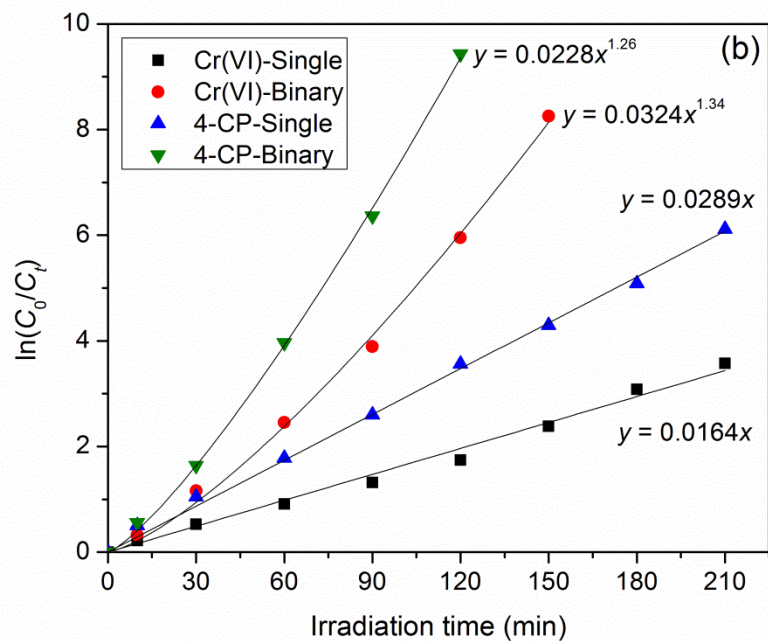
Figure 2-10. (a) Photocatalysis of Cr(VI) and 4-CP in the binary system by TNS and (b) first-order kinetic model fitting. (Experimental condition: Initial Cr(VI) and 4-CP = 5 mg/L, TNS dosage = 0.5 g/L, solution pH =7, temperature =25±2 °C).

Furthermore, it is interesting that the simulation of first-order kinetic model for photocatalysis in binary system is more like to exponential ($R^2 \geq 0.997$, $\mathrm{Ln}(C_0/C_t) = t^n$ and $n > 1$) but not linear equation (**Figure 2-10b**), indicating photocatalytic reaction accelerated with time moving on both for Cr(VI) and 4-CP. Gradual photo-reduction of Cr(VI) resulted in formation of Cr(III), which was subsequently adsorbed by TNS. TNS with Cr(III) incorporated and substituted was just like a self-doping process, thus enhancing the photocatalytic activity of TNS. In addition, the amount of Cr(III) entered into TNS increased as time moved on, leading to increase of photocatalytic activity gradually. Evidences for self-doping will be provided in detail in the next section.

To further confirm the synergetic promotion effect on photocatalysis when Cr(VI) and 4-CP coexist, photocatalytic reduction of Cr(VI) in the presence of varying 4-CP concentrations was tested and results are shown in **Figure 2-11** and corresponding first-order kinetic model parameters are listed in **Table 2-1**. Apparently, more 4-CP added in the solution resulted in higher photocatalytic rate for Cr(VI) reduction by TNS. Even at 2.5 mg/L of 4-CP, the k_1 value was as high as 0.0428 min^{-1}, which was ca. 2.6 times of that for Cr(VI) reduction without 4-CP. The k_1 value further increased to 0.0502 and 0.0735 min^{-1} when coexisting 4-CP increased to 5 and 10 mg/L, indicating the promotion effect enhanced at higher 4-CP concentration.
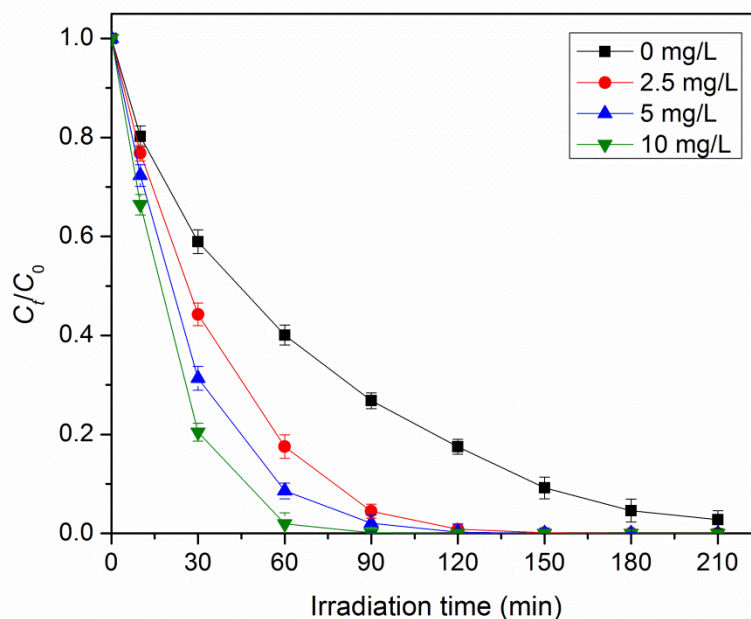
Figure 2-11. Photocatalysis of Cr(VI) with different co-existing 4-CP concentrations. (Experimental condition: Initial Cr(VI) = 5 mg/L, TNS dosage = 0.5 g/L, solution pH =7, temperature =25±2 °C).

2.3.5. Synergetic promotion mechanism for photocatalysis of Cr(VI) and 4-CP

In the photocatalysis process, TNS will generate a conduction band (electron, e^-) and a valence band (hole, h^+) under UV irradiation (Eqn. 2-8). Then Cr(VI) will be reduced to Cr(III) by the electrons (Eqn. 2-9). In the meanwhile, the holes will oxidize H_2O molecules into ROS ($\cdot OH$, $\cdot O_2^-$, H_2O_2, etc.) (Eqns. 2-10−2-15), and 4-CP can be degraded by these species via oxidation (Hou et al. 2009, Kim and Choi 2005, Liu et al. 2014a, Qiu et al. 2012) (Eqn. 16).

$$\text{TNS (titanate/TiO}_2\text{)} + hv = \text{TNS*} (e^- - h^+) \tag{2-8}$$

$$HCrO_4^- + 7H^+ + 3e^- = Cr^{3+} + 4H_2O \tag{2-9}$$

$$2H_2O + 4h^+ = O_2 + 4H^+ \tag{2-10}$$

$$H_2O + h^+ \rightarrow \cdot OH + H^+ \tag{2-11}$$

$$OH^- + h^+ \rightarrow \cdot OH \tag{2-12}$$

$$O_2 + e^- = \cdot O_2^- \tag{2-13}$$

$$\cdot O_2^- + e^- + 2H^+ = H_2O_2 \tag{2-14}$$

$$H_2O_2 + \cdot O_2^- = HO\cdot + OH^- + O_2 \tag{2-15}$$

$$\text{4-CP} + \cdot OH \text{ (or } \cdot O_2^-, H_2O_2) \rightarrow \text{ intermediates} \rightarrow \text{products} + CO_2 \tag{2-16}$$
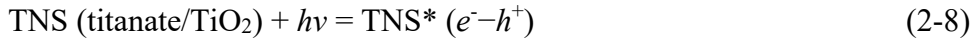
Acidic condition is benefited to the reduction of Cr(VI) according to Eqn. 2-9, while alkaline solution with abundant OH^- facilitates formation of $\cdot OH$ based on Eqns. 2-11 and 2-12. Therefore, higher removal efficiency of Cr(VI) was obtained for photocatalysis at lower pH, but lower activity for photocatalytic degradation of 4-CP was got.

Cr(III) is a widely used doping metal to modify TiO_2 so as to enhance the photocatalytic performance because of its similar atomic size with Ti (Fan et al. 2008, Zhang et al. 2008, Zhu et al. 2006). In this study, TNS with Cr(III) entered (labeled as TNS-Cr) was separated after

photocatalysis removal of Cr(VI) and 4-CP of same initial concentration (5 mg/L) at pH 7. The

UV-vis DRS spectra of TNS before and after Cr(III) entered are presented in **Figure 2-12**, and

energy band gaps (E_g) of the materials are calculated according to Kubelka-Munk theory

(Serpone et al. 1995). The light adsorption edge of neat TNS is 399 nm, with an E_g of 3.1 eV,

which is close to that of TiO$_2$ P25 and titanate nanotubes (Liu et al. 2015, Lopez and Gomez

2012). After Cr(III) doping TNS (TNS-Cr(III)), the adsorption edge shifts to visible light range

of 448 nm, and the E_g value is decreases to 2.8 eV. Narrowed energy band gap indicates much

wider ranges of lights can be utilized for photocatalytic reaction.
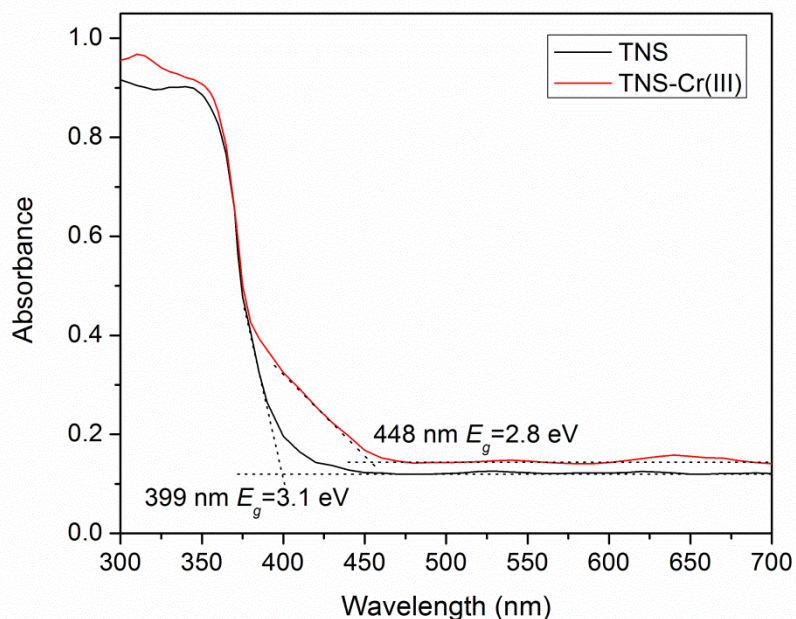
Figure 2-12. UV-vis DRS spectra of TNS before and after Cr(III) entered.

After Cr^{3+} incorporated into TNS, Cr(III) can act as trapper for the holes photo-generated by

titanate or TiO$_2$ in TNS, then the trapped holes in Cr^{4+} can further react with OH$^-$ to produce

27

hydroxyl radicals (Eqns. 2-17 and 2-18) (Zhu et al. 2006). Therefore, recombination of hole-electron pairs is inhibited due to the presence of hole media, Cr^{3+}. On the other hand, Cr(III) can also act as a donor level to produce electron under UV light, followed by production of $\bullet O_2^-$ (Eqns. 2-19 and 2-20) (Liu et al. 2014a, Zhu et al. 2006), which is a strong ROS that can further degrade 4-CP.

$$Cr^{3+} + h^+ \rightarrow Cr^{4+} \tag{2-17}$$

$$Cr^{4+} + OH^- \rightarrow Cr^{3+} + \bullet OH \tag{2-18}$$

$$Cr^{3+} + hv \rightarrow Cr^{4+} + e^- \tag{2-19}$$

$$e^- + O_2 \rightarrow \bullet O_2^- \tag{2-20}$$

To examine if more ROS (mainly $\bullet$OH) are produced for TNS-Cr, **Figure 2-13** displays the $\bullet$OH production by TNS with different Cr(III) doping dosages. Typically, a pre-adsorption process was conducted to get TNTs-Cr(III) with different Cr(III) doping dosages, as 0.2, 0.5 and 1.0 wt.%, for which 1, 2.5 and 5 mg/L of Cr(III) were absorbed by 0.5 g/L TNS at pH 7, respectively. It is observed that produced $\bullet$OH amount (proportional to fluorescence intensity) enhanced after Cr(III) incorporated into the TNS, and higher Cr doping dosage resulted in larger radical amount. Therefore, Cr self-doping exactly facilitates the photocatalytic degradation of 4-CP due to more produced ROS.
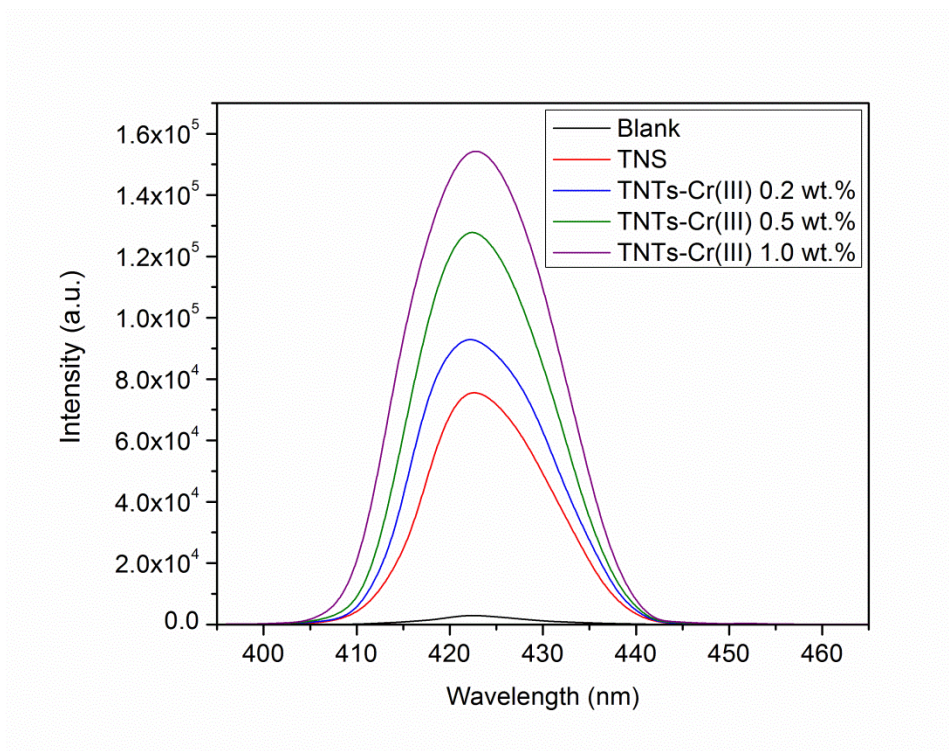
Figure 2-13. photoluminescence spectra for TNS before and after Cr(III) entered.

Photocatalytic degradation intermediates of 4-CP in the binary system were then determined using GC-MS, and a degradation pathway is proposed according to the detected products. The observed degradation pathway of 4-CP by TNS is similar to that for the photocatalysis by TiO_2 or other oxidation processes reported previously (Ai et al. 2005, Cheng et al. 2007, Johnson et al. 1999, Zhao et al. 2010), with regarding to the determined intermediates of hydroquinone (peak B, $m/z = 110$), benzoquinone (peak C, $m/z = 108$), and 4-chlorocatechol (peak D, $m/z = 144$) in the GC spectra (**Figure 2-15**) and MS confirmation (**Table 2-2**). Specially, after attack by •OH, two pathways are included for the 4-CP oxidative degradation: 1) dechlorination to form hydroquinone and then benzoquinone (A→B→C in Fig. 10), and 2) dehydrogenation to form 4-chlorocatechol and then hydroxyhydroquinone (A→D→E in **Figure 2-14**). Although we did not

29

detect hydroxyhydroquinone (compound E in **Figure 2-14**) due to its high activity and non-stability, it is widely confirmed to be an important intermediate in 4-CP degradation process (Cheng et al. 2007, Zhao et al. 2010). Carboxylic, small aliphatic compounds and even CO_2 form for future oxidation (Ai et al. 2005, Cheng et al. 2007, Johnson et al. 1999, Zhao et al. 2010). Therefore, •OH is the most important ROS for 4-CP photocatalytic degradation, and more produced amount of •OH will undoubtedly enhance the reaction as confirmed in **Figure 2-13**
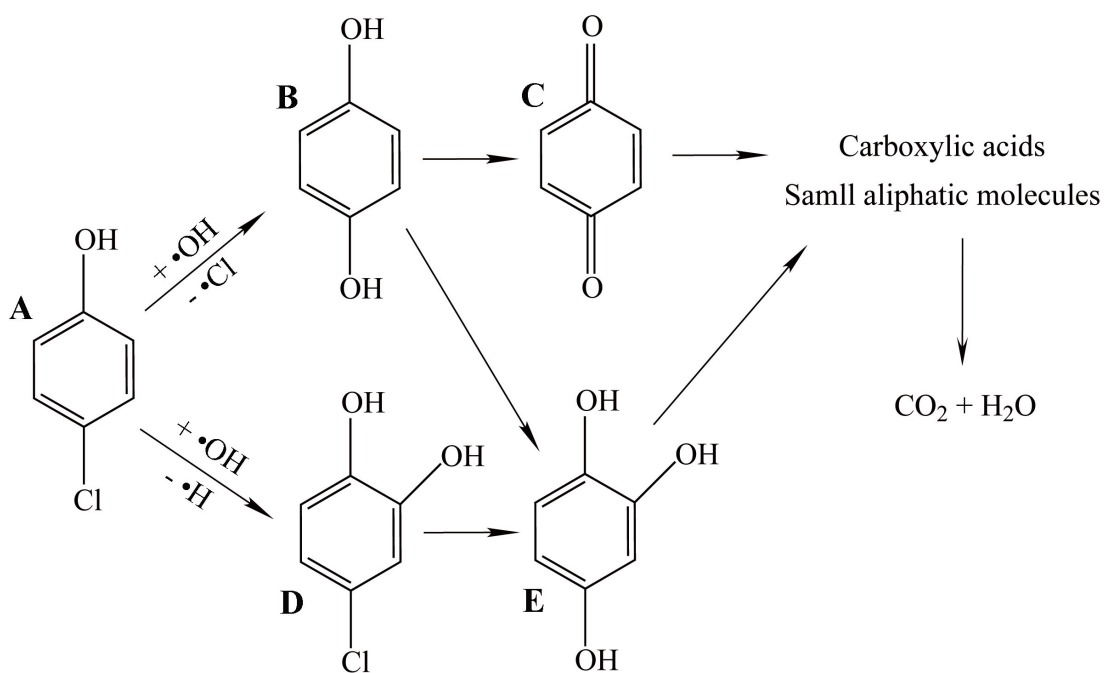
Figure 2-14. Proposed degradation pathway of 4-CP by TNS through photocatalysis.
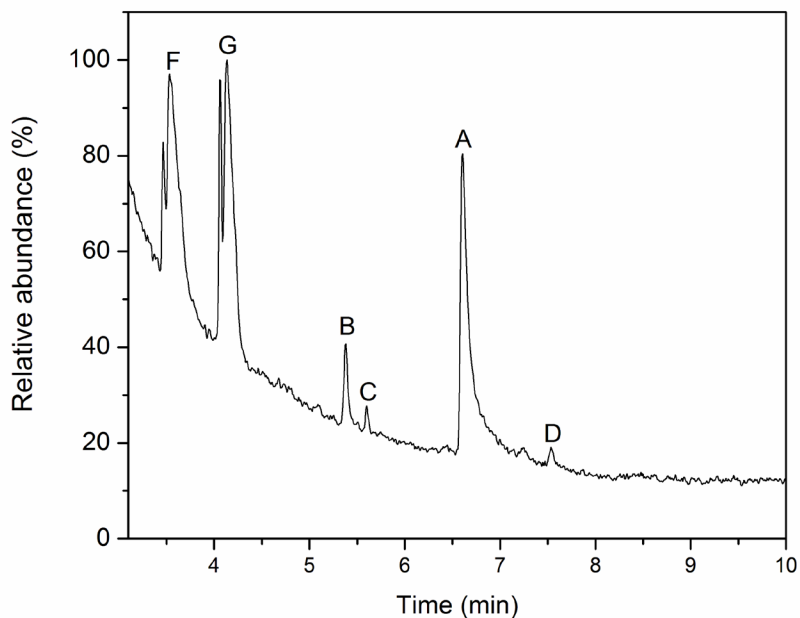
Figure 2-15. Total ion chromatograms of 4-CP and formed products after 10 min photocatalysis by TNS in the binary system.

Table 2-2. Mass spectral characteristic ions of main intermediates for in the 4-CP photocatalytic degradation process.

Peak	Retention time (min)	Compound	Molecular weight	Characteristic ion (*m/z*)
A	6.6	4-Chlorophenol	129	128, 130, 84
B	5.4	Hydroquinone	110	110, 81, 97
C	5.6	Benzoquinone	108	108, 55, 155
D	7.5	4-Chlorocatechol	144	144, 146, 171
F&G	3.5&4.1	Dichloromethane (Solvent)	85	51, 84, 87

Figure 2-16 depicts the synergetic promotion effect and self-doping process for simultaneous

removal of Cr(VI) and 4-CP. TNS is a composite material with combined crystal phases of

anatase and titanate. Under light irradiation, TNS (mainly the anatase phase) will generate a

31

conduction band (e^-) and a valance band (h^+). Cr(VI) will reduce to Cr(III) after acceptance of e^- (Reaction 1), while oxidative degradation of 4-CP by ROS also occurs (Reaction 2) with the help of h^+. Continuous consumption of electron and hole for photocatalytic reduction and oxidation in the same system leads to efficient separation of the h^+−e^- pairs and thus a synergetic promotion effect occurs with coexistence of Cr(VI) and 4-CP. Moreover, the photo-reduced Cr(III) can be immediately adsorbed and incorporated into titanate (Reaction 3), which is a self-doing process and can enhance the photocatalytic activity of TNS via narrowed band energy gap (from 3.1 to 2.8 eV). Therefore, it is interesting that photo-reduction of Cr(VI) and photo-degradation of 4-CP are greatly promoted in binary systems, due to the dual mechanisms of synergic effect and self-doping.
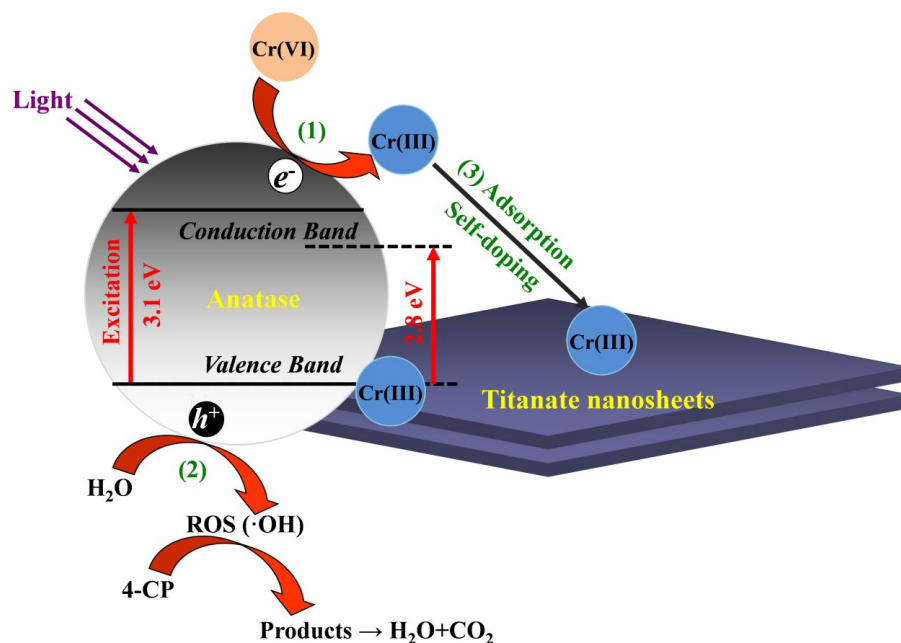
Figure 2-16. Schematic diagram for synergetic promotion effect and self-doping in the photocatalysis process.

2.3.6. Reuse of TNS

After photocatalysis, we proposed a two-step procedure to regenerate TNS based on our previous studies (Liu et al. 2014a, Wang et al. 2013c). Adsorbed Cr(III) will be desorbed from TNS through a 0.5 M HNO_3 treatment, while adsorption sites ($-ONa$ groups) will restore via further 0.5 M NaOH treatment. The regenerated material was reused for photocatalytic removal of coexisting Cr(VI) and 4-CP under foregoing conditions and lasted for 5 cycles. **Figure 2-17** depicts the removal of Cr and 4-CP over the 5 cycles. TNS showed good reusability, as the removal efficiency of total Cr and Cr(VI) could still reach up to 97.8% through 210 min photocatalysis even at the 5th cycle, and there was still no Cr(III) was detected in solution. Similarly, removal efficiency of 4-CP was high as 99.3% at the 5th cycle. In addition, the titanate nanomaterials can be easily separated from solutions due to the heterogeneous structure/composition compared to nano-TiO_2 (Liu et al. 2013b). Simple regeneration procedure and good reusability of TNS make it a promising material in environmental remediation area, especially for complex contaminants with co-existence of heavy metals and organic pollutants.
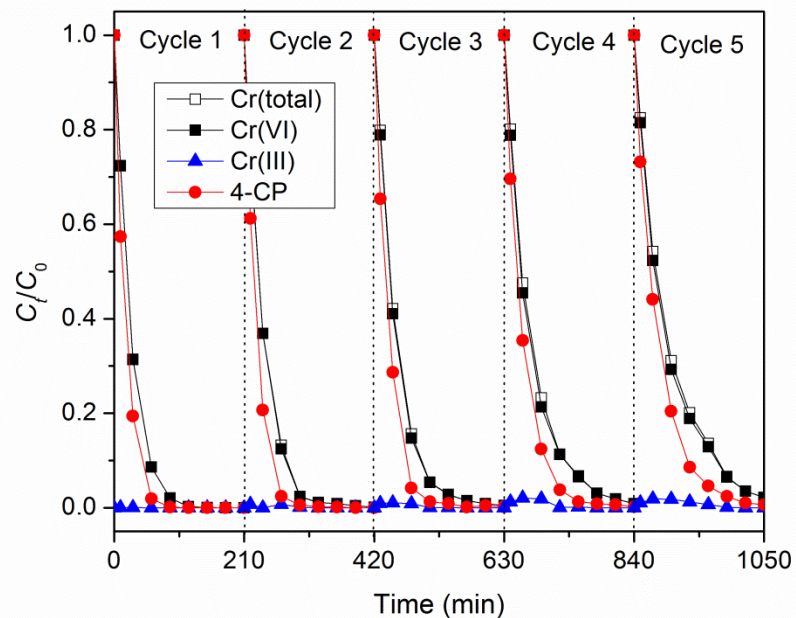
Figure 2-17. Reuse of TNS for photocatalytic removal of Cr(VI) and 4-CP in binary system over 5 cycles. (Experimental condition: Initial Cr(VI) and 4-CP = 5 mg/L, TNS dosage = 0.5 g/L, solution pH =7, temperature =25±2 °C).

2.4. Conclusions

Titanate nanosheets were synthesized through a facile one-step hydrothermal treatment using nano-anatase and NaOH. TEM and XRD analysis indicate that the prepared TNS are a composite material of anatase attaching onto titanate. TNS showed good adsorption capacity for cationic Cr(III) but could hardly capture anionic Cr(VI) and molecular 4-CP from solutions, and therefore, photocatalysis was necessary. Cr(VI) could be efficiently photocatalytic reduced by TNS, with a high removal efficiency of 97.2% at pH 7, and the formed Cr(III) was immediately adsorbed onto TNS at the same time. Moreover, over 99% of 4-CP could be photo-degraded by TNS at pH 5−9. In the binary system with co-existence of Cr(III) and 4-CP, either Cr(VI) or 4-

34

CP removal efficiency was enhanced compared to that in single systems under the same condition, as the apparent rate constant (k_1) for photocatalysis removal of Cr(VI) and 4-CP increased to ca. 3.1 and 2.6 times, respectively.

The mechanisms for enhanced removal efficiency with co-existence of Cr(III) and 4-CP are attributed to two aspects: On one hand, photo-reduction of Cr(VI) by electrons and photo-degradation of 4-CP by holes result in the efficient separation of electron-hole pairs, suggesting a synergetic effect occurs; On the other hand, adsorption of Cr(III) by TNS leads to narrowed energy band gap as well as enhanced photocatalytic activity of the materials, which is a self-doping process. Production of •OH and UV-DRS spectra further confirmed the synergy and self-doping mechanisms.

TNS could be efficiently reused for photocatalytic removal of Cr(VI) and 4-CP, as 97.8% and 99.3% removal efficiencies of the two pollutants were achieved even after 5 cycles respectively, making TNS a promising material for simultaneously removing both heavy-metal and organic pollutants from wastewaters.

Chapter 3: Hydrothermal synthesis of graphene grafted titania/titanate nanosheets for photocatalytic degradation of 4-chlorophenol: Solar-light-driven photocatalytic activity and computational chemistry analysis

G/TNS was prepared by grafting graphene (G) onto TNS, where G/TNS appeared as flower-like nanoscale sheets containing Ti crystalline phases of both anatase and sodium titanate. Graphene acted as a two-dimensional template for growth of Ti-nanosheets, which inhibited transformation of TiO_2 into titanate during the hydrothermal reaction. G/TNS with 2.0 wt.% graphene showed the highest photocatalytic degradation rate for 4-chlorophenol, and >99.2% of removal was achieved at 120 min. The pseudo-first order rate constant (k_1) was determined to be 0.041 min^{-1}, which is ~8 times higher than that of anatase and ~21 times than unmodified TNS. The findings indicate that the grafted graphene greatly promotes the material response to visible light because: (1) it facilitates rapid transfer of photo-excited electrons, thus inhibiting recombination of the h^+-e^- pairs, and (2) narrowed band gap energy leading to enhanced visible light absorption. Evidently, the 2-D sheet-like structures are conducive to electron transfer and solar-light-driven photocatalytic activity. The $^\bullet$OH radicals were found to be the primary reactive oxygen species for 4-CP degradation. Density functional theory (DFT) analysis indicates that the sites on 4-CP with a higher Fukui index (f^-) are preferentially attacked by $^\bullet$OH, and the theoretical calculation results were consistent with the experimentally identified 4-CP degradation pathway. In addition, G/TNS showed good reusability, and >90% of 4-CP still could be removed after 5 consecutive cycles.

3.1. Introduction

Titanium-based materials, including TiO_2 and titanate, are widely used for photocatalytic degradation of organic compounds (Kumar and Devi 2011, Hashimoto et al. 2005, Schneider et al. 2014). As a standard photocatalyst, TiO_2 presents excellent photo-electrical response to the UV spectrum, low cost, low toxicity and high stability (Kumar and Devi 2011, Hashimoto et al. 2005, Schneider et al. 2014). Titanate materials, which are derived from TiO_2, offer even larger specific surface area and better ion-exchange property compared to TiO_2, though the photocatalytic activity is slightly compromised due to quick recombination of electron-hole pairs after excitation (Bavykin et al. 2006a, Ou and Lo 2007, Zhao et al. 2016). Therefore, development of composite materials by combining TiO_2 and titanate phases can integrate the advantages of these two homologous Ti-materials. Furthermore, it is also highly desired to enhance the photocatalytic activity under solar light by tailoring Ti-materials.

Previously, we prepared a nanocomposite of anatase/titanate nanosheet (TNS), which was able to simultaneously remove Cr(VI) and 4-chlorophenol through photocatalysis (Liu et al. 2016a). However, TNS only exhibited UV light response, i.e., little photocatalytic activity under visible light, thus limiting its practical application upon solar energy. Therefore, modification of TiO_2 or titanate so as to improve the solar-light-driven photocatalytic performance is of great significance. In recent years, graphene, a two dimensional (2-D) material, has drawn increasing research interests due to its excellent mobility of charge carriers, large specific surface area, flexible structure, high transparency, and good electrical and thermal conductivity (Morales-Torres et al. 2012, Lee et al. 2012, Pan et al. 2012, Perera et al. 2012). Graphene has been often used for decoration/modification of TiO_2 based photocatalysts to improve their photocatalytic activity (Morales-Torres et al. 2012, Pan et al. 2012, Perera et al. 2012, Zhao et al. 2012, Liang et al. 2010). Compared to TiO_2 nanoparticles, application of TNS as skeleton to support graphene

37

may have the following advantages: Firstly, the alkali-hydrothermal reaction, which is used to transform TiO_2 into titanate (Bavykin et al. 2006a, Kasuga et al. 1999, Chen et al. 2002), can facilitate incorporation of graphene into titanate to form stale material architecture (Perera et al. 2012). Secondly, photo-excited electrons from 2-D TNS can easily transfer by 2-D graphene, leading to a synergetic effect (Kim et al. 2014a, Zhang et al. 2014). Finally, the large surface area of TNS is beneficial to the interaction with target contaminants (Liu et al. 2016a). However, information remains lacking on the morphology, crystalline phases, compositions and photocatalytic property of graphene-modified Ti-materials, in particular, when used for degradation of persistent organic pollutants (POPs) under solar light.

Chlorinated phenols (CPs) are one of the most common POPs in industrial wastewater. Main industrial sources include tanning, manufacturing of preservatives, pesticides and antifouling agents (Sorokin et al. 1995, Sze and McKay 2012). Due to their stable molecular structure and the C−Cl bonds, CPs are rather persistent to natural degradation , and show high toxicity and carcinogenicity to the ecosystem and human health (Ahlborg et al. 1980, Hirvonen et al. 2000). To mitigate the toxic effects of CPs, numerous technologies have been investigated to remove CPs from contaminated water (Dąbrowski et al. 2005, Chowdhury and Viraraghavan 2009, Gimeno et al. 2005, Dionysiou et al. 2000). In addition to adsorption and advanced oxidation processes (AOPs), photocatalysis has been found effective for removal and mineralization of CPs (Dąbrowski et al. 2005, Chowdhury and Viraraghavan 2009, Gimeno et al. 2005, Dionysiou et al. 2000). To this end, TiO_2 or modified TiO_2 has been the most used photocatalysts for photocatalytic degradation of various CPs, e.g., 2-chlorophenol (2-CP), 4-chlorophenol (4-CP), 2,4-dichlorophenol (2,4-DCP), 2,4,6-trichlorophenol (2,4,6-TCP), *etc*. (Dionysiou et al. 2000, Ai et al. 2005a, Khuzwayo and Chirwa 2015). Although the

photocatalytic removal efficiencies of CPs and related degradation pathway have been well documented, these processes are much less effective under solar irradiation, and there is a need to understand photocatalytic mechanisms pertaining to roles of radicals and reactive sites of CPs' molecules in order to further improve the photocatalytic performances. In addition, the booming development of computational chemistry (Jensen 2017, De Proft and Geerlings 2001, Di Valentin et al. 2005) may offer deeper insight into the underlying mechanisms at the molecular level.

In this study, we prepared a new type of 2-D graphene modified Ti-nanosheets (G/TNS) for the first time through a facile one-step hydrothermal treatment technique. The new composite material displayed very high solar-light-driven photocatalytic activity when 4-CP was tested as a model POP. The specific objectives of this work were to: (1) prepare and characterize a new class of graphene modified Ti-nanosheets; (2) test the photocatalytic activity of G/TNS under solar light using 4-CP as the model compound; (3) interpret the mechanism on enhanced photocatalytic performance and role of the graphene grafting, (4) examine the 4-CP photocatalytic degradation pathway and radical attacking mechanism by means of computational chemistry analysis, and (5) evaluate the reusability and stability of G/TNS.
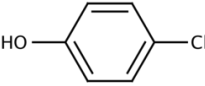
3.2. Methods and materials

3.2.1. Chemicals and materials

All chemicals used in this study were of analytical grade or better. Nanoscale TiO_2 (anatase of 99.7%, mean size of 25 nm) was purchased from Sigma-Aldrich (St. Louis, MO, USA). Graphene was obtained from Nanjing Xianfeng NANO Material Tech Co. Ltd. (Nanjing, China), and used without further treatment. NaOH, HCl and KI and were purchased from Acros Organics (Fair Lawn, NJ, USA). Absolute ethanol and isopropanol were purchased from BDH Chemicals

of USA. 4-CP (physicochemical properties shown in Table 3-1) was acquired from Sigma-Aldrich (St. Louis, MO, USA), and a stock solution of 100 mg/L was prepared and stored at 4 °C. All solutions were prepared using de-ionized (DI) water (18.2 MΩ cm, Millipore Co., USA).

Table 3-1. Physicochemical properties of 4-CP.

Parameters	Values[a]
Chemical formula	C_6H_5ClO
Molecule weight	128.56 g/mol
Chemical structure	
pK_a	9.41
Log K_{ow}	2.39
Solubility in water	2.4×10^4 mg/L (25 °C)
CAS Number	106-48-9

3.2.2. Synthesis and characterizations of G/TNS

G/TNS nano-composite was synthesized through a modified one-step hydrothermal method based on our previous studies (Liu et al. 2016a, Li et al. 2015). Typically, 0.8 g TiO_2 was mixed with a known mass (0.5−2.5 wt.% of TiO_2) of graphene and then dispersed into 8 mol/L of NaOH solution (80 mL). After stirring for 12 h, the mixture was transferred into a Teflon reactor and then heated at 130 °C for 3 h. After that, DI water was used to wash the gray precipitate till

the pH of supernatant reached ~8. The final product was dried in an oven at 105 °C for 4 h. For comparison, TNS was also synthesized via the same procedure but without graphene.

The morphology of G/TNS was obtained on a JSM-7000F scanning electron microscopy (SEM, JEOL, USA) operated at 20 kV. The crystal phases of the material was analyzed using a D/max-2400 X-ray diffractometer (XRD, Rigaku, Japan) at 100 kV and 40 mA, with the Cu $K\alpha$ radiation ($\lambda = 1.542$ Å) and a scanning rate of 4°/min. The Brunauer-Emmett-Teller (BET) surface area of TNTs@PAC was obtained on an ASAP 2010 surface area analyzer (Micromeritics, USA) in the relative pressure (P/P_0) range of 0.06–0.20. Diffuse reflectance UV-vis absorption spectra (UV-DRS) of the materials were measured on a UV-2400 spectrophotometer (Shimadzu, Japan). $BaSO_4$ powder was used as the reference at all energy levels (100% reflectance) and the reflectance measurements were converted to absorption spectra through Kubelka-Munk function. Pore size distribution was obtained following the Barrett-Joyner-Halenda method, and nitrogen adsorption volumes at the relative pressure of 0.99 were used to determine the pore volumes and the average pore diameters. Zeta potential of the material at various pH levels was measured on a Nano-ZS90 Zetasizer (Malvern Instruments, UK).

3.2.3. Photocatalytic degradation experiments

Batch photocatalytic degradation kinetic tests were conducted using a cylindrical glass reactor (volume = 200 mL) with a quartz cover, and Fig. 1 displays the schematic of the experimental setup. A 500 W Xenon lamp (CHFXQ 500 W, Global Xenon Lamp Power) was employed to simulate the solar light, which was placed vertically over the reactor (10 cm away). Cooling water was circulated around the reactor to maintain the system temperature at 25 ± 0.2 °C. To test the photocatalytic activity, 5 mg/L of 4-CP and 0.2 g/L of G/TNS prepared with

various amounts of graphene was mixed in the reactor and the solution pH was adjusted to 7.0 using diluted HCl or NaOH. The photocatalytic reaction was then followed for 120 min. At specific time intervals, water samples (1 mL each) were taken and immediately filtered through a 0.22 μm polytetrafluoroethylene (PTFE) membrane, and 4-CP concentration in the filtrate was then analyzed. Control tests were carried out in the dark to gauge adsorption of 4-CP on G/TNS. To examine the contributions of visible light to 4-CP photodegradation, a UV cut-off filter (Beijing Electric Light Institute, China) was used to remove all the UV lights with wavelength <420 nm.
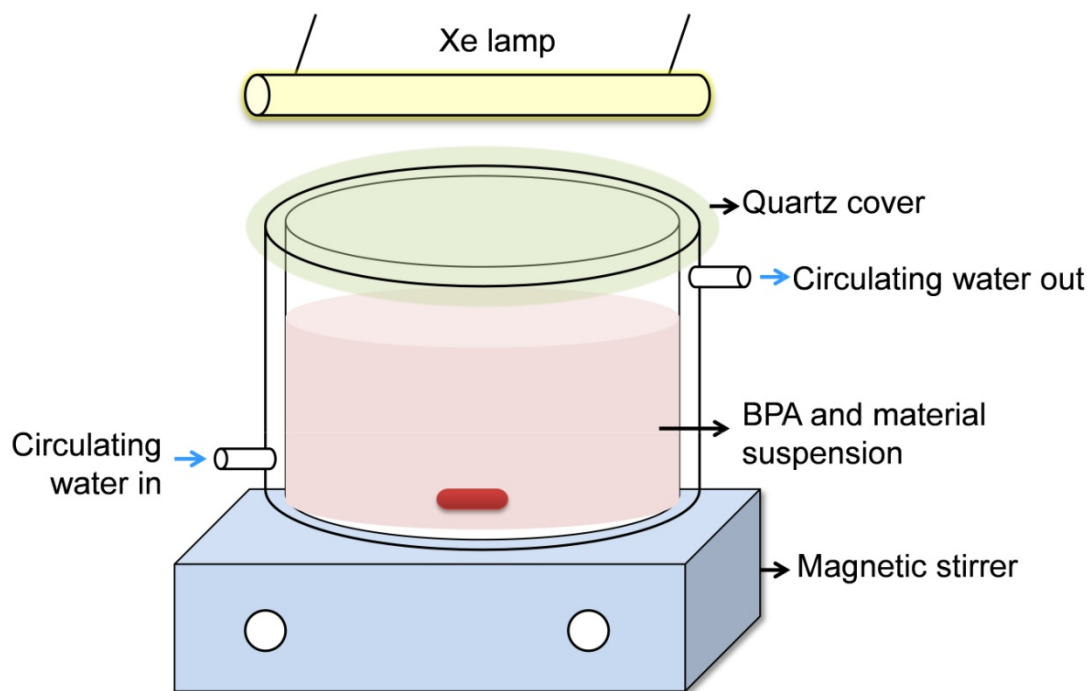
Figure 3-1. Schematic of experimental set-up.

The pseudo first-order kinetic model based on the Langmuir-Hinshelwood (L-H) model is employed to describe the 4-CP photo-degradation kinetics (Satterfield 1970, Liu et al. 2014):

$$\ln(C_0 / C_t) = k_1 t \tag{3-1}$$

where C_0 and C_t (mg/L) are the 4-CP concentrations in solution at time 0 and t (min), respectively, and k_1 (min^{-1}) is the first-order rate constant.

To reveal the roles of reactive oxygen species (ROS) in 4-CP photocatalysis, various quenching agents, including KI, isopropanol and benzoquinone (BQ) (1 mL each) were added in the solution. Formation of hydroxyl radicals (•OH) by the photocatalysts was further analyzed by the photoluminescence (PL) technique with terephthalic acid as the probe molecule. Terephthalic acid can readily react with •OH to form a highly fluorescent product, 2-hydroxyterephthalic acid (HTA) (Liu et al. 2015, Guo et al. 2013), which was recorded on a fluorescence spectrophotometer (Model Cary Eclipse, Varian, USA) at an excitation wavelength of 425 nm and emission wavelength varying from 390 to 460 nm.

3.2.4. Analytical methods

4-CP concentration was measured on an Agilent 1100 high performance liquid chromatography (HPLC, USA) equipped with a Zorbax SB-C18 column (2.1 mm × 150 mm, 5 μm) and a diode array detector (DAD). A mixture of methanol (HPLC grade) and ultrapure water (v/v of 60:40) was applied as the isocratic eluent at a flow rate of 0.2 mL/min and the eluate analyzed at an UV array detector of 280 nm.

Reaction intermediates and products during the photocatalysis were analyzed using an Agilent HPLC-MS system (HP 1100 LC-M^{Sn} Trap SL System, Agilent, USA) equipped with a Zorbax SB-C18 column, and the injection sample volume was 20 μL. Acetonitrile and water were used in the mobile phase and **Table 3-2** gives the operating gradients and program. The electrospray ionization at the negative mode (ESI-) was applied with a mass scan range of m/z 50−500 and a mass fragmentation voltage of 70 eV and a capillary voltage of +4500 V. Ionization in the ESI source was achieved using nitrogen as a nebuliser and drying gas at 45 psi.

Table 3-2. Mobile phase gradients for LC operation.

Acetonitrile	H₂O	Time (min)
5%	95%	0
5%	95%	4
40%	60%	12
95%	5%	20
95%	5%	26
5%	95%	36

3.2.5. Computational analysis

Fukui function based on the density functional theory (DFT) was used to predict the regioselectivity of radicals (•OH in this study) towards the 4-CP molecules. All of the calculations were performed using the Gaussian 03 software (Frisch et al. 2003). The geometry optimization and single-point energy calculations were executed using the B3LYP method with the 6-311+G(d,p) basis set. Fukui function is an important concept in the conceptual density functional theory (CDFT), and it has been widely used in prediction of reactive sites of electrophilic and nucleophilic attacks (Parr and Yang 1984). Specifically, Fukui function is defined as:

$$f(r) = \left[\frac{\partial \rho(r)}{\partial N} \right]_V \tag{3-2}$$

where $\rho(r)$ is the electron density at a point r in space, N is the electron number in the present system, and the constant term v in the partial derivative is the external potential. In the

condensed version of Fukui function, the atomic population number is used to represent the electron density distribution around an atom. The condensed Fukui function can be calculated as:

Electrophilic attack: $f_A^- = q_{N-1}^A - q_N^A$ (3-3)

where q^A is the atom charge of atom A at the corresponding state. The reactive sites on a molecule usually have larger values of Fukui index than other regions. Hydroxyl radical has been classified as a kind of electrophile, which is more likely to attack the sites that can readily lose electrons (De Vleeschouwer et al. 2007). Thus, we calculated the Fukui index (f^-) of 4-CP for electrophilic attacks. In this study, the natural population analysis (NPA) charge is used to study the reactive sites, as it is considered to be one of the most suitable methods to calculate Fukui index (Olah et al. 2002). A color gradient for the set of Fukui values is generated using the conditional formatting tool in Microsoft Excel 2013, with the maximum value assigned a shade of red (RGB code 255:00:00) and the smallest value assigned a shade of white (RGB 255:255:255) for Fukui index.

3.2.6. Material reusability

Following the first run of the photocatalysis of 4-CP ($C_0 = 5$ mg/L, G/TNS with 2.0 wt% graphene = 0.2 g/L, pH = 7.0), the photocatalyst was separated through filtration using a 0.22 μm PTFE membrane, and then re-used in another photodegradation run under otherwise identical conditions, and the same tests were repeated for 5 cycles. Dissolution of Ti into solution in each cycle and at different pH was also detected by measuring the total Ti level in the solution using an inductive coupled plasma - optical emission spectrometry (ICP-OES, Prodigy, Leeman, USA).

3.3. Results and discussion

3.3.1. Morphologies, crystal phases and compositions of G/TNS

Figure 3-2 displays SEM images of TiO_2, graphene and G/TNTs (with 2.0 wt.% graphene). The precursor, TiO_2, presents as nanospheres with diameters of 20−30 nm (Fig. 2a) (Liu et al. 2016a, Li et al. 2015), which is consistent with the manufacturer reported value (mean size of 25 nm). Graphene exhibits as fine sheets composed of one-atom-thick layered carbon atoms (Fig. 2b). After the hydrothermal reaction, the resulting G/TNS appears as flower-like nanoscale sheets (Fig. 2c). In addition, considering the small fraction (2.0 wt.%) of graphene in G/TNS, the formed nanosheets are mainly titanium materials. Yet, graphene acted as a template for the growth of Ti-nanosheets in the hydrothermal process, while high NaOH concentration (8 M) and reaction temperature (130 °C) lead to fragmentation of the graphene sheets.
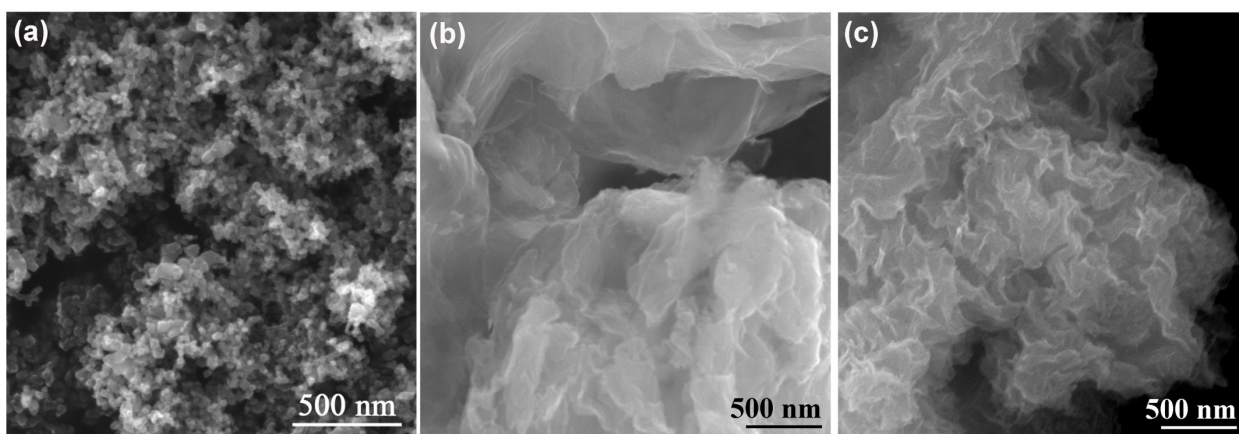
Figure 3-2. SEM images of (a) TiO2 (P25), (b) graphene and (c) G/TNS (2.0 wt.% graphene).

Figure 3-3 shows the XRD patterns of TiO_2, TNS and G/TNS with 2.0 wt.% graphene. TiO_2 presents only crystalline phases of anatase (JCPDS 21-1272) (Yang et al. 2008). For TNS without graphene grafted, the XRD spectra revealed clear crystalline phase transformation, although some of anatase phases, e.g., A(101), remained. The new peaks at 9.6°, 28.4°, 48.1° and 62.7° are attributed to sodium tri-titanate (Liu et al. 2016a, Sun and Li 2003, Liu et al. 2013).

The characteristic peak at 9.6° (T(020)) represents the interlayer distance of titanate (Liu et al. 2016a, Sun and Li 2003, Liu et al. 2013). The sodium tri-titanate, with a chemical formula of $Na_xH_{2-x}Ti_3O_7$ (x depends on the remaining sodium), is composed of layered corrugated ribbons formed by edge-sharing triple $[TiO_6]$ octahedrons as skeletons and the exchangeable H^+/Na^+ counter ions located in the interlayers (Sun and Li 2003, Liu et al. 2013). For G/TNS, the crystal structure is closer to the precursor anatase than TNS, and only a weak T(020) peak was observed at ~8.4°, suggesting that the addition of graphene inhibited the phase transformation from anatase to titanate. In addition, the shift of peak T(020) to a smaller 2-theta value indicates the larger interlayer distance of G/TNS than TNS (Li et al. 2015, Liu et al. 2013, Hua et al. 2017). No graphene crystalline phase was evident because of its relatively low grafting content (2.0 wt.%) and the disordered stacking of graphene sheets in the composite material (Chen et al. 2011).
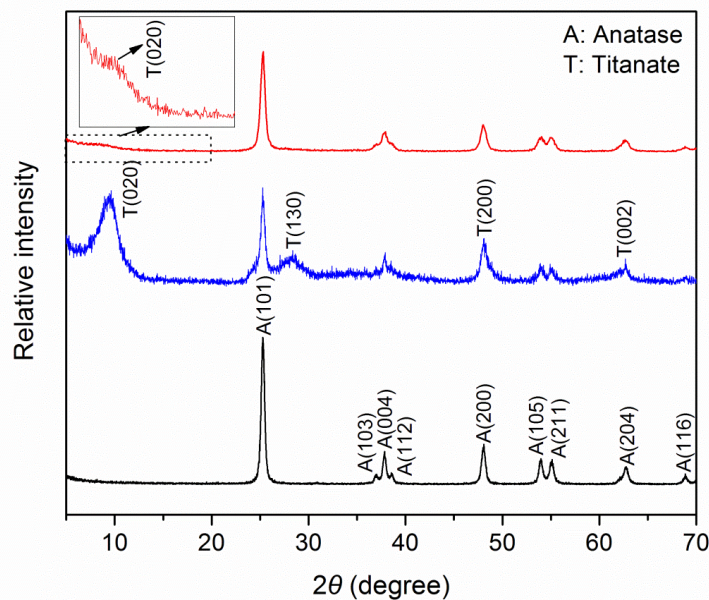
Figure 3-3. XRD patterns of TiO_2 (P25), TNS and G/TNS (with 2.0 wt.% graphene).

In the hydrothermal process, the Ti–O–Ti bonds in the [TiO$_6$] octahedrons are first broken into planar fragments under concentrated base (NaOH) attacking. Then the fragments are linked together through hydroxyl bridging, resulting in formation of TiO$_2$ nanosheets (Chen et al. 2002, Li et al. 2015, Wen et al. 2007). When further treated by concentrated NaOH and heat, the fragments will reassemble to form triple end-sharing [TiO$_6$] octahedrons, i.e., the formation of titanate nanosheets (Chen et al. 2002, Li et al. 2015, Wen et al. 2007). In the absence of graphene, the formed [TiO$_6$] fragments can easily undergo rearrangement to form triple end-sharing [TiO$_6$] octahedrons lattice, i.e., titanate nanosheets. However, the graphene grafted weakens this transformation. As a result, [TiO$_6$] fragments are assembled to mainly form anatase rather than titanate nanosheets.

The BET surface area of G/TNS (2.0 wt.%) was measured to be 108.0 m^2/g, and the large specific surface area along with the easy accessibility facilitates efficient mass transfer of 4-CP molecules to the material in the photocatalysis process (shown in the next Section). **Figure 3-4** shows N$_2$ adsorption-desorption isotherms of G/TNS, which is in accordance with the type IV isotherm with the H3 hysteresis loop according to classical BDDT classification and 2015 IUPAC classification (Brunauer et al. 1940, Thommes et al. 2015), suggesting the presence of mesopores (2–50 nm) in G/TNS. Moreover, the total single pore volume of G/TNS was calculated to be 0.34 cm^3/g. It is interesting that the pore size of G/TNS (2.0 wt.%) exhibits a trimodal distribution (**Figure 3-5**). The peaks at ~3 nm and 5 nm correspond to the interlayer distance between grafted graphene sheets and titania nanosheets, while the peak at ~200 nm is ascribed to the large gaps between the curled nanosheets and voids in the aggregates of the materials (Yu et al. 2003, Turki et al. 2013). The pH of point of zero charge (pH$_{PZC}$) was measured to be = 4.1. This relatively low value results from the hydrothermal treatment and

formation of abundant Ti−OH groups on the surface of the material (**Figure 3-6**) (Liu et al. 2013,

Ma et al. 2017).
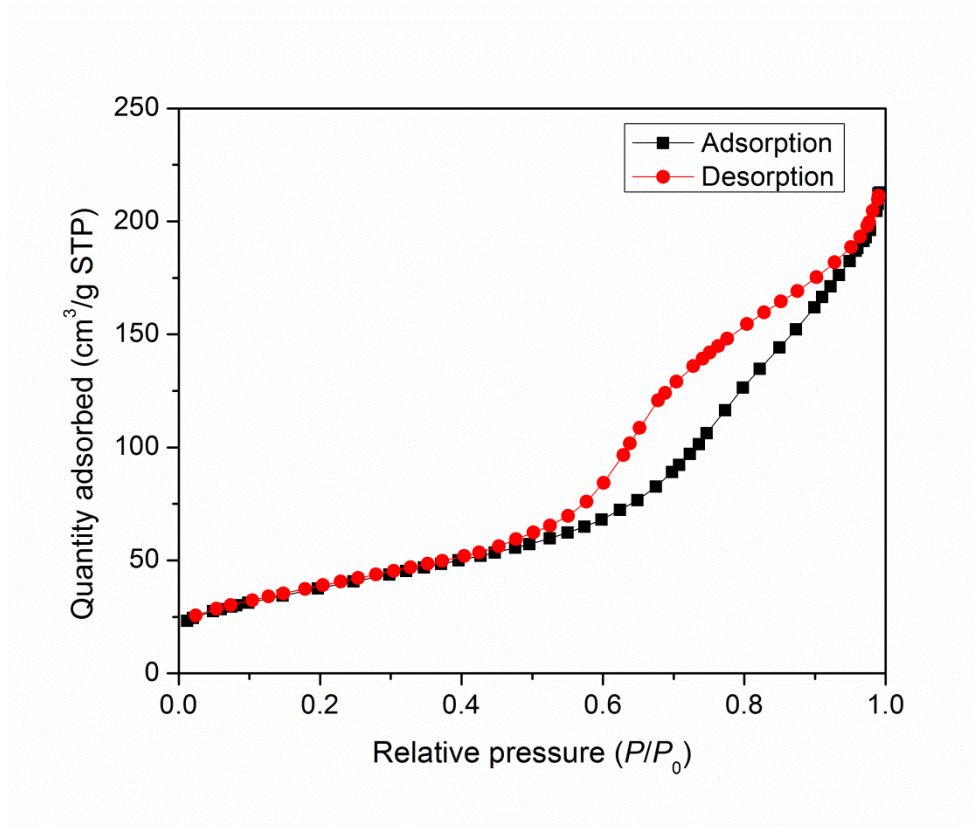
Figure 3-4. N_2 adsorption-desorption isotherms of G/TNS.
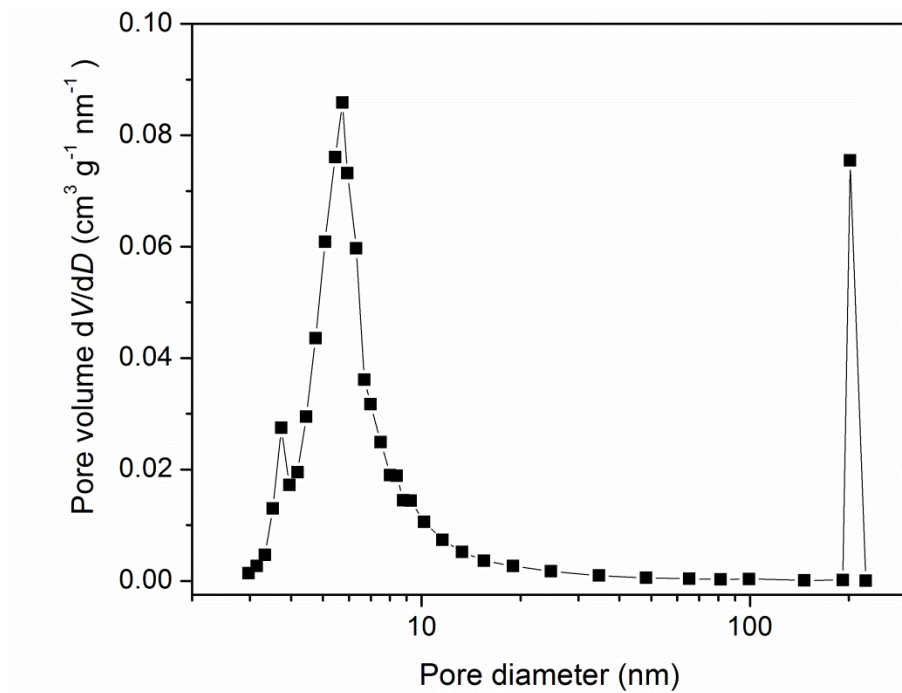
Figure 3-5. Pore size distribution of G/TNS.
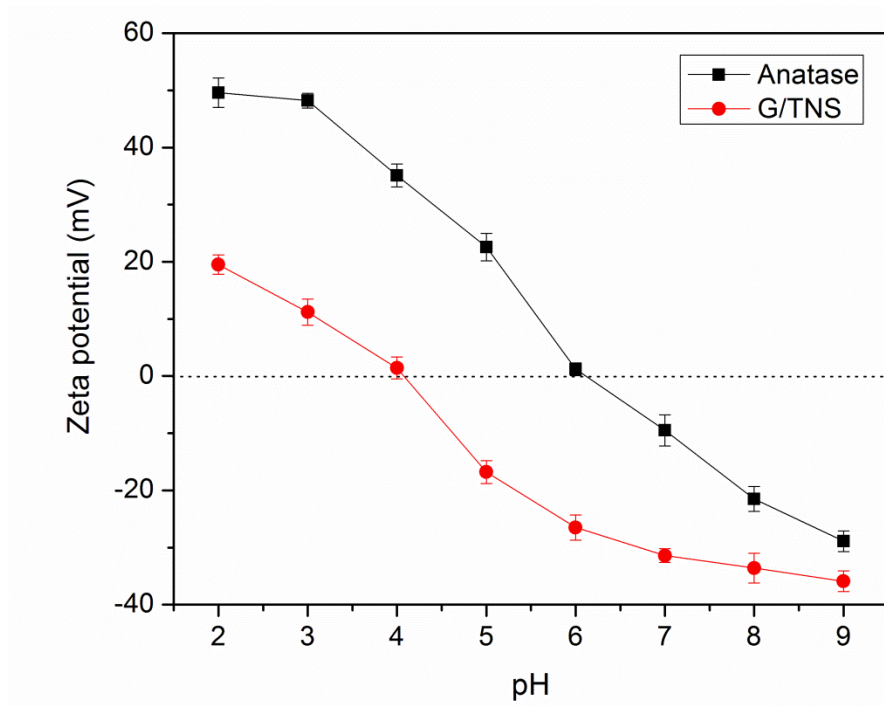
Figure 3-6. Zeta potentials of anatase and G/TNS at different pH.

3.3.2. Adsorption and photocatalytic degradation of 4-CP by G/TNS

Figure 3-7 shows adsorption of 4-CP by the original TNS and composite materials in the absence of light, including anatase, TNS, and G/TNS with various amounts of grafted graphene. Consistent with the previous studies (Zhao et al. 2016, Li et al. 2015), pure anatase and TNS could hardly adsorb the rather hydrophobic 4-CP (<1%) due to their inorganic structures and the negatively charged surface at pH 7 (Fig. S4). Yet, the adsorption capacity of 4-CP was proportional to the content of graphene grafted in G/TNS, though only 6.1% of 4-CP was removed at the maximum graphene content (2.5 wt.%) (Fig. S4). Overall, the adsorption kinetics was quite rapid but with only limited capacity. It is consistent with the adsorptive characteristics of graphene (Wang et al. 2013, Jin et al. 2015), where the dominant adsorption mechanisms are hydrophobic effects and π–π interactions (Wang et al. 2013, Jin et al. 2015). Strong adsorption may limit subsequent photodegradation of 4-CP, while small capture of 4-CP facilitated its transfer from solution to catalysis surface. Therefore, the modest adsorption capacity (4.8% 4-CP was removed by G/TNS with 2.0 wt.% graphene) is expected conducive to the following photocatalysis.
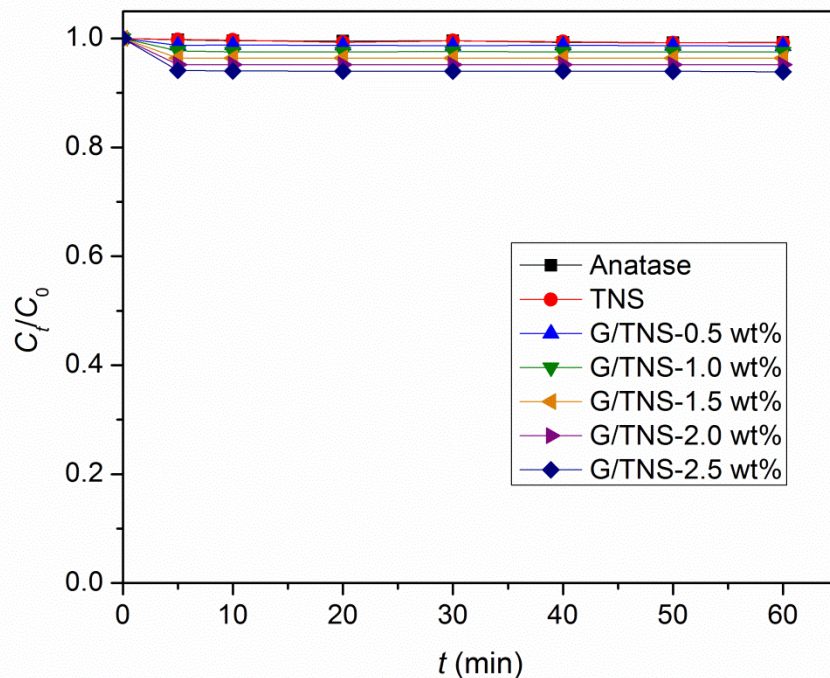
Figure 3-7. Adsorption kinetics of 4-CP by various materials (Initial 4-CP = 5 mg/L, material dosage = 0.2 g/L, pH = 7.0, T = 25 ± 0.2 °C).

Figure 3-8 presents photocatalytic degradation kinetics of 4-CP by various materials, and

Table 3-3 lists the simulated first-order model parameters. Within 2 hours, 41.5% of 4-CP was

degraded by TiO_2 (anatase) with a k_1 value of 0.005 min^{-1}. Generally, TiO_2 has almost no

response to visible irradiation from the solar light (Kumar and Devi 2011, Schneider et al. 2014),

and thus so the photodegradation is attributed to the small fraction of UV (~9%) of the solar

light. Pure TNS was found much less effective than anatase and removed only 21.7% of 4-CP at

120 min, with a k_1 value of 0.002 min^{-1}. Transformation of anatase to titanate will lead to lower

photocatalytic activity under solar light, because reduced light absorbance and the faster

recombination of electron-hole pairs after photo-excitation in the titanate phase (Yu et al. 2006,

Lee et al. 2007, Kim et al. 2014b). However, grafting of graphene onto TNS can overcome these

drawbacks, resulting in greatly enhanced photocatalytic activity. The k_1 value was increased to 0.008 min^{-1} when only 0.5 wt.% of graphene was grafted, and it was further increased to 0.041 min^{-1} at a graphene content of 2.0 wt.%, which is ~8 times higher than that for anatase and ~21 times that of TNS. More than 99.2% of 4-CP was rapidly photodegraded within 120 min by G/TNS with 2.0 wt.% graphene. Further increasing the graphene grafting to 2.5 wt.% only modestly increased the k_1 value to 0.048, while the relative coefficient (R^2) decreased to 0.9772 due to low remaining of 4-CP after 90 min. Therefore, G/TNS with 2.0 wt.% graphene was selected for further experiments.
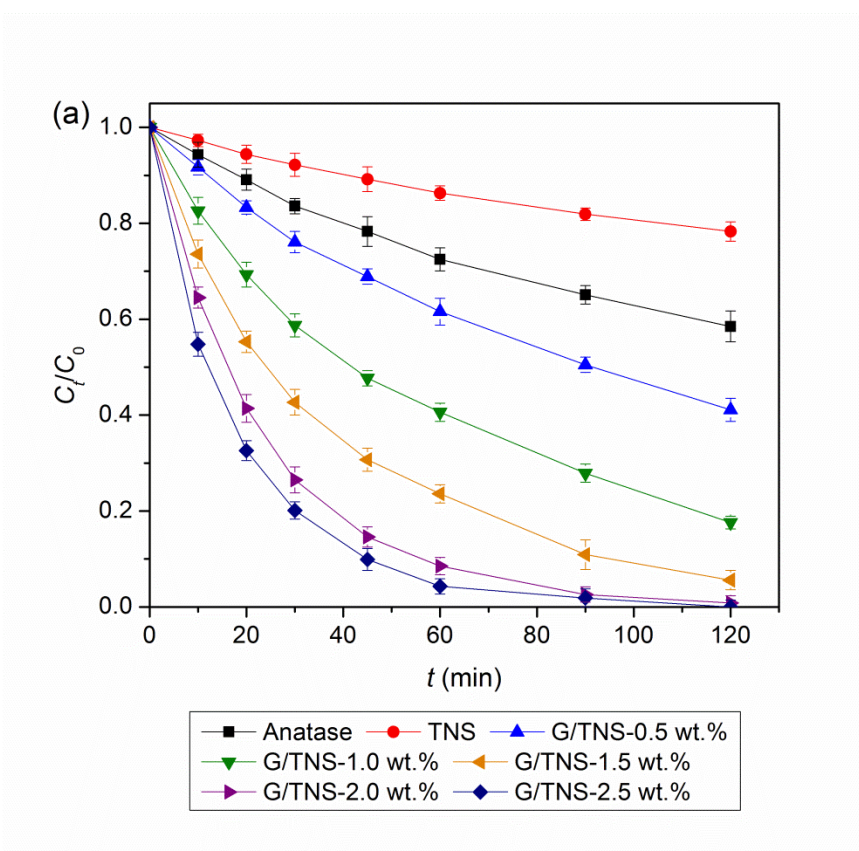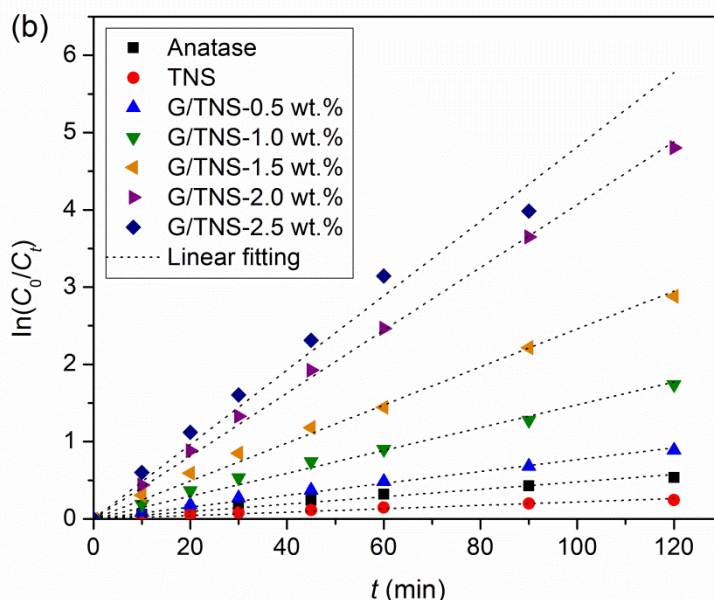
Figure 3-8. (a) Photocatalytic degradation kinetics of 4-CP by various materials under solar light; **(b)** linear first-order model fitting of the experimental kinetic data (Initial 4-CP = 5 mg/L, material dosage = 0.2 g/L, pH = 7.0, T = 25 ± 0.2 °C).

Table 3-3. Parameters of first-order kinetic models for degradation of 4-CP by various materials under solar light.

Materials	Parameters		Materials	Parameters	
	k_1 (min^{-1})	R^2		k_1 (min^{-1})	R^2
Anatase	0.005	0.974	G/TNS-1.5 wt%	0.025	0.994
TNS	0.002	0.978	G/TNS-2.0 wt%	0.041	0.998
G/TNS-0.5 wt%	0.008	0.992	G/TNS-2.5 wt%	0.048	0.977
G/TNS-1.0 wt%	0.015	0.989			

Contributions of visible light to 4-CP photocatalysis for the various materials were further examined by cutting off the UV light (**Figure 3-9**). Almost no removal of 4-CP (<4%) was found for anatase and TNS under visible light, indicating UV-light-driven photocatalysis is the primary mechanism for these materials. In contrast, G/TNS (2.0 wt.%) was able to remove 69.3% of 4-CP under visible light in 2 h, with a k_1 value of 0.011 min^{-1}. Therefore, of the 99.2% of 4-CP removal under solar light, 69.3% was attributed to visible light and 29.9% to UV irradiation, indicating that the graphene grafting greatly enhanced the material response to the visible spectra of solar light.
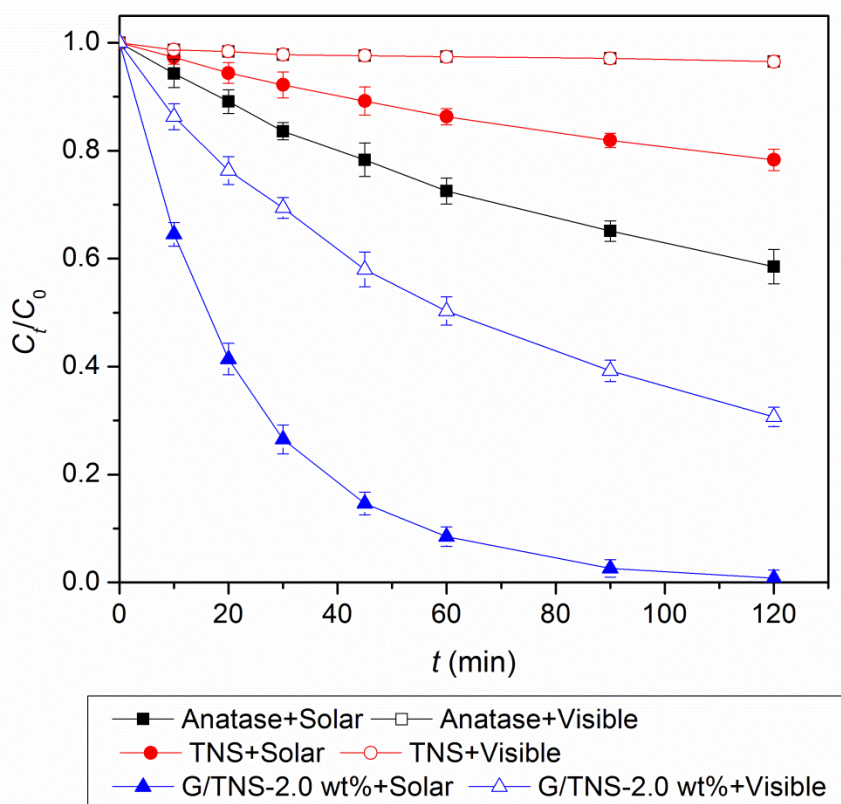
Figure 3-9. Comparison of photocatalytic degradation rates of 4-CP by anatase, TNS and G/TNS (with 2.0 wt% graphene) under solar or visible light (Initial 4-CP = 5 mg/L, material dosage = 0.2 g/L, pH = 7.0, T = 25 ± 0.2 °C).

3.3.3. Mechanisms on enhanced photocatalytic activity

Figure 3-10 illustrates the formation of G/TNS through hydrothermal reaction and the

photocatalytic reaction mechanisms. The hydrothermal treatment of the precursors causes

rearrangement and linkage of $[TiO_6]$ octahedrons in anatase, resulting in the TiO_2 and titanate

nanosheets. In the meanwhile, graphene sheets are split into nanoscale fragments and

incorporated into the Ti-nanosheets. Under solar irradiation, the electron (e^-, conduction band)

and hole (h^+, valence band) pairs are generated on TiO_2 and titanate after excitation (Eq. 3-4).

The photo-generated electrons are captured by O_2 to produce $\bullet O_2^-$, further leading to the

formation of $\bullet OH$ (Eqs. 3-6 and 3-8) (Zhao et al. 2012, Liu et al. 2014, Zhang et al. 2013, Zhang

et al. 2015). At the same time, H_2O molecules will be oxidized by h^+ to produce $\bullet OH$ (Eq. 3-7).

Finally, 4-CP is degraded by these ROS and even mineralized (Eq. 3-9) (Zhao et al. 2012, Liu et

al. 2014, Zhang et al. 2013, Zhang et al. 2015).

$$TiO_2/titanate + hv \rightarrow TiO_2/titanate^* \ (e^- - h^+) \tag{3-4}$$

$$graphene + e^- \rightarrow graphene - e^- \ (electron \ transfer) \tag{3-5}$$

$$O_2 + e^- \rightarrow \bullet O_2^- \tag{3-6}$$

$$H_2O + h^+ \rightarrow \bullet OH + H^+ \tag{3-7}$$

$$\bullet O_2^- + 2e^- + 2H^+ \rightarrow \bullet OH + OH^- \tag{3-8}$$

$$4\text{-}CP + OH/\bullet O_2^- \rightarrow intermediates \rightarrow products + CO_2 \tag{3-9}$$
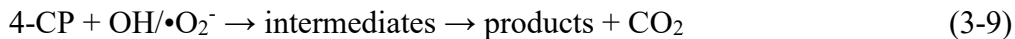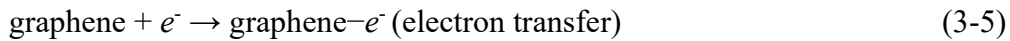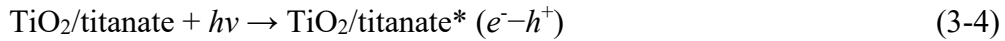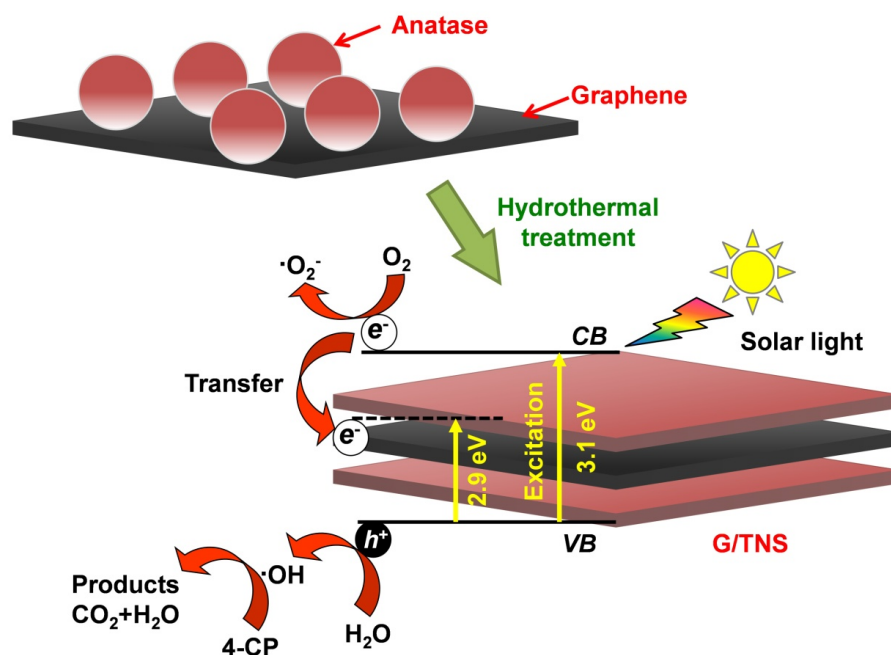
Figure 3-10. Schematic illustration of mechanisms for graphene enhanced photocatalytic activity of G/TNS.

Carbonaceous materials, such as activated carbon (Liu et al. 2016b), carbon nanotubes (Zhao et al. 2013), and graphene (Lee et al. 2012, Pan et al. 2012, Liang et al. 2010, Kim et al. 2011), have been widely used to modify conventional photocatalysts such as TiO_2 and titanate to enhance the photocatalytic activity, due to their excellent ability to transfer photo-excited electrons. Compared to other carbonaceous materials, graphene contains one-atom-thick two-dimensional layers of sp^2-bonded carbon, which exhibits a range of unusual properties, especially the extraordinary electron transport capability (Stankovich et al. 2006). The grafted graphene in G/TNS plays several important roles in enhancing the photocatalytic degradation of 4-CP. First, its moderate adsorption property facilitates adsorption of the aromatic organic compound through π−π stacking and hydrophobic interactions (Wang et al. 2013). Such initial adsorption concentrates 4-CP molecules onto the catalytic surface (Perera et al. 2012), thus greatly facilitating the subsequent photocatalytic reaction. Second, the grafted graphene can

greatly facilitate solar-light-driven photocatalytic activity of the material. On one hand, the

grafted graphene can rapidly transfer electrons, and thus inhibit the electron-hole recombination

(Eq. 5) (Lee et al. 2012, Pan et al. 2012, Liang et al. 2010, Kim et al. 2011). On the other hand,

the light absorption edge of G/TNS shifts to the visible range with a reduced energy band gap (E_g

= 2.9 eV) compared to TNS (E_g= 3.1 eV) (Fig. S5) (Liu et al. 2016a, Lee et al. 2012, Pan et al.

2012, Liang et al. 2010, Kim et al. 2011). The UV-vis DRS spectra also indicate the light

absorbance is enhanced in the range of 350–700 nm due to incorporation of graphene (**Figure 3-**

11). Therefore, the grafting of graphene into G/TNS enhances the production of ROS (especially

•OH), and thus promotes the photocatalytic degradation of 4-CP under visible light.
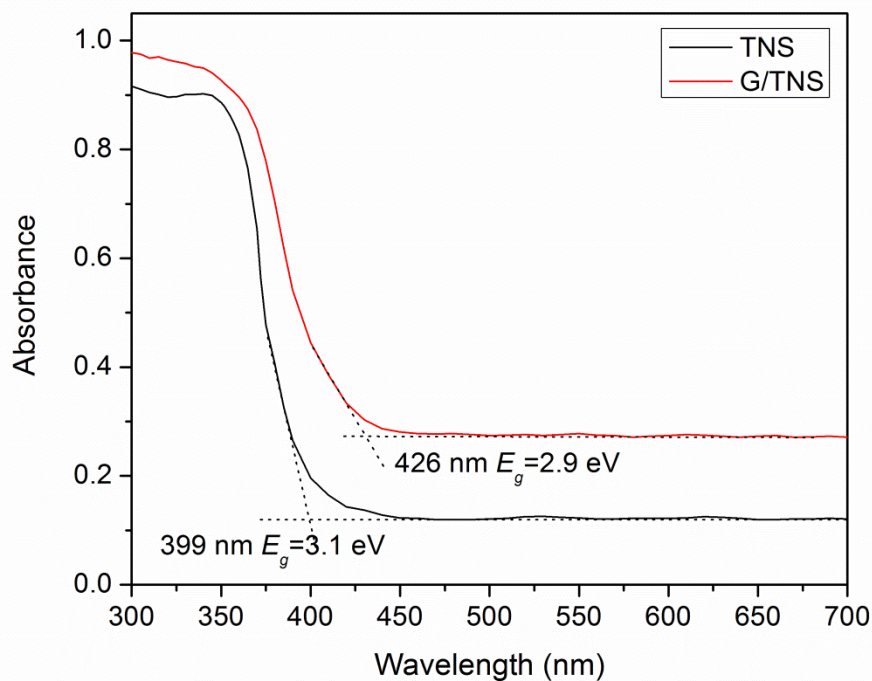
Figure 3-11. Absorbance UV-vis diffuse reflectance spectra (DRS) of TNS and G/TNS (2.0 wt.%).

Roles of h^+ and ROS (•OH and •O_2^-) in the photocatalytic degradation of 4-CP by G/TNS

(2.0 wt.%) were further investigated through the classical scavenger-quenching methods (Guo et

al. 2013, Cao et al. 2012) (**Figure 3-12**). The addition of KI and isopropanol remarkably

inhibited the photocatalytic reaction, decreasing the final 4-CP removal efficiency from 99.2% to

4.6% and 13.7%, respectively. Therefore, •OH-driven reactions are the primary mechanism for

4-CP degradation in this study, and it has been known that and •OH radicals play a dominant role

in various photocatalysis systems in the presence of Ti-based materials (Kumar and Devi 2011,

Schneider et al. 2014, Ishibashi et al. 2000). Moreover, inhibition on h^+ formation will diminish

the •OH production as shown in Eq. 3-7. In comparison, the results indicate that •O_2^- played a

less important role in the 4-CP degradation process as BQ showed only slight inhibition effect.
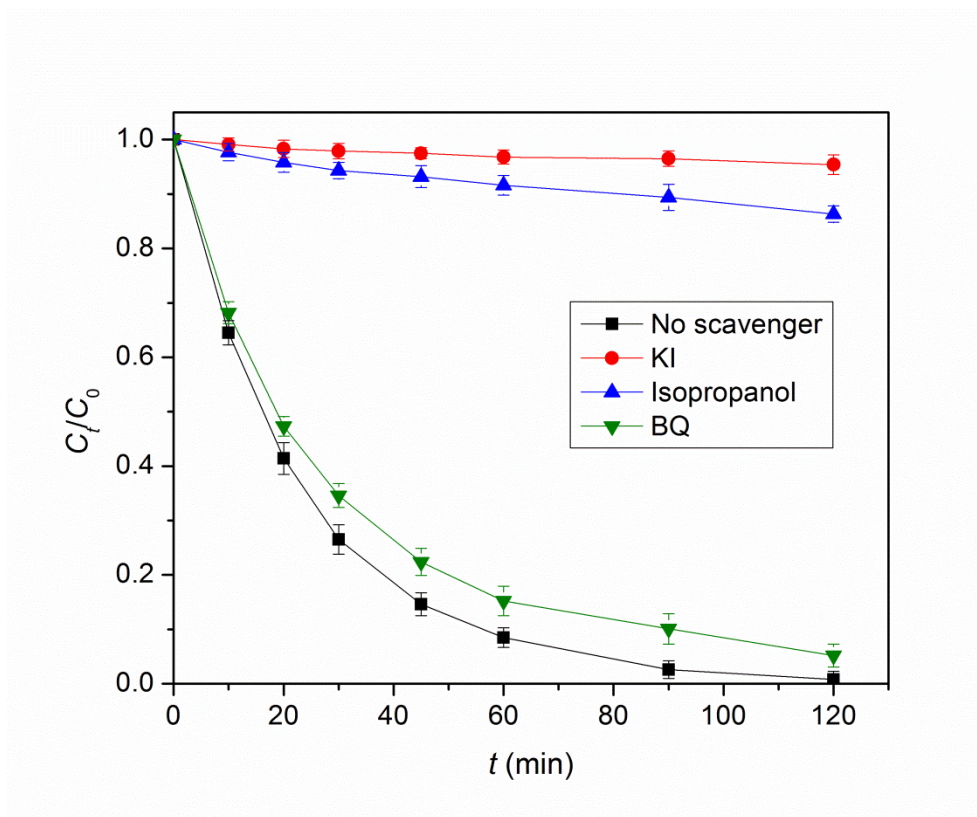
Figure 3-12. Photocatalytic degradation of 4-CP by G/TNS (with 2.0 wt% graphene) under

solar light in the presence of various radical scavengers (Initial 4-CP = 5 mg/L, material dosage = 0.2 g/L, scavenger concentration = 1 mM, pH = 7.0, T = 25 ± 0.2 °C).

The production of •OH by different materials under solar light at 1 h was recorded through the photoluminescence (PL) method. Fig. 8 shows that the fluorescence intensity of the 2-hydroxyterephthalic acid produced in the presence of G/TNS (2.0 wt.%) reached up to 4.0×10^3 a.u., which was 2.5 times higher than that of anatase (1.6×10^3 a.u.) and 3.6 times that for TNS (1.1×10^3 a.u.), indicating much greater •OH yield in the G/TNS system. Evidently, the amount of •OH produced is in accordance with the 4-CP degradation results.
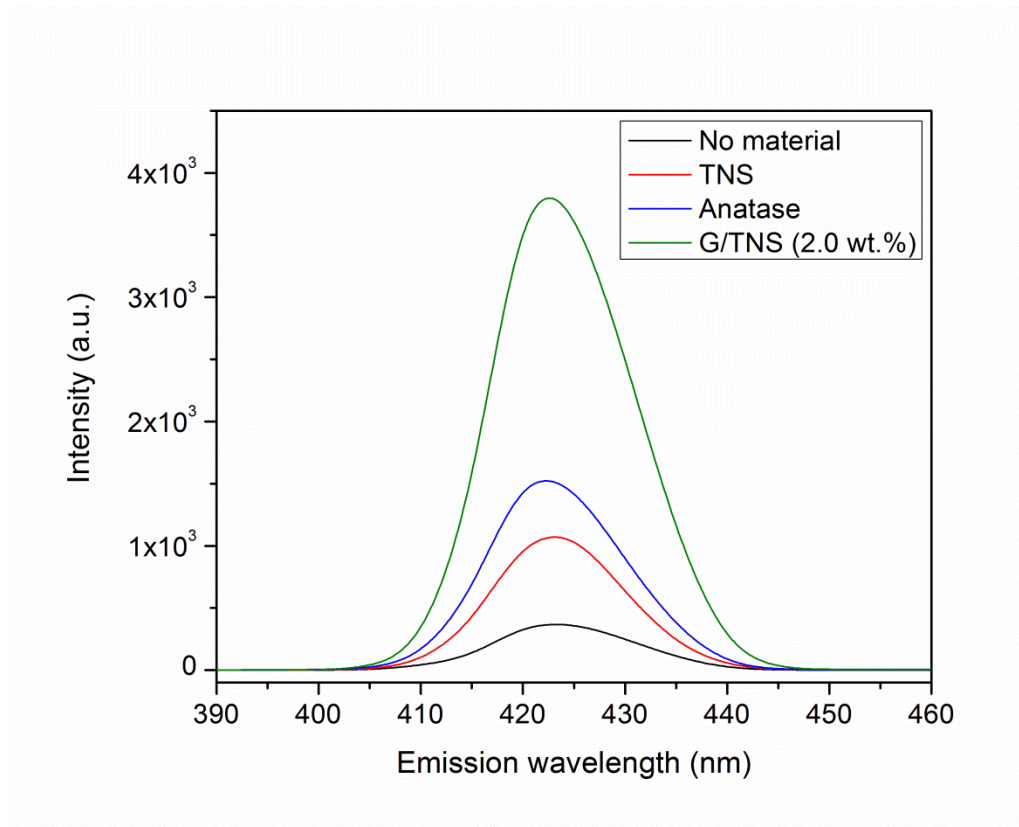
Figure 3-13. PL spectra of photocatalysis systems in the presence of different materials after solar irradiation for 1 h.

3.3.4. Photocatalytic degradation pathway and computational chemistry analysis

The highest occupied molecular orbital (HOMO) and the lowest unoccupied molecular orbital (LUMO) cannot accurately explain the reactive sites of 4-CP for •OH radical attacking. Fukui index distribution related to radical attacking was further calculated based on DFT. **Figure 3-14** displays the Fukui index (f^-) distribution on a 4-CP molecule, and Fig. 10 depicts the proposed 4-CP degradation pathway. •OH is the primary ROS for 4-CP degradation in this system. The Fukui index indicates the ability of electron escape from the different sites of a 4-CP molecule, and •OH prefers to attack the sites with higher f^- values (De Vleeschouwer et al. 2007). As shown in Figs. 8a and 8c, C4 has the highest Fukui index value ($f^- = 0.125$), and thus is the most reactive site, which is consistent with the intermediates detected by LC-MS (Fig. 10). Although C1 also shows a high f^- value (0.108), this C site is saturated and cannot further accept •OH. Therefore, C6 with an f^- value of 0.074 is the second most reactive site, which is highly vulnerable to •OH attacking (Fig. 9a). Specifically, C4 site is first attacked by •OH, which cleaves the C-Cl bond, leading to formation of hydroquinone ($m/z = 109$) (**Figure 3-15**). Further, benzoquinone ($m/z = 107$) is formed through a two successive one-electron oxidation process (Pathway A→B→C in Fig. 10) (Huang et al. 2008, Du et al. 2016). On the other hand, •OH also attacks the C6 site, resulting in generation of 4-chlorocatechol ($m/z = 144$) and then hydroxy hydroquinone ($m/z = 125$) (Pathway A→D→E in Fig. 10). As the reaction proceeds, the intermediates are further broken down into small carboxylic and aliphatic compounds, until complete mineralization given sufficient reaction time (Huang et al. 2008, Ai et al. 2005b, Johnson et al. 1999, Cheng et al. 2007, Zhao et al. 2010). The proposed pathway is in accordance with the conventional reactions of 4-CP with •OH despite much enhanced degradation efficiency (Huang et al. 2008, Ai et al. 2005b, Johnson et al. 1999, Cheng et al. 2007, Zhao et al. 2010).

(a)

OH

0.064   0.074

0.042   0.026

0.125

Cl

(b)

No.	Atom	Charge (0) (e/Å³)	Charge (+1) (e/Å³)	f^-
1	C	0.306	0.414	0.108
2	C	-0.305	-0.242	0.064
3	C	-0.236	-0.195	0.042
4	C	-0.082	0.043	0.125
5	C	-0.236	-0.209	0.026
6	C	-0.274	-0.200	0.074
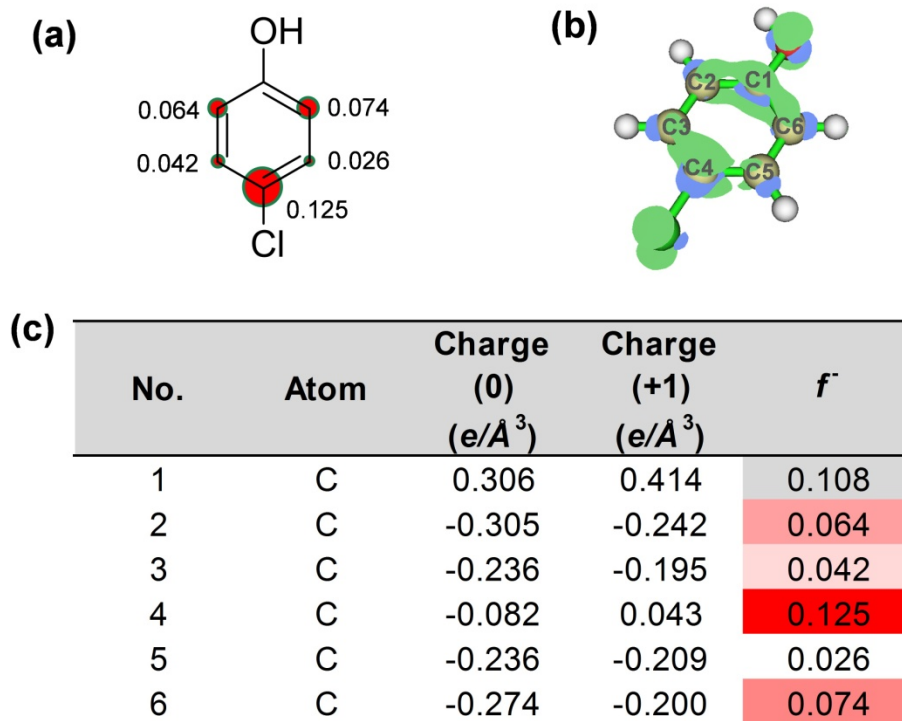
Figure 3-14. The atomic contributions to Fukui index (electrophilic attack) for 4-CP. (a) Fukui index (f -) distribution on 4-CP; (b) Spatial Fukui index density on 4-CP; (c) NPA charge distribution on 4-CP at different electron states and calculated Fukui index (f -).
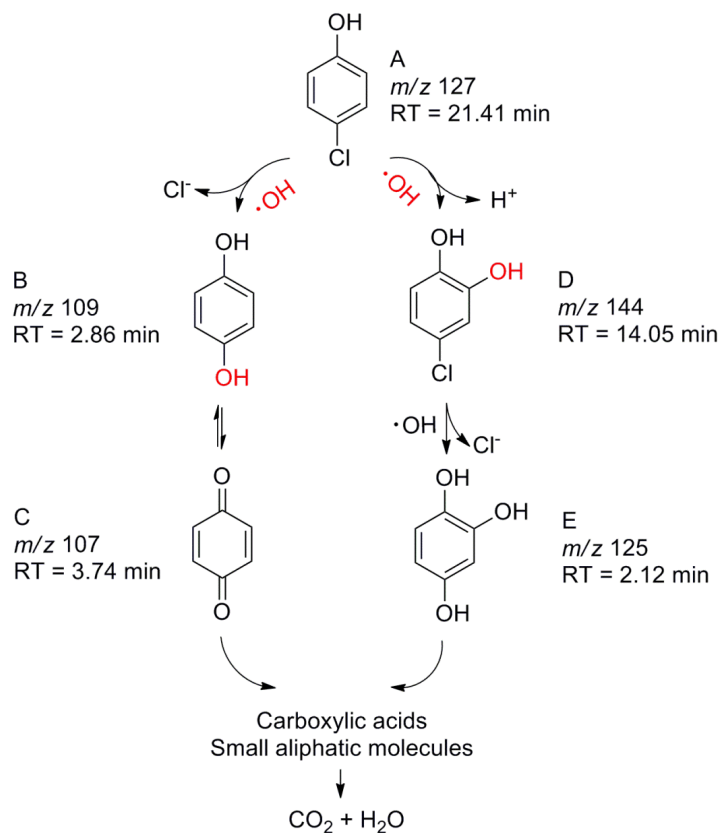
Figure 3-15. Degradation pathway of 4-CP by G/TNS under solar irradiation.

3.3.5. Reusability of G/TNS for 4-CP photocatalysis

Figure 3-16 presents the 4-CP photocatalytic degradation profiles when the same G/TNS (2.0 wt.%) was repeatedly used over 5 operating cycles without any treatment. About 90.3% of 4-CP was rapidly (within 2 h) degraded in the 5th cycle. In addition, almost no Ti (<1%) was dissolved from photocatalyst into solution after the 5 cycles (**Table 3-4**), owing to the good stability of the precursors TiO_2 and titanate (Bavykin et al. 2006a, Bavykin et al. 2006b). In addition, dissolution tests indicated that only 8.3% of Ti was dissolved at low pH (4), while <1% of dissolution was observed when pH $\geq$5 at 120 min. The rather good material stability and reusability warrant G/TNS is a promising material for effective degradation of persistent organic pollutants under natural light.
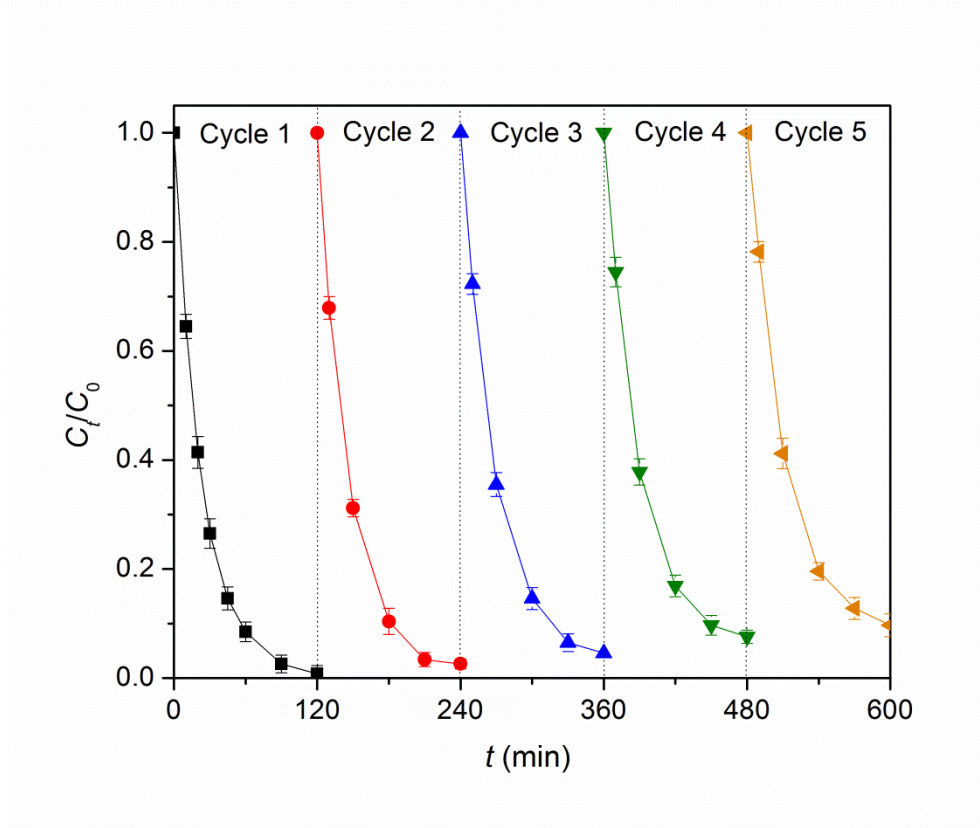
Figure 3-16. Photodegradation of 4-CP using the same G/TNS (with 2.0 wt.% graphene) over 5 operating cycles (Initial 4-CP = 5 mg/L, material dosage = 0.2 g/L, pH = 7.0, T = 25 ± 0.2 °C).

Table 3-4. Dissolution of Ti from G/TNS (2.0 wt.%) in 5 reuse cycles.

Cycle	Dissolution (wt.%)
1	0.07
2	0.11
3	0.13
4	0.17
5	0.23

3.4. Conclusions

A new photocatalyst, graphene grafted TiO_2/titanate nanosheets, was synthesized through a one-step alkaline hydrothermal method. The new material showed excellent photocatalytic activity for degradation of 4-CP under solar light. The main findings of this study are summarized as follows:

(1) G/TNS are structured as flower-like nanosheets. The primary phase of G/TNS is anatase, while sodium titanate is also formed during the hydrothermal reaction. Graphene acts as a 2-D template for the growth of the Ti-nanosheets, and the presence of graphene inhibits transformation of anatase to titanate.

(2) G/TNS with 2.0 wt.% of graphene grafted showed the most efficient photocatalytic activity under solar irradiation. The pseudo first-order rate constant for 4-CP degradation was measured to be 0.041 min^{-1}, which is ~8 times higher than that of anatase and ~21 times that of unmodified TNS.

(3) Grafting of graphene can greatly enhance the photocatalytic activity. On one hand, graphene can facilitate rapid transfer of photo-excited electrons, thus inhibiting recombination of the h^+-e^- pairs; On the other hand, the shift of the light absorption edge to the visible light range along with narrowed band gap energy also facilitates solar light irradiation activity.

(4) The •OH radicals played the most important role in 4-CP photocatalytic degradation by G/TNS. The degradation pathway was interpreted through computational chemistry analysis based on the DFT. The C4 and C6 sites on 4-CP are identified as the most reactive sites for •OH attacking based on the Fukui index values. The computational results were confirmed by the reaction intermediates that were experimentally identified.

(5) G/TNS can be efficiently reused and >90% of 4-CP was still degraded after 5 reuse cycles.

G/TNS holds the promise for effective photocatalytic degradation of persistent organic pollutants under solar light. The facile synthesis procedure, high activity, good reusability and physical stability merits G/TNS great application potential in practical environmental remediation practices.

Chapter 4: "Concentrate-&-destroy": an advanced approach of 4-chlorophenol removal using titanate nanotube based adsorptive photocatalyst

In the third study, an adsorptive photocatalyst (TNTs@AC) was prepared by modifying TNTs with a commercial AC for rapid removal of 4-CP in water through the "concentrate-&-destroy" approach. TNTs@AC   showed both high adsorption capacity and photocatalytic activity towards 4-CP. Coating TNTs with nanoscale carbon not only enhanced hydrophobic interactions, but induced a capillary condensation mechanism, resulting in enhanced 4-CP adsorption. Moreover, the carbon quantum dots also facilitated photo-excited electron transfer, resulting in greater photocatalytic activity. The efficient photodegradation of pre-concentrated 4-CP also regenerates the material. After 5 cycles of repeated uses, TNTs@AC showed no significant drop in 4-CP adsorption capacity. The composite also demonstrated strong resistance to dissolved organic matter (DOM) and salinity.

4.1. Introduction

Chlorinated phenols (CPs) are widespread in wastewaters originating from multiple industrial processes including tanning, and manufacturing of preservatives, pesticides and

antifouling agents (Sorokin et al., 1995; Sze and McKay, 2012). As emerging contaminants, CPs have drawn substantial attention for its high toxicity towards aquatic organisms and excessive carcinogenicity risk to human health. Meanwhile, CPs are rather persistent to natural degradation and have already been listed as persistent organic pollutants (POPs) due to their stable molecular structure and the C-Cl bond (Jones and De Voogt, 1999; Wania and Mackay, 1996). To eliminate the risks and toxic effects of CPs, people developed abundant technology approaches for CPs removal from wastewater. Adsorption of CPs using activated carbon/charcoal (AC) (Dąbrowski et al., 2005) and synthetic resins (Lin and Juang, 2009) are generally efficient and safe due to strong and irreversible hydrophobic attraction between sorbents and CPs. But AC/resins regeneration would be costly and eco-unfriendly (Zhang and Chuang, 2001). In addition, ozonation (Pi et al., 2007), Fenton system (Pérez-Moya et al., 2007), Fenton-like system (Yin et al., 2014) and photo assisted Fenton system (Pérez-Moya et al., 2007) were tested for CPs removal. Although CPs could be removed and mineralized effectually by these approaches, the cost was still too high to afford in full-scale wastewater treatment processes.

To this end, we believe that photocatalysis approach would be an ultimate solution for CPs removal. Photocatalysis process could efficiently and copiously generate hydroxyl radical which was recognized as dominant reactive oxygen species (ROS) ensuing CPs decomposition (Li et al., 2018; Pérez-Moya et al., 2007). Various CPs, such as 2,4,6-trichlorophenol (2,4,6-TCP), 2,4-dichlorophenol (2,4-DCP), 4-chlorophenol (4-CP), 2-chlorophenol (2-CP), etc. have been reported to be photodegradable by titanium-based materials (Ai et al., 2005; Dionysiou et al., 2000; Khuzwayo and Chirwa, 2015) which are the most used photocatalysts. Titanium-based

materials include TiO_2, titanate, and TiO_2-modified materials. TiO_2 is a standard industrial photocatalyst with excellent photo-electrical response to the UV spectrum. Titanate materials are derived from TiO_2 and would offer larger specific surface area and better ion-exchange capacity than TiO_2 (Bavykin et al., 2006). But comparing with TiO_2, the photocatalytic activity of titanate is slightly weaken by rapid hole-electron pair recombination after UV excitation (Bavykin et al., 2006; Ou and Lo, 2007). In previous work, we synthesized a nanocomposite of anatase/titanate nanosheet (TNS), which combined the advantages of TiO_2 and titanate together and was further able to simultaneously remove Cr(VI) and 4-CP through photocatalysis (Liu et al., 2016b). But TNS just showed limited response to visible light, therefore weakening its application pretential upon solar energy. Afterwards, we induced graphene as a two-dimensional template for growth of anatase/titanate nanosheet and synthesized graphene grafted titania/titanate nanosheets (G/TNS) through a one-step hydrothermal treatment (Li et al., 2018). We observed graphene could efficiently transfer photo-excited electrons and enhance visible light absorption. The highest 4-CP photocatalytic degradation rate (99.2% at 120 min) was achieved by G/TNS with 2.0 wt.% graphene under simulated solar light. We also confirmed that hydroxyl radicals (·OH) attack on reactive sites on 4-CP with high Fukui index resulted the rapid photodegradation in this work.

Then, when we try to scale up our treatment technology, we realized that we were facing an awkward situation of so-called "using cannon to shoot birds". Most time, contaminated water body (e.g. wastewater or domestic sewage) has a large volume but trace level POPs. As consequences, we must either build a huge reactor with numerous UV light source to sacrifice

low-cost property or shorten the hydraulic retention time to sacrifice removal efficiency. In

addition, photocatalysts collection for reuse was also difficult after each batch. Briefly, reactor

design is the real "bottleneck" for using photocatalysis approach to remove POPs (Loeb et al.,

2019). For this issue, we proposed a "concentrate-&-destroy" approach using novel adsorptive

photocatalyst (**Figure 4-1**). Initially, trace level POPs could be adsorbed on our adsorptive

photocatalysts to avoid treating large volume polluted water using photocatalysis approach.

Afterwards, POPs loaded adsorptive photocatalyst would be easily separated by gravity settle

down and subjected to photocatalytic regeneration. Simultaneously, the POPs would be

decomposed, or even completely mineralized. Then, regenerated adsorptive photocatalysts would

be reused for POPs concentration in a new "concentrate-&-destroy" cycle.
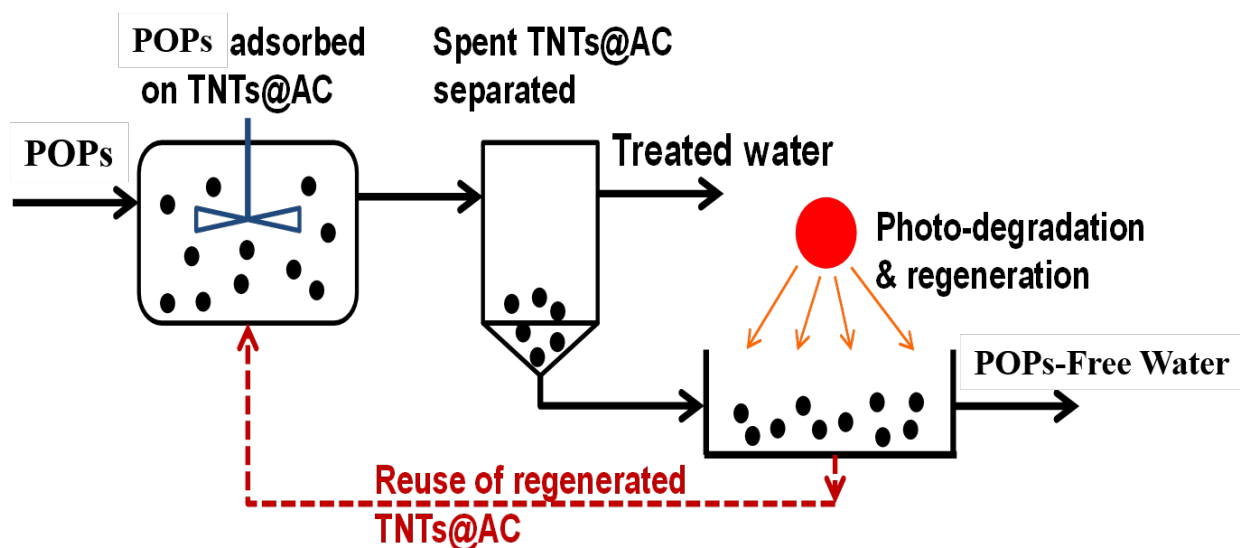
Figure 4-1. Schematic illustration of "concentrate-&-destroy" approach.

Previously, we synthesized the activated carbon modified titanate nanotube (TNTs@AC) for

phenanthrene removal.(Liu et al., 2016a) We observed that condensation effect can greatly
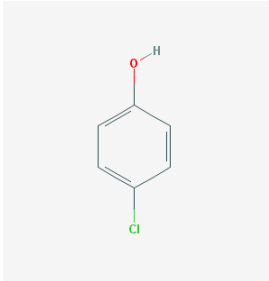
enhance phenanthrene adsorption. Additionally, "micro-carbon" on titanate nanotube can improve photocatalytic activity through preventing photo-generated hole-electron pair recombination and facilitating broader photo wavelength irradiation. Ultimately, phenanthrene could be efficiently photodegraded by photo-generated hydroxyl radicals. Therefore, we believe that application of TNTs@AC following "concentrate-&-destroy" would be an ideal method for 4-CP removal since 4-CP could be straightforwardly adsorbed by AC(Dąbrowski et al., 2005) and hydroxyl radical is dominant ROS result in 4-CP degradation (Li et al., 2018; Liu et al., 2016b).

4.2. Materials and methods

4.2.1. Chemicals and reagents

All chemicals used in this study were of analytical grade or better. Nano-TiO_2 (P25, 80% anatase and 20% rutile) was purchased from Evonik (Worms, Germany). Sodium hydroxide (Granular) and absolute ethanol were obtained from Acros Organics (Fair Lawn, NJ, USA). Powder activated charcoal (100 mesh) was obtained from Sigma-Aldrich (St. Louis, MO, USA) and used without further amendment. This PAC has relatively larger pore size to prevent fouling issue or pore clogging issue. Besides, this PAC can be slowly released during alkaline hydrothermal treatment to modify the TNTs and further benefit adsorption and photodegradation of target pollutant. 4-CP (physicochemical properties shown in Table 4-1) was acquired from Alfa Aesar (Ward Hill, MA, USA), and a stock solution (1000 mg/L) was prepared and stored at 4 °C. All solutions were prepared using de-ionized (DI) water (18.2 MΩ cm, Millipore Co., USA).

Table 4-1. Physicochemical property of 4-CP

parameters	values [a]
chemical formula	C_6H_5ClO
chemical structure	
molecule weight	128.56 g/mol
*pK*a	9.41
Log *K*ow	2.39
solubility in water	2.71 g/100 mL (20 °C, pH 6)
CAS Number	335-93-3

4.2.2. Synthesis and Characterization of TNTs@AC

TNTs@AC was synthesized through a facial alkaline hydrothermal treatment as previous work (Liu et al., 2016a). Specifically, 1.2 g of TiO_2 was mixed with 2.4 g of PAC and then dispersed into 67 mL of a 10 M NaOH solution. After stirring for 12 h, the mixture was transferred into a Teflon reactor and heated at 130 °C for 72 h. Later, the gray precipitates, i.e., TNTs@AC, were washed with deionized (DI) water until neutral pH, and then oven-dried at 105 °C for 24 h. afterwards, composite materials were stored at 25°C for further experiments.

The surface morphology of TNTs@AC was imaged using a scanning electron microscope (SEM) (20 kV; FEI XL30F, Philips, USA). The Brunauer–Emmett–Teller (BET) surface area was measured using an ASAP 2010 BET surface area analyzer (Micromeritics, USA) with the relative pressure (P/P0) range of 0.06–0.20. The Barret-Joyner-Halender (BJH) method was followed to determine the pore size distribution. The nitrogen adsorption at the relative pressure of 0.99 was obtained for the pore volumes and the average pore diameters.

4.2.3. 4-CP Adsorption Kinetic and Isotherm Experiments

4-CP adsorption kinetic experiments were performed by using brown glass vials (40 mL) with Teflon-lined caps in darkness. The experiments in this section were initiated by adding TNTs@AC (or other materials) into the 4-CP solutions and then the change in 4-CP concentration was followed for 4 h at predetermined time under shaking at 150 rpm. The vials were sacrificially sampled. Adsorption kinetic were performed at pH 7 with an initial concentration of 4-CP of 8 mg/L and various of TNTs@AC dosage (0.2, 0.3, or 0.5 g/L). Upon centrifuging at 6000 rpm (4800 g-force) for 10 min, the supernatants were sampled and analyzed for-4-CP. For comparison, 4-CP adsorption kinetics by original untreated PAC and alkaline hydrothermal treatment treated AC (AC-treated) were also tested. Adsorption isotherms were carried out in similar method with an initial 4-CP concentration of 2-100 mg/L and a fixed TNTs@AC dosage of 0.2 g/L at pH 7, and the mixtures were equilibrated for 24 h under shaking. For comparison, adsorption isotherms by AC, and TNTs were also performed. To probe effects of pH on adsorption, the equilibrium tests were carried out with initial 4-CP concentration of 8 mg/L, a TNTs@AC dosage of 0.2 g/L, and final solution pH 2−11 (adjusted using dilute

HCl and NaOH). To quantify the effects of ionic strength, the tests were carried out in the presence of 0−10 mM of NaCl and CaCl$_2$. Similarly, effects of humic acid on adsorption were also tested by measuring equilibrium uptake of 4-CP in the presence of 0−10 mg/L as TOC of LHA. To test the adsorption reversibility, desorption isotherms OF 4-CP were obtained. Specifically, the supernatant in each vial was replaced with 40 mL of deionized water after the adsorption isotherm tests, and then re-equilibrated for 24 h. The equilibrium distribution of 4-CP was then measured in the same fashion as in the adsorption equilibrium tests. All experiments in this section were at least duplicated.

4.2.4. Photodegradation of 4-CP and Reuse of TNTs@AC

Reuse of spent TNTs@AC was achieved through photodegradation of pre-loaded 4-CP on TNTs@AC. Following the adsorption equilibrium, the mixtures were left still for 1 h to allow the composite materials to settle by gravity (>99% of the materials settled). Then, ~95% of the supernatant was pipetted out, and the residual solid-liquid mixture was transferred into a quartz photo-reactor with a quartz cover. Then, 2 or 4 mL of DI water was added to the mixture so that the solution volume in the photo-reactor reached 4 or 6 mL (i.e., soli:solution = 1:20), and the solution pH was adjusted to 7.0. The reactor was then placed under UV light (254 nm, 1.28 mW/cm^2). After predetermined time (i.e. 1, 2, 3, 4 h) of UV irradiation, the liquid was decanted and the solid was extracted for remaining 4-CP using 40 mL of methanol at 80 °C for 4 h. 4-CP recovery efficiency was > 87%. After 4 h of photo-regeneration, TNTs@AC was then re-submitted in another cycle to adsorb and degrade 4-CP. The "concentrate-&-destroy" cycle were

repeated five times to probe the feasibility of the concept. All experiments in this section were at least duplicated.

4.2.5. Analytical Methods

4-CP concentration was analyzed using an Agilent 1100 high-performance liquid chromatography (HPLC) with the Zorbax SB-C18 column (2.1 mm × 150 mm, 5 μm) and a diode array detector (DAD). A mixture of ultrapure water and methanol (HPLC grade) (v/v of 40:60) was used as the isocratic eluent at a flow rate of 0.2 mL/min under 25 °C. The eluate was analyzed at an UV array detector of 280 nm. After calibration and verification, limit of quantitation was as low as 20 μg/L.

4.3. Results and Discussion

4.3.1. Characterization of TNTs@AC

Figure 4-2 is the scanning electron microscope (SEM) images of TNTs@AC. In previous work, we observed that same AC used for TNTs@AC synthesis has a bulky, flat, and smooth surface (Liu et al., 2016a). Whereas the surface of TNTs@AC appeared rather rough and full of clusters of aggregates (**Figure 4-2a**). A close-up of the surface revealed that the tubular TNTs formed an interweaved network spreading throughout the surface (**Figure 4-2b and c**). The length of the nanotubes stretched up to hundreds of nanometers. Additionally, TNTs were not only simply coated on AC, rather the PAC are intermingled with nanotubes, i.e., some AC ("micro-carbon") is also coated on TNTs.
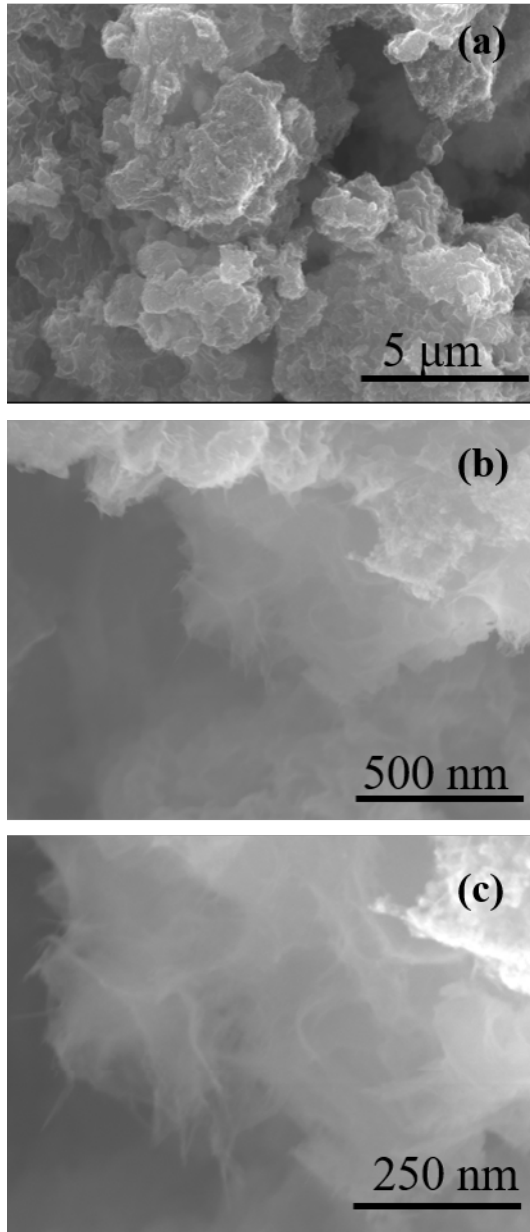
Figure 4-2. SEM image of (a,b, and c) TNTs@AC

The AC modification of TNTs increased the measured BET surface area from 272.3 m^2 /g

for neat TNTs (Liu et al., 2016a) to 481.4 m^2 /g for TNTs@AC, which is closed to results (471.6

m^2 /g) in previous work(Liu et al., 2016a). But the pore volume decreased from 1.26 to 0.67 cm^3

/g. Meanwhile, the PAC has a BET surface area of 593.4 m^2 /g and pore volume of 0.64 cm^3 /g

(**Table 4-2**). Given the composition ratio of TNTs@AC (mass ratio: AC/TNTs = 1.7:1), the

measured BET surface area of TNTs@AC is close to the calculated value 478.8 m^2/g, suggesting

that the hydrothermal treatment did not significantly alter the AC surface area. TNTs@AC

displays a bimodal pore size distribution profile with a primary peaking at ~4 nm and a

secondary peaking at 2−2.5 nm (**Figure 4-3b**), which can be assigned to the pores of PAC and

conversion of larger pores (>10 nm) of TNTs into more micropores in TNTs@AC, respectively

(Xiong et al., 2011).

Table 4-2. Key physical parameters of PAC and TNTs@AC

Material	BET surface area (m^2/g)	Single point total pore volume (cm^3/g)	Average pore diameter (nm)
PAC	593.4	0.61	4.53
TNTs@AC	481.4	0.67	4.17
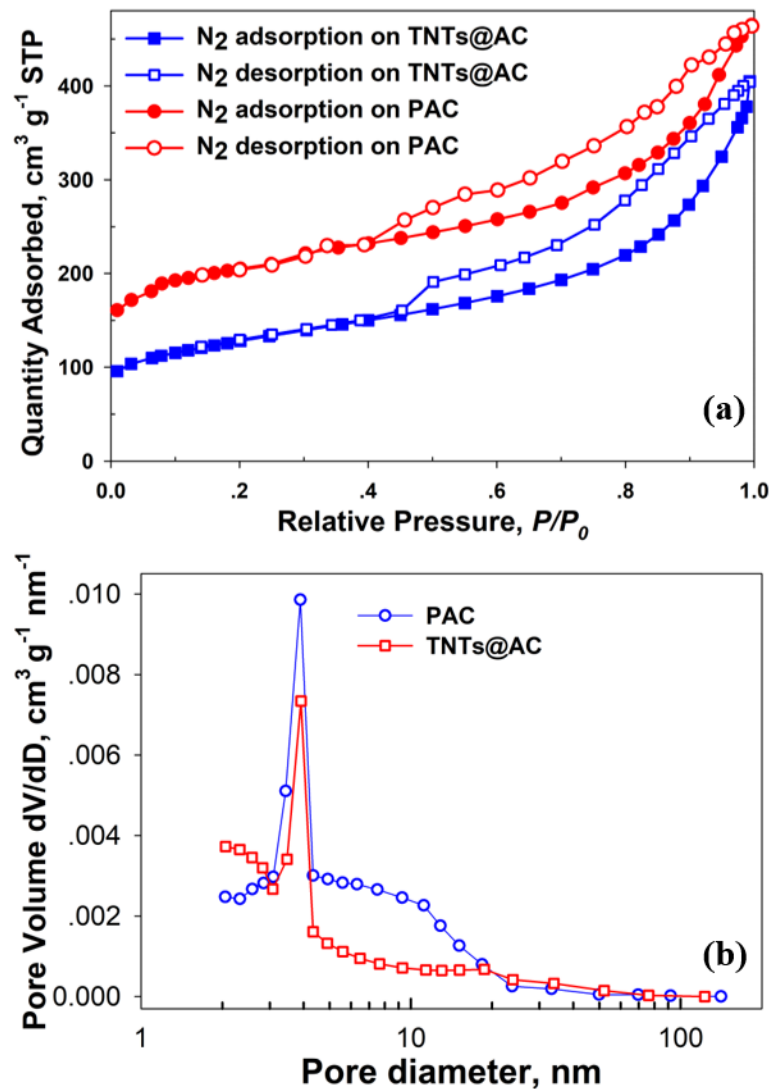
Figure 4-3. (a) N_2 adsorption-desorption isotherms and (b) pore size distributions of PAC and TNTs@AC.

4.3.2. Adsorption of 4-CP: Kinetics and Isotherm.

Figure 4-4 shows 4-CP adsorption kinetics by TNTs@AC, alkaline hydrothermally treated AC (treated AC), and parent PAC. All adsorption reached equilibrium within 4 h with > 96% 4-CP removal. TNTs@AC demonstrated fastest uptake rate among three sorbents. More than 85% of 4-CP was rapidly adsorbed by TNTs@AC in first 5 min while treated AC and parent PAC

only uptake 68% and 57% of 4-CP in first 5 min, respectively. Pseudo first-order and pseudo second-order adsorption model were applied to interpret data and model fitting results were shown in **Table 4-3**.

Concentrations of 4-CP before and after adsorption were measured in experiments, and the uptake (q_t, mg g^{-1}) of 4-CP on our composite materials and removal efficiency (R, %) were determined via:

$$q_t = \frac{(C_0 - C_t)V}{m} \tag{4-1}$$

$$R = \frac{(C_0 - C_t)}{C_0} \times 100\% \tag{4-2}$$

where q_t (mg g^{-1} or μg g^{-1}) is the uptake of 4-CP at time t (min); C_0 and C_e (mg/L or μg/L) stand for the 4-CP concentrations at $t = 0$ and equilibrium, respectively; m (g) is the mass of composite materials; and V (L) is the total volume of the solution.
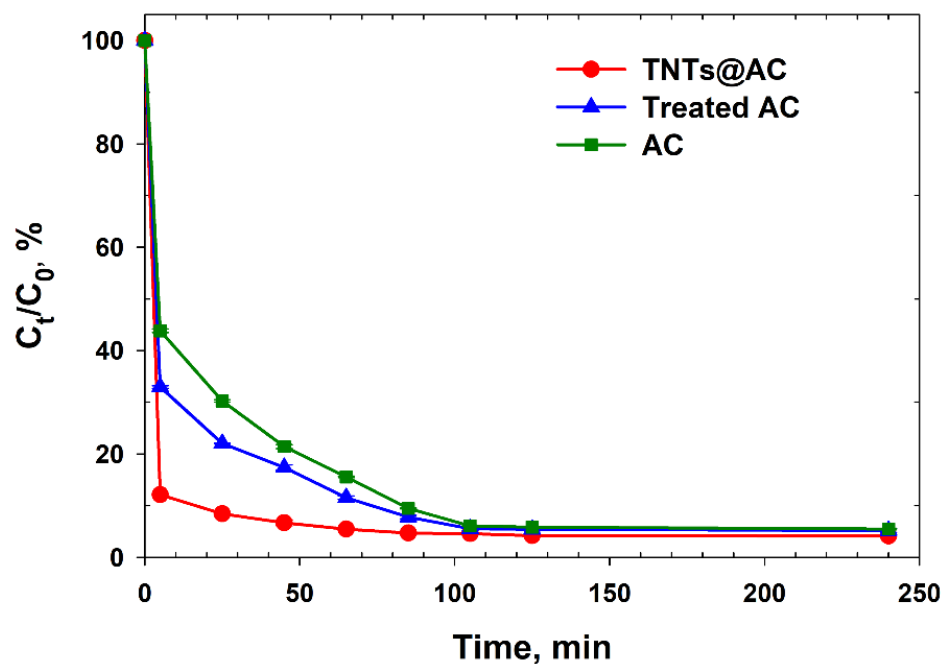
Figure 4-4. 4-CP adsorption kinetics by TNTs@AC, alkaline hydrothermally treated AC (treated AC), and PAC. Conditions: Initial [4-CP] = 8 mg/L, material dosage = 0.2 g/L, volume = 40 mL, pH = 7 ± 0.2, and reaction time = 4 h.

Table 4-3. Model fitting parameters of 4-CP adsorption kinetics

Models	Parameters	Materials		
		TNTs@AC	Treated AC	AC
pseudo first-order	k_1 (min^{-1})	1.28×10^{-1}	0.74×10^{-1}	0.63×10^{-1}
	R^2	0.924	0.956	0.938
pseudo second-order	k_2 (g (mg·min)$^{-1}$)	3.31×10^{-2}	2.06×10^{-2}	1.49×10^{-2}
	R^2	0.992	0.994	0.989

Model fitting results indicated that pseudo-second order can better describe the 4-CP adsorption kinetics by TNTs@AC, treated AC, and parent PAC whereas intraparticle diffusion no longer is the 4-CP adsorption kinetic rate limit step (Ho and McKay, 1999). The k_2 (pseudo second-order rate constant) of TNTs@AC was approximately 1.5 and 2 times faster than rate constants of treated AC and parent PAC, respectively. This observation indicates that alkaline hydrothermal treatment and TNTs modification take the important role in 4-CP adsorption. Alkaline hydrothermal treatment can release "micro-carbon" (nanoscale) from parent PAC and further accumulate on surface of PAC or intermingled with TNTs. Thus, the modification provides more accessible sites on parent PAC surface and together with TNTs induced a new adsorption manner caused by capillary condensation effect (Liu et al., 2016a). The rapid adsorption leads to efficient removal of 4-CP from bulk water with a small hydraulic residence time (HRT) (i.e., a small reactor) which could be applied as an infrastructure-free treatment.

Figure 4-5 shows the adsorption isotherm of 4-CP by TNTs@AC, alkaline hydrothermally treated AC, parent PAC and neat TNTs. Previously, we have observed that a dual-mode model can better describe TNTs@AC adsorption behavior than classic Langmuir isotherm model and

Freundlich model (Liu et al., 2016a). Dual-mode adsorption model (Eq. 1) consist of two stages:

1) Langmuir-type adsorption in low initial 4-CP concentration range which assumes that the

adsorption sites on a monolayer are equivalent and homogeneous without interaction between

adsorbate molecules on adjacent sites; 2) linear-type adsorption in high initial 4-CP

concentration range which may due to capillary condensation or partition effect.

$$Q_e = \frac{Q_L b C_e}{1 + b C_e} + K_d C_e \tag{4-3}$$

where K_d (L/g) is the distribution coefficient, Q_L (mg/g) is the Langmuir maximum

adsorption capacity, b (L/mg) is the Langmuir constant, and C_e is aqueous phase concentration at

equilibrium. Although Eq. 1 shares the same formula as the classical dual-mode model that

considers a dissolution domain and a hole-filling domain (Zhao et al., 2002, 2001), the

underlying physical meanings are different. Dual-mode model fitting parameters are shown in

Table 4-4.
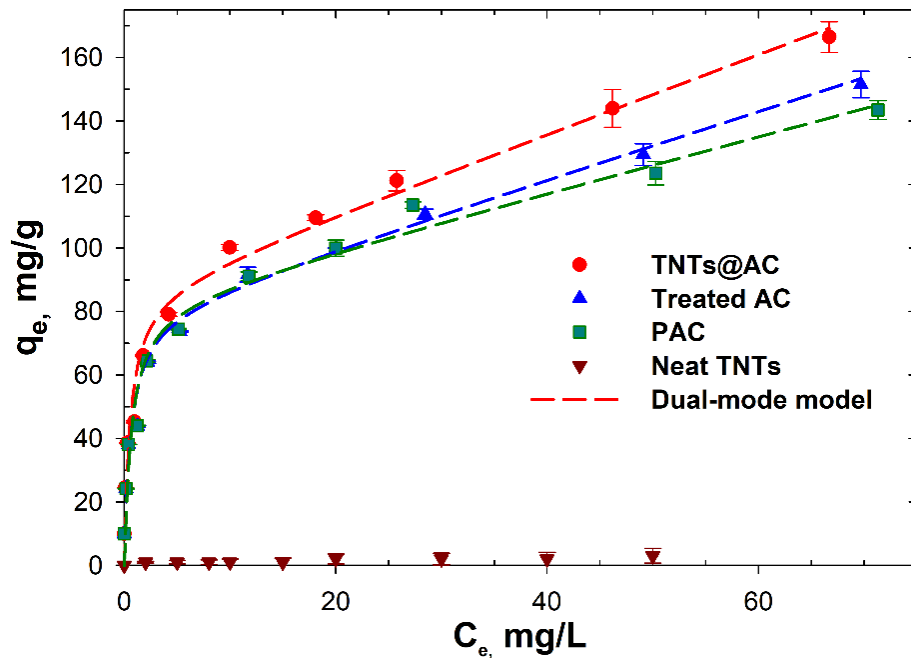
Figure 4-5. 4-CP adsorption isotherm by TNTs@AC, alkaline hydrothermally treated AC (treated AC), PAC and neat TNTs. Conditions: Initial [4-CP] = 2-100 mg/L, material dosage = 0.2 g/L, pH = 7 ± 0.2, volume = 40 mL, temperature = 25 °C, and reaction time = 24 h.

Table 4-4. Dual-mode model fitting parameters

Adsorbent	K_d (L/g)	Q_L (mg/g)	b (L/mg)	R^2
TNT@AC	1.24 ± 0.19	87.02 ± 7.26	1.89 ± 0.17	0.982
Treated AC	1.01 ± 0.14	85.69 ± 3.62	1.64 ± 0.11	0.961
PAC	0.94 ± 0.16	83.16 ± 6.36	1.54 ± 0.19	0.974

The dual-mode model fitting results show that TNTs@AC just offer slightly better (~10%) adsorption capacity than treated AC and parent PAC. But given that neat TNTs only has negligible adsorption capacity towards 4-CP (< 5 mg/g) and TNTs@AC consists approximately 37% (wt. %) (Liu et al., 2016a) of TNTs, the 4-CP adsorption capacity based on AC was greatly enhanced. This enhanced adsorption capacity may due to capillary condensation on "micro-carbon" modified TNTs. Specific, TNTs in TNTs@AC are attached on scattered nano-scale AC particle. The tubular structure of TNTs in TNTs@AC turned to be much contaminated and distorted compared to the well-defined multilayered (4-5 layers) neat TNTs since AC was co-existed during alkaline hydrothermal process. Hence, some nanoscale "micron-carbon" were patched in the interlayer of TNTs or coated on the coarse nanotubes. As consequence, the neat TNTs is morphologically open-ended while the TNTs of TNTs@AC show a narrow ink-bottle structure with more "micro-carbon" occupied on entrance of tube (Liu et al., 2016a). Although "micro-carbon" were patched on interior and exterior walls of the TNTs, forming a narrow-throat structure at the open-ends of the nanotubes and relatively large and ellipsoidal

cavity inside the nanotubes mimicking the ink-bottle pore geometry (Libby and Monson, 2004). The carbon coating reduced most of the interior tube diameters from 5-9 nm (Liu et al., 2016b) to < 4 nm (Liu et al., 2016a) and further benefit capillary condensation of 4-CP. Typically, there are four stages can be perceived in transition process of adsorption to capillary condensation (Tuller et al., 1999). In low-concentration stage, 4-CP is initially adsorbed on the pore sites and slit nanotube walls following the classical Langmuir mode. Afterwards, the adsorbed layer thickens with increased 4-CP concentration until the slits on nanotube walls are fully filled with liquid due to capillary condensation. Further increasing the matric potential fills the "belly" of the residual pore in nanotube, resulting in a reduction in the radius of curvature of liquid−vapor interfaces and forming a circle or elongated oval-shaped interface. Later, the pore is completely filled with 4-CP and capillary condensation and/or adsorption reach maximum capacity (Liu et al., 2016a).

4.3.3. pH effects, ionic strength effects, and dissolved organic matters (DOM) effects on 4-CP adsorption

Figure 4-6 shows the pH effect on 4-CP adsorption by TNTs@AC and TNTs@AC performed consistently stable in pH range of 4-11 (> 96% 4-CP removal). Additionally, ~0.06% and ~1% of Ti was dissolved into the 4-CP solution at pH 3 and 2, respectively. Yet, no soluble Ti was detected under alkaline condition (**Table 4-5**), indicating the composite material has strong stability in wide pH range (Bavykin et al., 2006; Wang et al., 2013). Likewise, 4-CP removal at pH 2decreased significantly ($p < 0.05$) compare to neutral and alkaline pH. This may due to the tubular structure of TNTs was destroyed at very acidic condition, and hence capillary

condensation no longer took place to enhance 4-CP uptake. **Figure 4-7** shows the ionic strength effects on 4-CP adsorption by TNTs@AC. With presence of NaCl and CaCl$_2$, insignificant inhibition (p >0.05) of 4-CP removal rate at 4 h was observed. As cation-exchanger, neat TNTs can uptake Na$^+$ and Ca^{2+} efficiently through ion exchange process (Wang et al., 2013). After carbon modification, TNTs@AC keeps this unique advantage, and thus TNTs@AC has resistance towards high salt concentration.
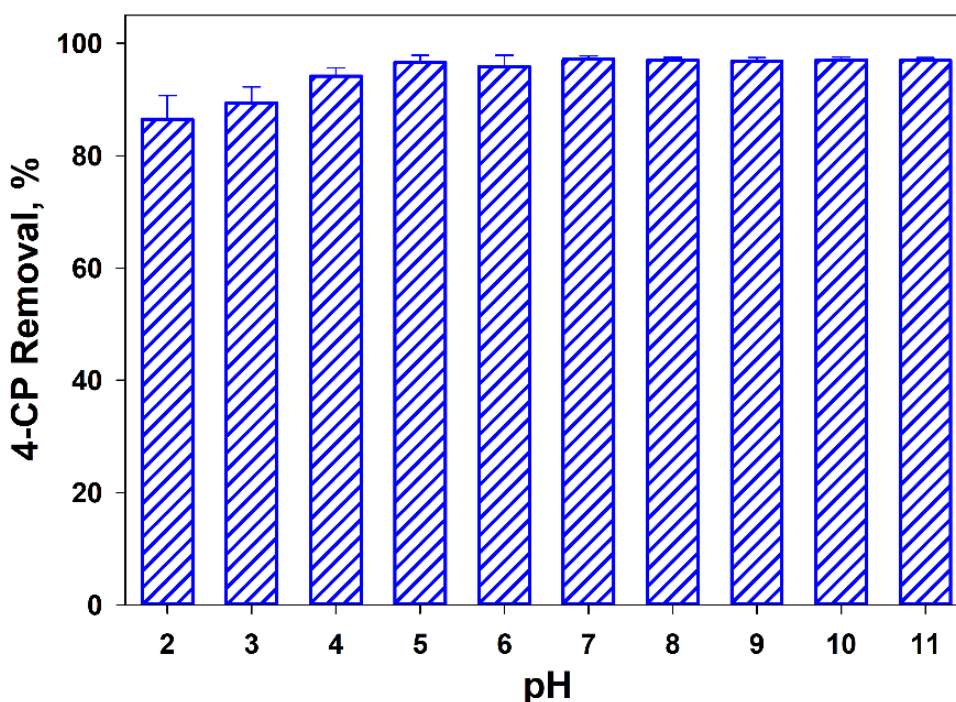
Figure 4-6. pH effect on 4-CP adsorption by TNTs@AC. Conditions: Initial [4-CP] = 8 mg/L, material dosage = 0.2 g/L, pH = 2-11, volume = 40 mL, temperature = 25 °C, and reaction time = 4 h.

Table 4-5. Dissolution of Ti from TNTs@AC at different pH.

pH	Ti dissolution, w.t.%	pH	Ti dissolution, w.t.%
2	0.942	7	N.D.
3	0.057	8	N.D.
4	0.012	9	N.D.
5	0.005	10	N.D.
6	N.D.*	11	N.D.

*N.D.: non-detectable
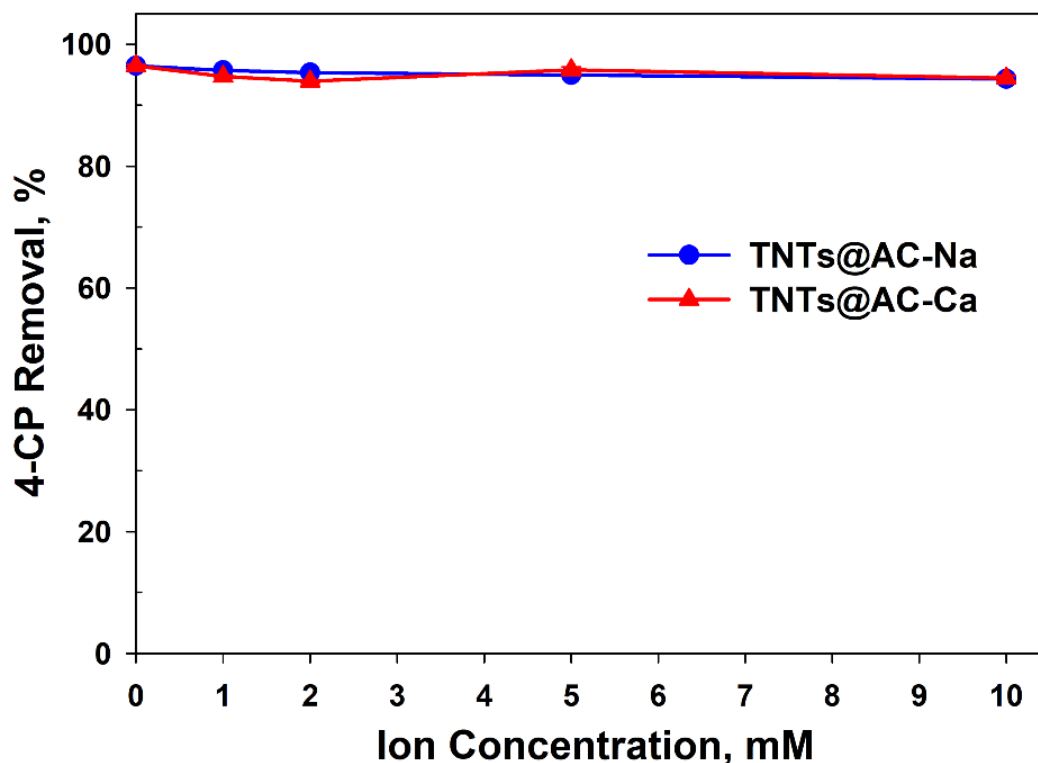
Figure 4-7. ionic strength effect on 4-CP adsorption by TNTs@AC. Conditions: Initial [4-CP] = 8 mg/L, material dosage = 0.2 g/L, pH = 7, NaCl/CaCl2 concentration = 1, 2, 5, and 10 mM, temperature = 25 °C, volume = 40 mL, and reaction time = 4 h.

HA displayed quite unique and interesting effects on TNTs@AC and parent PAC (**Figure 4-8)**. For TNTs@AC, when HA concentration was increased from 0 to 5 mg/L as TOC, 4-CP removal was slightly improved from 96.4% to 99.5%. When HA concentration was further increased from 5 to 20 mg/L as TOC, 4-CP removal was rapidly dropped to 68.2%. In contrast, the uptake of 4-CP by parent AC was progressively inhibited when HA concentration increased. The inhibitive effect on PAC adsorption was expected since DOM can cause irreversible adsorption and clogging of the pores, which is also known as organic fouling or territorial binding (Pignatello et al., 2006). Difference between TNTs@AC and parent PAC can be

attributed to that pore sites on TNTs@AC have only limited contribution of 4-CP removal and

TNTs@AC has much higher HA uptake capacity (~5 times) than parent PAC (**Figure 4-9**).

Furthermore, low concentration HA and high concentration HA will have opposite effects on 4-

CP removal. When HA concentration is relatively low (0-5 mg/L as TOC), HA (surfactant like

molecules) (Libby and Monson, 2004) may form bilayer membranes coating on the TNTs, which

will further enhance ad-solubilization of 4-CP (Liu et al., 2016a). On the other hand, smaller

absorbable components of HA partially intent to aggregate through hydrophobic interaction and

H-bonds after HA concentration was elevated (Chilom et al., 2009). Afterwards, HA aggregates

will compete for π-π bonding sites and/or hydrophobic sites, which are crucial for 4-CP

adsorption by carbon materials (Yang et al., 2010), and then further inhibit 4-CP adsorption.
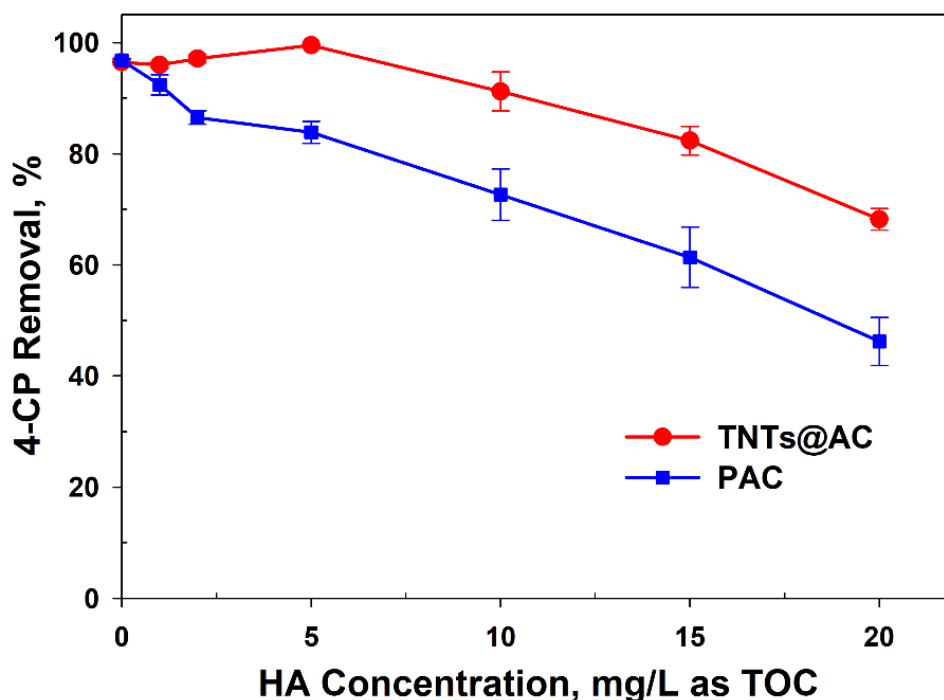
Figure 4-8. DOM effect on 4-CP adsorption by TNTs@AC and parent PAC. Conditions: Initial [4-CP] = 8 mg/L, material dosage = 0.2 g/L, pH = 7, HA concentration = 1, 2, 5, 10, 15, and 20 mg/L as TOC, volume = 40 mL, temperature = 25 °C, and reaction time = 4 h.
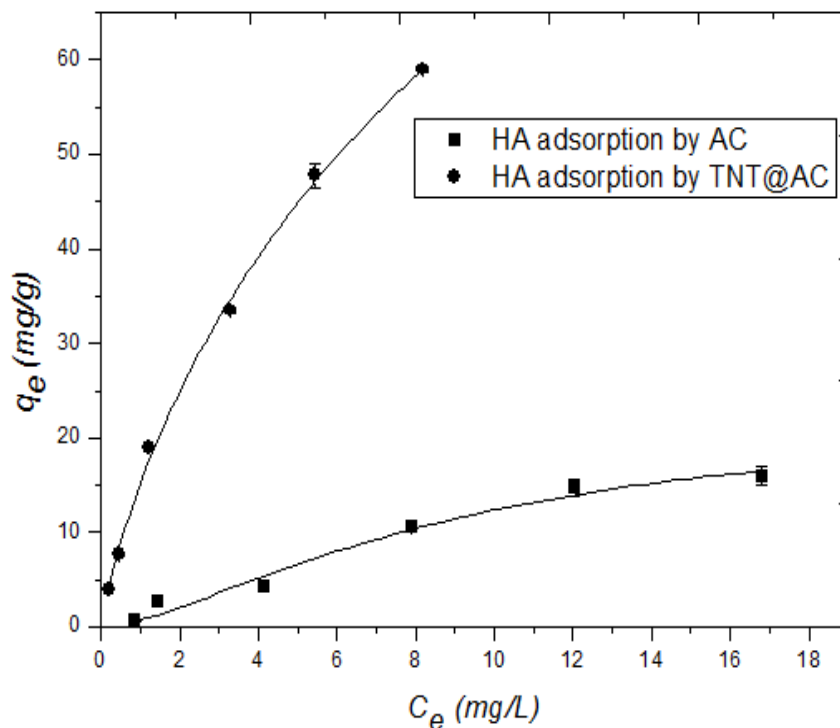
Figure 4-9. HA adsorption isotherm by TNTs@AC and parent PAC. Conditions: Initial [HA] = 1-20 mg/L as TOC, material dosage = 0.2 g/L, volume = 40 mL, pH = 7 ± 0.2, temperature = 25 °C, and reaction time = 24 h.

4.3.4. Photodegradation of 4-CP and Reuse of TNTs@AC

Figure 4-10 indicated that only limited (<7%) of 4-CP can be directly degraded by UV irradiation. As comparison, the mass of 4-CP pre-loaded on parent PAC showed ~12% reduction after hot methanol extraction. Given the 4-CP recovery rate (> 87%), PAC demonstrated negligibly catalytic effect on 4-CP degradation. In this section, various composite material dosages (0.2, 0.3, and 0.5 mg/L) were applied for 4-CP photodegradation. As shown in **Figure 4-11**, all experimental groups with different dosages uptake 4-CP rapidly in first 5 min and reached adsorption equilibrium within 2 h. The 4-CP removal of 0.2, 0.3, and 0.5 g/L were 96%, 98%,

and 99%, respectively. Thus, the total mass of 4-CP loaded on materials were approximately

same.
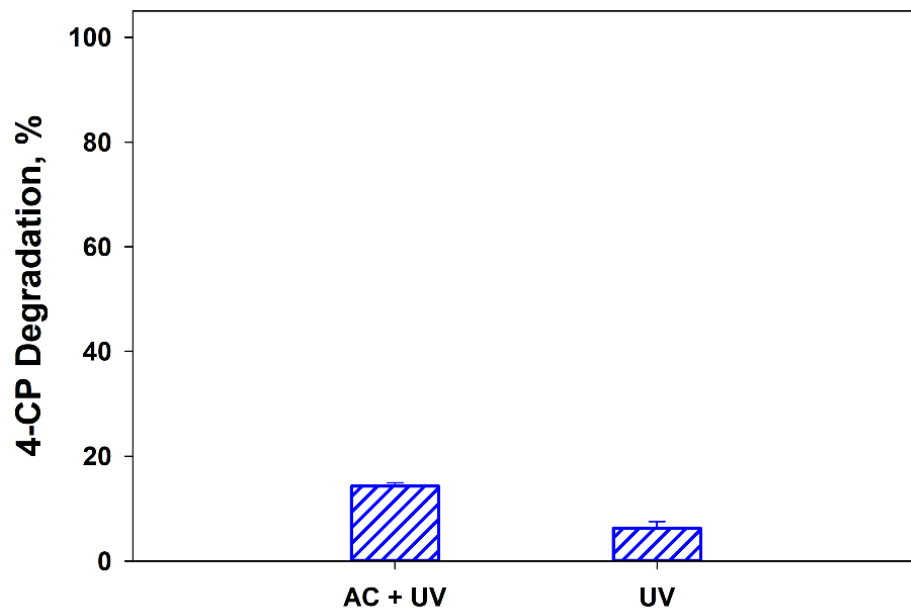
Figure 4-10. 4-CP photodegradation on AC and photolysis in DI. Conditions: Initial [4-CP]
= 8 mg/L, material dosage = 0.2 g/L, pH = 7 ± 0.2, temperature = 25 °C, volume = 40 mL, and
reaction time = 4 h.
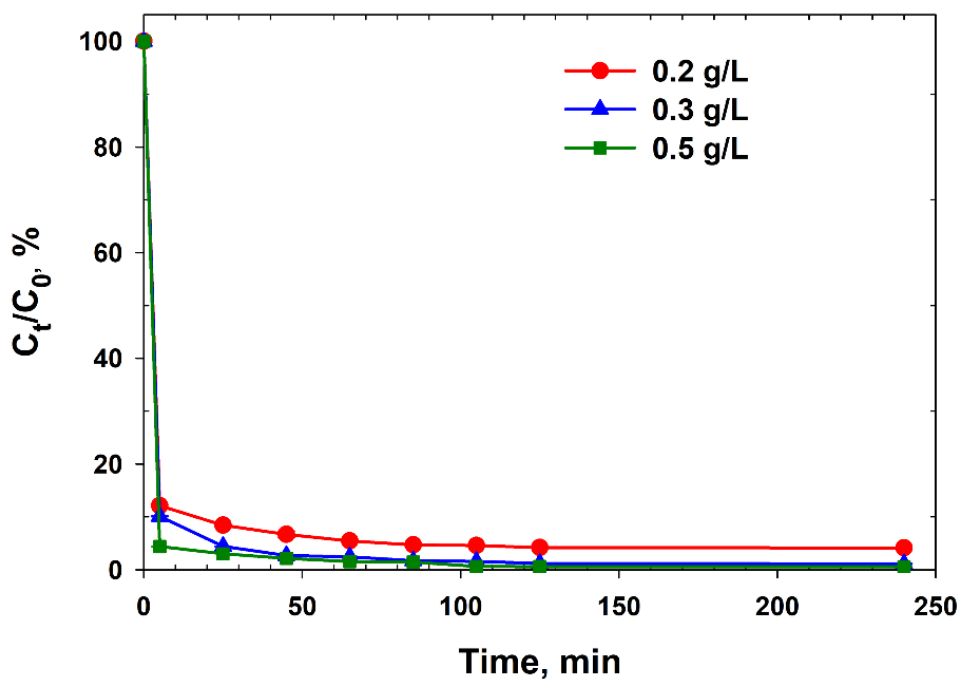
Figure 4-11. 4-CP adsorption kinetics by TNTs@AC with various dosages. Conditions: Initial [4-CP] = 8 mg/L, material dosage = 0.2, 0.3, and 0.5 g/L, volume = 40 mL, pH = 7 ± 0.2, temperature = 25 °C, and reaction time = 4 h.

In **Figure 4-12**, composite materials without UV were used to correct potential hot methanol method recovery bias which caused by dosage difference. In fact, recovery rate was very stable (all > 87%) for all dosages at different time, and therefore, reduction of 4-CP only attribute to photodegradation. **Figure 4-12** also shows the corresponding photodegradation kinetics under UV-irradiation. The pseudo first-order kinetic model (Eq. 2) and retarded first-order kinetic model (Eq. 3) were used to fit the photodegradation kinetic data, and **Table 4-6** offers the best fitted parameters.

$$\text{First-order kinetic model: } \ln\left(\frac{M_t}{M_0}\right) = -k_1 t \tag{4-3}$$

$$\text{Retarded first-order kinetic model: } \frac{M_0}{M_t} = \frac{1}{(1+\alpha t)^{-k_{init}/\alpha}} \tag{4-4}$$

where M_0 and M_t are the 4-CP mass (mg) at time 0 and t (h), respectively, k1 is the first-order rate constant (1/h), and ka is the retarded first-order rate constant (1/h).
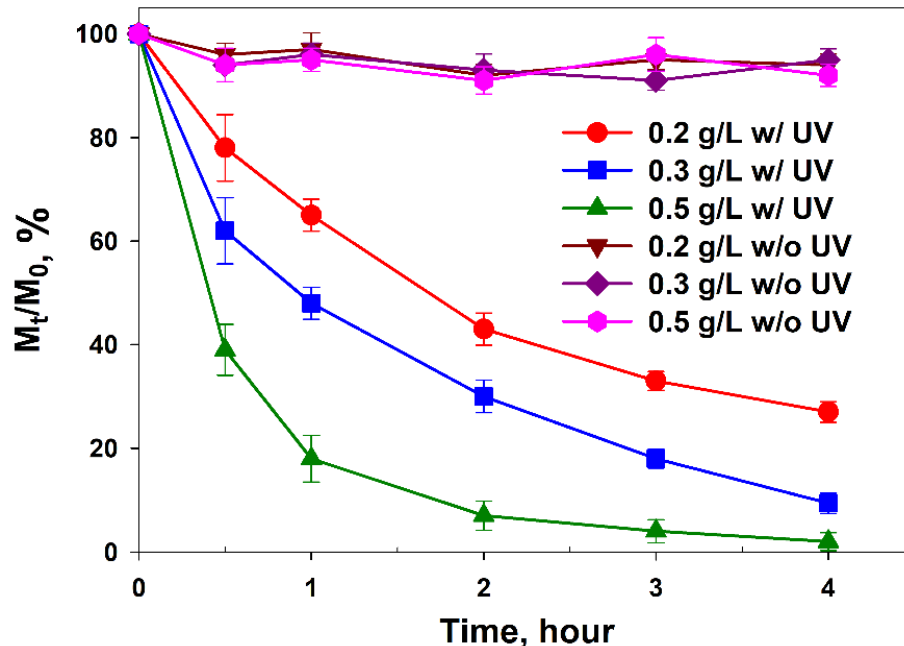
Figure 4-12. 4-CP photodegradation kinetics by TNTs@AC with various dosages. Conditions: Initial [4-CP] = 8 mg/L (before adsorption), material dosage = 0.2, 0.3, and 0.5 g/L, pH = 7 ± 0.2, temperature = 25 °C, and UV-irradiation reaction time = 4 h.

Table 4-6. Kinetic model parameters for photodegradation of 4-CP by TNTs@AC at various material dosages.

Models	Parameters	Materials		
		0.2 g/L	**0.3 g/L**	**0.5 g/L**
First-order kinetic model	k_1 (1/h)	0.345	0.596	0.854
	R^2	0.954	0.971	0.825
Retarded first-order kinetic model	k_a (1/h)	0.059	0.106	0.184
	α (1/h)	0.014	0.021	0.031
	R^2	0.999	0.999	0.999

It is interesting that both kinetic models fit well to the data for 0.2 and 0.3 g/L dosages, while the retarded first-order model fits much better than the first-order model for 0.5 g/L (R^2: 0.999 vs. 0.825). Upon photolysis, about 72%, 91% and 97% of 4-CP were degraded by 0.2, 0.3, and 0.5 g/L of TNTS@AC, respectively. It is evident that the higher material dosage allowed 4-CP to be accumulated at the sites that are more accessible for both adsorption and

photodegradation (e.g., micro-carbon attached on the surface of TNTs). At the dosage of 0.5 g/L, more than 80% of 4-CP was degraded in the first hour; yet only 14% more was degraded in the subsequent three hours; and after 4 h of UV irradiation, there remained 3% of 4-CP in the material. This phenomenon indicates that 4-CP is distributed at different classes of the reactive sites, and a small residual of 4-CP may be hardly photodegradable.

Previously, we observed that AC modification of TNTs resulted a blue shift on absorption edge compare to neat TNTs, with an increased band energy gap (Liu et al., 2016a). Briefly, broadened band energy gap indicates the band structure of the composite materials turns to be quantized, which prefer the utilization of UV light and suggested that, at least, part of the " micro-carbon" are quantum dots (Slimen et al., 2011; Takagahara and Takeda, 1992). The quantization have a tendency to confine photo-excited electrons in the conduction band (CB), and further enhancing the photocatalytic activity of composite material (Slimen et al., 2011; Takagahara and Takeda, 1992) and generation of reactive oxygen species (ROS), especially hydroxyl radicals ($\cdot$OH), which play a dominant role in 4-CP degradation (Li et al., 2018).

Next, **Figure 4-13** shows that when TNTs@AC with dosage of 0.2 or 0.5 g/L were repeatedly used in five consecutive cycles of adsorption-photodegradation without chemical regeneration, namely, the efficient photodegradation of pre-concentrated 4-CP also regenerates the material. It is interesting that 4-CP adsorption by 0.5 g/L of TNTs@AC remained high (>99% removal) while 4-CP adsorption by 0.2 g/L of TNTs@AC keep decreasing. As mentioned above, 4-CP intents to occupy some un-regenerable reactive site (i.e. sites in deep pores) if material dosage is not high enough. In contrast, easy-access sites on surface of composite can

perfectly keep adsorb 4-CP and degraded it later. Evidently, TNTs@AC can be reused in

multiple cycles without additional regeneration need if dosage is high enough.
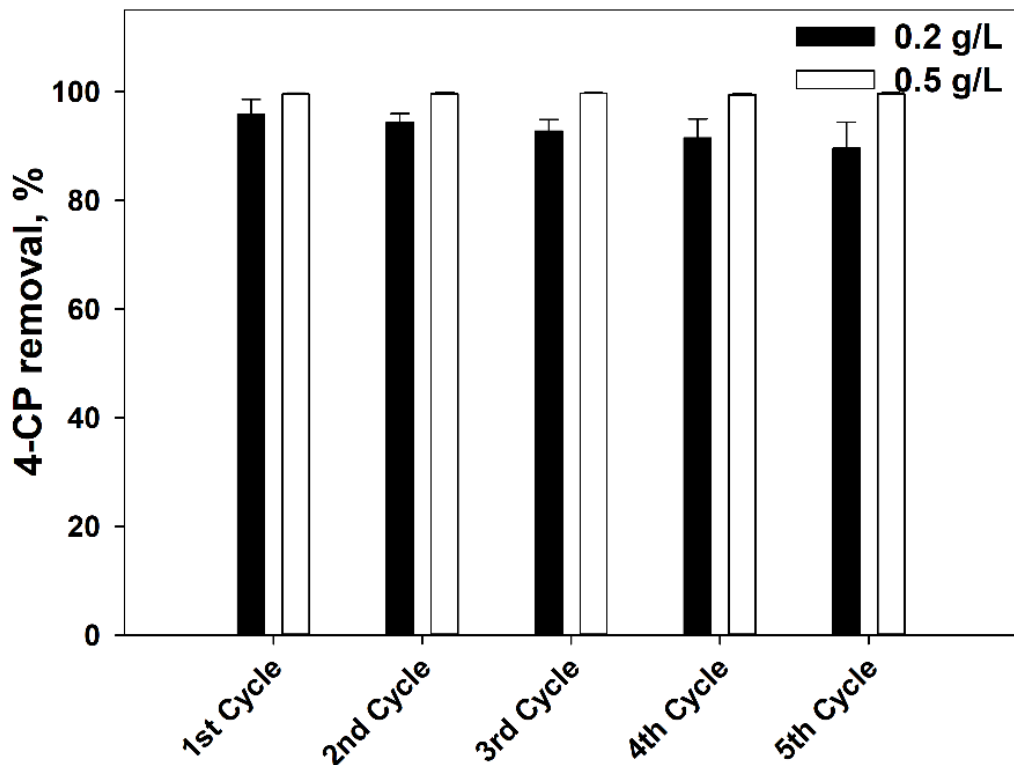
Figure 4-13. Reuse test of TNTs@AC. Conditions: Initial [4-CP] = 8 mg/L (each cycle), material dosage = 0.2 and 0.5 g/L, pH = 7 ± 0.2, temperature = 25 °C, adsorption reaction time = 4 h and UV-irradiation reaction time = 4 h.

4.4. Conclusions

An adsorptive photocatalyst, PAC modified titanate nanotubes, was synthesized through a

one-step facile hydrothermal treatment. This material showed excellent adsorption capacity and

rapid uptake rate of 4-CP. Meanwhile, TNTs@AC also displayed great photocatalytic activity

for 4-CP degradation under UV light. The "concentrate-&-destroy" approach allows TNTs@AC

uptake target trace level POP rapidly from large volume water body, and afterward TNTs@AC

91

can be separate by gravity easily. This fast and convenient pre-concentrate process will further

allow people to regenerate the composite materials in a small and movable reactor. In other

words, the entire treatment will be an infrastructure-free process, which can greatly lower cost

and shorten construction period. Additionally, resistance of DOM and adaption of wide pH range

and high salinity make TNTs@AC a promising composite material which can be utilized to

remove trace level POP from domestic sewage water, groundwater, industrial wastewater, and

even landfill leachate.

Chapter 5: Rapid adsorption and photodegradation of perfluorooctanoic acid (PFOA)

by a new iron/titanate nanotubes modified activated carbon composite at neutral pH

Fe/TNTs@AC was prepared by doping iron on TNTs@AC to apply the "Concentrate-&-Destroy" concept to rapid removal of PFOA in water. The adsorbed iron and AC work synergistically in adsorption of PFOA through concurrent hydrophobic interactions and metal-ligand complexation. Moreover, Fe and AC particles facilitate the molecular orientation of PFOA and electron-transfer, thereby enhancing photocatalytic activity of the composite material. Furthermore, the presence of Fe can take up photo-generated electrons (e^-), and thus inhibit the e^--h^+ recombination. . DFT calculations and analysis of intermediate products confirmed that decarboxylation of PFOA was the key mechanism in PFOA degradation.   Fe/TNTs@AC is also amenable to repeated uses without chemical regeneration. After 6 times of repeated adsorption and photodegradation cycles, Fe/TNTs@AC showed no significant drop in adsorption and photocatalytic activity for PFOA.

5.1. Introduction

Per- and polyfluoroalkyl substances (PFAS) have become a class of important contaminants in soil and water due to their wide-spread applications, resistance to environmental degradation, and potential health effects (Li et al., 2019). Perfluorooctanoic acid (PFOA) and perfluorooctane sulfonate (PFOS) are the most detected PFAS (Li et al., 2019). To mitigate human exposure, EPA established a lifetime health advisory level of 70 ng /L for combined PFOA and PFOS in drinking water on May 19, 2016. A recent survey reported that drinking water supplies for 6 million U.S. residents exceeded the advisory level (Hu et al., 2016).

Human exposure to PFAS has been linked to cancer, elevated cholesterol, obesity, immune suppression, and endocrine disruption (Hu et al., 2016). Health concerns in the early 2000s prompted manufacturers in Europe and North America to phase out production of some long-chain PFAS (Land et al., 2018).

To address the PFAS associated issues, conventional technologies including physical adsorption/filtration and redox decomposition have been developed for *in-* or *ex-situ* treatments. Commonly used sorbents for PFOA removal cover a broad range of composite materials, such as activated carbon (Dudley, 2012; Zhao et al., 2011), carbon nanotubes (Deng et al., 2012), carbon fibers (Wang et al., 2015), metal organic frameworks (Liu et al., 2015), and ion-exchange resins (Deng et al., 2010). However, this approach only transfers PFAS from aqueous phase to solid phase, and inevitably generate regeneration wastes that require high-cost management or disposal. On the other hand, redox decomposition, including photochemical, sonochemical (Lin et al., 2016), electrochemical (Yang et al., 2015) and thermochemical treatments (Krusic et al., 2005) could partially or even completely mineralize PFAS, yet concerns of high energy-demand and operational cost still hinder their engineering applications. Recently, photocatalytic decomposition was recognized as a promising technique for PFAS removal since it can offer more efficient defluorination, easier operation conditions, reduction of acute toxicity, and lower energy consumption (Cho, 2011, p. 2). Under light irradiation, free electrons (e^-) are excited and transfer from the valence band (VB) to the conduction band (CB) on the catalyst surface, yielding highly reactive electron holes (h^+) (Legrini et al., 1993). Secondary products of photocatalytic excitation include hydroxyl radicals ($^\bullet OH$), superoxide radicals ($^\bullet O^{2-}$), and organic

94

substrates radicals (Legrini et al., 1993). These reactive species are reported to be responsible for the PFAS degradation.

Still, the photocatalytic process needs to be improved in several aspects. In general, $^\bullet$OH prefer to abstract the H atom from organic compounds' C–H bonds (Liu et al., 2016b) that most PFAS obviously do not have. Further, the oxidation potential of $^\bullet$OH ($E^0 = 2.72V$) (Schwarz and Dodson, 1984) and $^\bullet O^{2-}$ ($E^0 = 1.83V$) (Radi et al., 1991) were lower than the redox potential of fluorine ($E^0 = 3.06V$) (Beltran, 2003). Therefore, it is thermodynamically unfavorable to oxidize C–F bond (bond energy approximately $107 - 118$ kcal mol^{-1}) (Bentel et al., 2019) in nature by $^\bullet$OH or $^\bullet O^{2-}$ alone. Although it is believed photogenerated electron/hole acted as the major reactive species in PFAS photodegradation (Bahnemann et al., 1997; Estrellan et al., 2010), they are easily scavenged or self-combined preventing the direct reduction/oxidation of PFAS. Heterogeneous photocatalysts modified with transition metals (Chen et al., 2015), noble metals (Li et al., 2016), carbon nanotube (Song et al., 2012), and graphene/graphene oxide(Li et al., 2012) could trap the photogenerated electrons, thereby avoiding the electron-hole recombination for enhanced photocatalytic activity.

Further, the photocatalysts are unlikely to be directly applied in wastewater treatment plants (WWTPs), due to the following factors: 1) light can only travel a short distance in water or sludge systems; 2) recycle of these photocatalysts for reuse would be difficult from the large volume of daily treated water; 3) mass transfer could be a rate-limiting step without mixing that usually is energy-intensive; and 4) acidic pH condition is favored in most photocatalytic processes (Dillert et al., 2007; Sahu et al., 2018), which is not operationally practical in WWTP.

Thus, in our previous works, we developed a new class of adsorptive photocatalyst for application of photodegradation technology in WWTP for the first time (Liu et al., 2016a; Ma et al., 2017). Specifically, we synthesized activated carbon modified titanate nanotubes (TNTs@AC) through a one-step hydrothermal treatment method base on low-cost AC and TiO_2. TNTs@AC not only offers rapid adsorption rate and enhanced adsorption capacity, but also boosts AC-mediated electron transfer and reactive oxygen species (ROS) production (Liu et al., 2016a). Following photodegradation, the composite materials were thus regenerated for reuse. This "concentrate-and-degradation" strategy promoted light absorption efficiency and mass transfer in a relatively small treatment volume. Meanwhile, TNTs@AC demonstrate outstanding photocatalytic activity over a broad pH range, exhibiting great capability for trace contaminants removal in WWTPs.

The "concentrate-and-degradation" approach would also be a feasible method for PFOA degradation. We hypothesized that introducing transition metals (*e.g.*, Fe) into TNTs@AC would prevent the electron-hole recombination and thus facilitate the direct reactions between electrons/holes and PFOA molecules to achieve higher photo-decomposition ability. Specifically, the doped Fe, an excellent conductor, could act as electron sink and thus prevent electron-hole recombination; second, Fe in oxide form could shift the PZC values to alkaline pH range for enhanced adsorption of anionic PFOA at neutral pH; and third, the concentrated PFOA by adsorption could be degraded by free electrons/electron holes at elevated levels. The material modification, along with mechanistic investigation, in this study could provide a cost-effective solution to remove PFAS in wastewater or groundwater.

5.2. Materials and methods

5.2.1. Chemicals and materials

All chemicals used in this study were of analytical grade or higher. Nano-TiO_2 (P25, 80% anatase and 20% rutile) was acquired from Evonik (Worms, Germany). NaOH (Granular), absolute ethanol, and HCl were obtained from Acros Organics (Fair Lawn, NJ, USA).   A DARCO granular activated charcoal (20–40 mesh) was purchased from Sigma-Aldrich (St. Louis, MO, USA) and used as received. Filtrosorb-400® granular activated carbon (F-400 GAC) was donated by Calgon Carbon Corporation (Pittsburgh, PA, USA) and used as received. F-400 GAC was made of bituminous coal to achieve high density and high surface area for organic pollutant removal. PFOA (physicochemical properties shown in **Table 5-1**) was obtained from Sigma-Aldrich (St. Louis, MO, USA), and a stock solution of 10 mg/L was prepared and stored at 4 °C. Perfluoro-n-[1,2,3,4,5,6,7,8-13C8]octanoic acid (13C-PFOA or M8PFOA) was purchased from Wellington Laboratories Inc. (Guelph, Ontario, Canada Perfluoro) and was used as isotopically labeled internal standards (IS). All solutions were prepared using deionized (DI) water (18.2 MΩ cm, Millipore Co., USA).

Table 5-1. Physicochemical properties of PFOA.

parameters	values [a]
chemical formula	$C_8HF_{15}O_2$
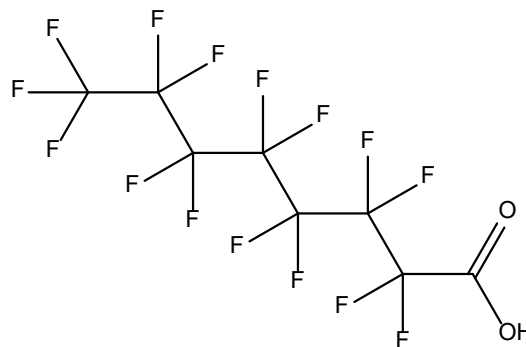
chemical structure	
molecule weight	414.07 g mol^{-1}
boiling point	192 °C
Log Kow	4.81
solubility in water	3300 mg/L (25 °C)
CAS Number	335-93-3

[a] https://pubchem.ncbi.nlm.nih.gov/compound/9554#section=Other-Identifiers

5.2.2. Synthesis and characterization of Fe/TNTs@AC

Fe/TNTs@AC composite was initially synthesized through a hydrothermal method modified based on our previous studies (Liu et al., 2016a). Typically, 1.2 g of TiO$_2$ was mixed with 1.2 g of F-400 GAC and then dispersed into 67 mL of a 10 M NaOH solution. After stirring for 12 h, the mixture was transferred into a Teflon reactor and heated at 130 °C for 72 h. Then, the gray precipitates, i.e., TNTs@AC, were washed with deionized (DI) water until neutral pH, and then oven-dried at 105 °C for 4 h. Then, 1 g of dried TNTs@AC was dispersed in 100 mL of DI water, and then 10 mL of an FeCl2 solution (1 g /L as Fe, pH = 3.0) was drop-wise added into the TNTs@AC suspension (Fe:TNTs@AC = 1 wt.%). Upon equilibrium, nearly all (>99.7%) Fe(II) ions were adsorbed by TNTs@AC, the solid particles were separated via centrifugation,

and then oven-dried at 105 °C for 24 h, which also oxidized Fe(II) to Fe(III). The supernatant was analyzed for residual dissolved iron. Then, the dried particles were calcined at 550 °C and under a nitrogen flow at 100 mL min^{-1} for 3 h. No detectable Ti or Fe leaching was observed when 0.2 g of Fe/TNTs@AC was mixed with 200 mL DI water.

Additionally, the calcination temperature and Fe content were varied to obtain best photoactive Fe/TNTs@AC (good adsorption rate and capacity and high photoactivity). The calcination temperatures were 300 °C, 550 °C, 650 °C, and 850 °C, and the Fe contents included 0.5 wt.%, 1 wt.%, 3 wt.%, and 5 wt.%. Based on the subsequent adsorption and photodegradation tests, Fe/TNTs@AC prepared at 550 °C calcination temperature and 1 wt.% of Fe was chosen as the best composite for further studies. For comparison, TNTs@AC without Fe was also prepared following the same procedure.

Fe/TNTs@AC was characterized with respects to various physicochemical and photochemical properties. The surface morphology was imaged using a scanning electron microscope (SEM) (20 kV; FEI XL30F, Philips, USA), equipped with an energy-dispersive X-ray spectroscopy (EDS). Additionally, transmission electron microscopy (TEM) analysis was conducted on a Tecnai30 FEG microscopy (FEI, USA) operated at 300 kV. The zeta potential (ζ) was measured using a Malvern Zetasizer Nano-ZS90 (Malvern Instrument, Worcestershire, UK). The crystalline structures were analyzed on a Bruker D2 PHASER X-ray diffractometer (XRD, Bruker AXS, Germany) using Cu Kα radiation (λ = 1.5418 Å) and at a scanning rate (2θ) of 2° min^{-1}. The surface chemical compositions and oxidation states were analyzed using an AXIS-Ultra X-ray photoelectron spectroscopy (XPS) (Kratos, England), which was operated at 15 kV

and 15 mA (Al Kα X-ray). The standard C 1s peak (Binding energy, Eb = 284.80 eV) was used

to calibrate all the peaks and eliminate the static charge effects. The Brunauer–Emmett–Teller

(BET) surface area was obtained using an ASAP 2010 BET surface area analyzer

(Micromeritics, USA) in the relative pressure (P/P0) range of 0.06–0.20. The pore size

distribution was determined following the Barret-Joyner-Halender (BJH) method. The nitrogen

adsorption at the relative pressure of 0.99 was used to determine the pore volumes and the

average pore diameters. Diffuse reflectance UV-visible absorption spectra (UV-DRS) were

carried out using a UV-2400 spectrophotometer (Shimadzu, Japan). $BaSO_4$ powder was selected

as the reference at all energies to achieve 100% reflectance. To evaluate generation of hydroxyl

radicals (•OH), photoluminescence (PL) spectra were obtained using a fluorescence

spectrophotometer (SpectraMax M2, Molecular Devices, CA, USA). Be specific, terephthalic

acid can rapidly react with •OH under alkline condition to form 2-hydroxyterephthalic acid

which can be easily detected (excitation wavelength: 315 nm; emission wavelength: 360 to 490

nm).

5.2.3. Adsorption kinetic and isotherm experiments

Adsorption kinetic tests were performed in batch reactors using 40 mL high-density

polyethylene (HDPE) vials under the following experimental conditions: initial PFOA = 100

µg/L, material dosage = 1 g/L, pH = 7.0, and temperature = 22 ± 1 °C. The adsorption was

initiated by mixing a specific material with a PFOA solution. The vials were kept in the dark and

under shaking at 100 rpm. At predetermined time intervals, the vials were sampled in duplicate

and centrifuged for 2 min at 4000 rpm, and the supernatants were analyzed for remaining PFOA.

Each kinetic test lasted for 4 h, which was sufficient to reach equilibrium.

Adsorption isotherms for PFOA were conducted following the same procedure under the

following conditions: initial PFOA = 0 µg/L to 100 mg/L, material dosage = 1 g/L, pH = 7.0,

solution volume = 40 mL, and equilibrium time = 24 h.

5.2.4. Photodegradation of PFOA

Following the adsorption equilibrium, the mixtures were left still for 1 h to allow the

composite materials to settle by gravity (>99% of the materials settled). Then, ~95% of the

supernatant was pipetted out, and the residual solid-liquid mixture was transferred into a quartz

photo-reactor with a quartz cover. Then, 8 mL of DI water was added to the mixture so that the

solution volume in the photo-reactor reached 10 mL (i.e., soli:solution = 1:10), and the solution

pH was adjusted to 7.0. The reactor was then placed in a Rayonet chamber UV-reactor (Southern

New England Ultraviolet CO., Branford, CT, USA), and subjected to UV light at a wavelength

of 254 nm and an intensively of 2.28 mW cm^{-2}. After predetermined times (i.e., 1, 2, 3 and 4 h),

the liquid was collected for fluoride analysis while the solid was extracted for remaining PFOA

using 40 mL of methanol at 80 °C for 4 h. M8PFOA was used as internal standards (IS) to

correct the mass recovery and the average method recovery was >90% for PFOA. All tests were

carried out in duplicate. Degradation of PFOA refers to decomposition or breakdown of PFOA

into other compounds, e.g., shorter-chain perfluorinated carboxylic acids (PFCAs), CO_2, and F^-;

whereas defluorination or mineralization indicates conversion of fluorine in PFOA into fluoride

ions. The degradation was quantified by comparing the initial PFOA loaded on a photocatalyst

and PFOA remaining upon light irradiation, whereas defluorination was determined by measuring the fluoride produced upon the photocatalytic reactions.

Meanwhile, the pH effects on PFOA photodegradation were also studied in the pH range from 4.0 to 10.0. The classical scavenger tests with potassium iodide (KI), isopropanol (IP) and benzoquinone (BQ) was carried out to study the roles of h^+, $^\bullet OH$, and $^\bullet O^{2-}$, respectively (Wei et al., 2017b). In addition, the reusability of the photo-regenerated materials was verified by testing the material for 5 consecutive cycles of the adsorption-photodegradation experiments.

5.2.5. Chemical analysis

Quantitative analysis of trace levels of PFOA was performed on liquid chromatograph with triple quadrupole tandem mass spectrometry (LC-MS/MS). Detailed PFOA analysis method and related quality assurance/quality control (QA/QC) were described below in **section 5.2.6**. Based on our calibration analysis, the detection limits of PFOA can reach the ppt levels.The PFOA degradation intermidiates were analyzed using an ultra-performance liquid chromatography system coupled with a quadrupole time-of-flight mass spectrometer (UPLC-QTOF/MS) with electrospray ionization (ESI) operated in the negative mode. The detailed analysis method was described in **section 5.2.7**.

The fluoride in the aqueous phase was analyzed using an ion chromatography (IC) system (Dionex, CA, USA) with an IonPac AS22 IC column. The injection loop was 100 μL. The flow rate of eluent is set at 1.2 mL min^{-1} and there is a well-defined retention time for fluoride around 3.30 min. Dissolved Fe and Ti concentration in the supernatant during synthesis and after

reaction were measured on an inductively coupled plasma-optical emission spectroscopy (ICP-OES, 710-ES, Varian, USA).

5.2.6. PFOA analysis method using LC-MS/MS and related QA/QC

The PFOA analytical procedure followed the requirements specified in Table B-15: Per- and Polyfluoroalkyl Substances (PFAS) Using Liquid Chromatography Tandem Mass Spectrometry (LC/MS/MS) With Isotope Dilution or Internal Standard Quantification in Matrices Other Than Drinking Water (DoD quality system manual (QSM), version 5.3, 2019). Briefly, PFOA, and its mass labelled IS are measured with an UltiMate 3000 LC connected to a Thermo TSQ Quantum Access Max triple quadrupole MS/MS (Thermo; Waltham, MA). Samples (50 µL) are injected into a Waters XBridge BEH C18 column (2.1×150 mm, 2.5 µm) with a guard column (2.1×5 mm, 2.5 µm) containing the same material. The analytes are separated using a 6-minute isocratic elution scheme employing 65% methanol with 0.1% ammonium hydroxide and 35% water with 0.1% ammonium hydroxide (pH 10.5). The column temperature is set at 40 °C, and the eluent flow rate is 200 µL/min. The negative electrospray ionization mode is employed for all compounds and at least one product ion is selected for quantitation. A DI water sample and another sample with known PFAS concentration (both spiked with isotopes IS) will be analyzed along with other samples for each batch as QC check and to correct bias caused by shipment. After samples are delivered, the PFOA concentration in DI water sample must be lower than 1/2 limit of quantitation (LOQ) and concentration of the sample with known PFOA concentration must be within ± 10% of its true value. Failure in these criteria will lead to sample re-preparation. Other related QC were listed below:

Instrument Sensitivity Check (ISC). Prior to analysis, the instrument sensitivity must be checked at least once every 12 hours. Analyte concentration must be at the limit of quantitation (LOQ) and within ±30% of the true value.

Method Blank (MB). The method blank must be run in each preparatory batch. No analytes shall be detected more than 1/2 of the LOQ or ≥1/10 the amount measured in any sample or 1/10 the regulatory limit, whichever is greater. The MB and all samples should be re-extracted and re-analyzed for failed analytes.

Instrument Blank (IB). The instrument blanks containing Extracted Internal Standard (EIS) must be checked prior to daily sample/standards and after the highest calibration standard. The concentration of each analyte in the instrument blank must be lower than 1/2 of the LOQ. If acceptance criteria are not met in first instrument blank or after the highest calibration standard, calibration must be performed using a lower concentration for the highest standard until the acceptance criteria are met. No samples should be analyzed until instrument blanks meet the acceptance criteria.

Mass Calibration. Mass calibration is required prior to initial calibration and sample analysis. The calibration compounds are used to calibrate the mass scale of the MS, which must be within ±0.5 amu of the true value in a full scan. The entire range needs to be mass calibrated and 15 spectra scans are acquired across each chromatographic peak.

Calibration Verification. PFOA standards containing both branched and linear isomers must be used if both are commercially available. If not available, use linear isomer for quantification. Prior to sample analysis, analysis of a second source standard is needed for the

initial calibration verification (ICV), with analyte concentrations within ±30% of their true value and R^2>0.99 (minimum of 5 standards for linear calibration and minimum of 6 standards for quadratic calibration). The S/N ratio shall be >10:1 for all ions used for quantification, while the S/N ratio must be >3:1 for the quantitative transition ions.

Continuing calibration check (CCC). CCC Standards are analyzed at the beginning of each analysis batch, after every 10 field samples, and at the end of the analysis batch. Recovery for each analyte must be within 70-130% of the true value for all but the lowest level of calibration. Recovery for each analyte in the lowest CAL level CCC must be within 70-130% of the true value.

Sample PFAS Identification. Two ion transitions (Precursor → quant ion and precursor → confirmation ion) and the ion transitions ratio must be documented for the chemical derivation of the ion transition. For PFOA, the transition of 413 → 369 shall be observed.

Retention Time Establishment. Retention time of analyte must fall within 0.4 minutes of the predicted retention times from the daily calibration verification.

Internal standards (IS). The analyst should monitor the peak areas of the IS(s) in all injections during each analysis day. The IS responses (peak areas) should be within 70-130% of the response in the most recent CCC and must not deviate by more than 30% from the average area measured during initial analyte calibration. The IS PDS and an appropriate amount of 96:4% (vol/vol) methanol:water solution was added to the extract to bring the volume to 1 mL (e.g., 10 µL of the 100-400 ng/mL IS PDS for extract concentrations of 1-4 ng/mL). Then, a

small aliquot is transferred to a polypropylene autosampler vial with a plastic pipette for analysis.

5.2.7. LC-QTOF-MS operation method

LC-QTOF-MS was operated with Masslynx software (V4.1) (ACQUITY, Waters Corp., USA). The following method will be adopted based on our preliminary work. First, 10 µL of a standard or sample is injected in the C18 column (Luna C18(2), 3 µm, 100 Å, 2 × 50 mm with 2 x 4 mm guard cartridge, Phenomenex) with a 200 µL/min flow rate of mobile phase of solution A (2 mM ammonium acetate in water pH 4.7) and solution B (100% acetonitrile) beginning at 30% B for the first 0.3 minute then increasing to 95% B at 3.4 min, held at 95% B for 0.7 min, back to 30% B in 1.2 min, and re-equilibration, resulting in a total run time of 7 min. The capillary voltage is set at 2.0 kV, the sample cone voltage is 20 V, and the extraction cone is 4.5 V. The source and desolvation temperatures are maintained at 120 and 400 °C, respectively, with the desolvation gas flow at 800 L/h. The Time of Flight Mass Spectrometry scan is 1 s from 50 to 600 m/z with a 0.1 s inter-scan delay using the centroid data format. The lock mass is used to correct instrument accuracy with a 0.2 ppm solution of Leucine enkephalin. Ion source parameters such as the source temperature (gas and sample cone), mobile phase flow rate, and cone voltage will be fixed throughout the study.

5.2.8. Density functional theory calculations

To describe the surface complexation of PFOA anions at the Fe/TNTs@AC surface, density functional theory (DFT) calculations were performed using Gaussian 09. According to Wei et al. (2017) (Wei et al., 2017a), B3LYP functional, 6−311+G(d,p) basis set, and Integral Equation

Formalism Polarized Continuum Model (IEFPCM) as solvation model were employed in the hybrid DFT calculations. With the purpose of determining orientation of PFOA anions on the surface (*e.g.*, parallel or perpendicular), formic acid and edge-sharing two-Fe(III) octahedral dimer were constructed to mimic the surface reaction. This simplified configuration saved a massive amount of computing time and, at the same time, adequately predicted the possible orientation of PFOA anions on the surface.

Fukui function and electrostatic potential (ESP) based on the DFT was used to predict the regioselectivity of reactive species (h^+ and •OH) attacking on the PFOA molecule. All of the calculations were performed using the Gaussian 09 software (Frisch et al., 2004). The geometry optimization and single-point energy calculations were executed using the B3LYP method with the 6-31+G(d,p) basis set. Fukui function is an important concept in the conceptual density functional theory (CDFT), and it has been widely used in prediction of reactive sites of electrophilic, nucleophilic and general radical attacks (Parr and Yang, 1984). Specifically, Fukui function is defined as:

$$f(r) = \left[\frac{\partial \rho(r)}{\partial N} \right]_{V(r)}$$

(5-1)

where $\rho(r)$ is the electron density at a point r in space, N is the electron number in the present system, and the constant term v in the partial derivative is the external potential. In the condensed version of Fukui function, the atomic population number is used to represent the electron density distribution around an atom. The condensed Fukui function on radical attack can be calculated as:

Electrophilic attack: $f_A^- = q_{N-1}^A - q_N^A$ (5-2)

Nucleophilic attack: $f_A^+ = q_N^A - q_{N+1}^A$ (5-3)

Radical attack: $f_A^0 = \dfrac{q_{N-1}^A - q_{N+1}^A}{2}$ (5-4)

where q^A is the atom charge of atom A at the corresponding state. The reactive sites on a molecule usually have larger values of Fukui index than other regions. In this study, the natural population analysis (NPA) charge is used to study the reactive sites, as it is considered to be one of the most suitable methods to calculate Fukui index (Oláh et al., 2002).

5.3. Results and discussion

5.3.1. Characterization of Fe/TNTs@AC composite

Figure 5-1 (a) presents an SEM image of calcinced Fe/TNTs@AC, displaying a cotton-like surface structure consisting of interwoven carbon- and Fe-modified TNTs. This structure is expected to be conducive to concentrating PFAS on the outer-shell surface and thereby facilitate the subsequent photocatalytic destruction of PFAS *in situ*. For comparison, the parent F-400 GAC (Gu et al., 2019) shows a flat, smooth, and layered-structure, where adsorption is expected to penetrate deep into the internal pores. **Figure 5-1 (b)** shows the EDS spectra of Fe/TNTs@AC, confirming the presence of the five major elements (C, O, Na, Fe, and Ti) on the surface of Fe/TNTs@AC. **Figure 5-2** presents EDS mappings of the elements, indicating that a small amount of Fe is well distributed on the surface of Fe/TNTs@AC, while Ti and C are the predominant elements. **Table 5-2** gives the relative percentiles of the elements.

(a)   (b)
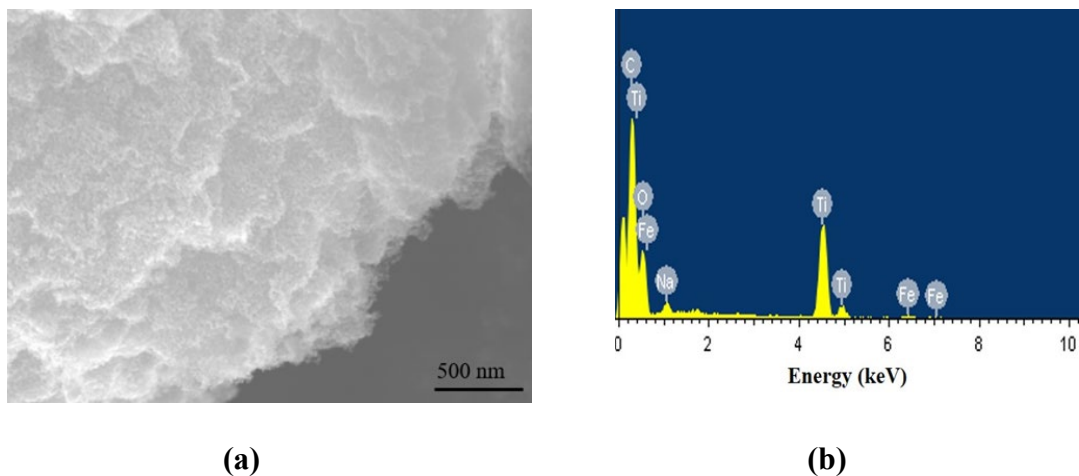
Figure 5-1. SEM image of (a) TNTs@AC and (b) Fe/TNTs@AC; and EDS spectra of (c) Fe/TNTs@AC.
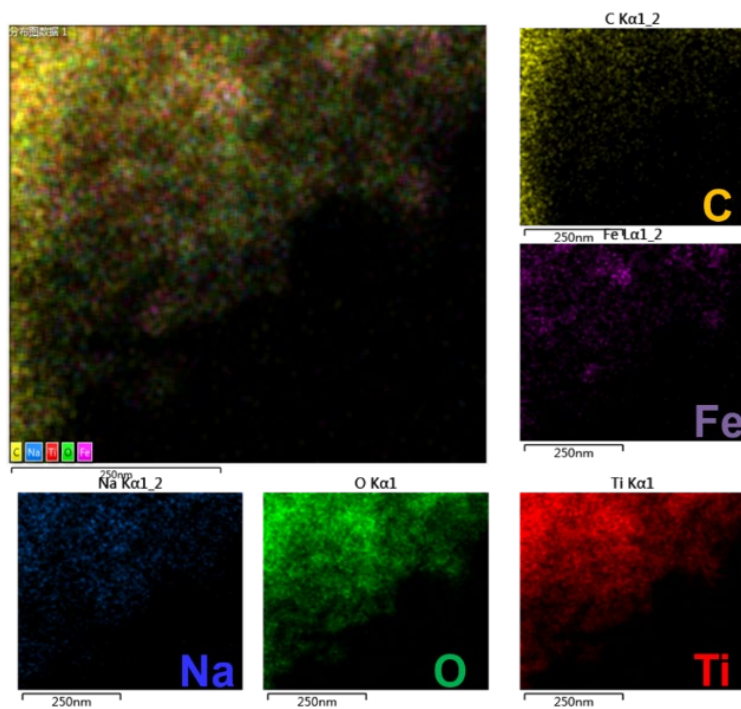
Figure 5-**2.** SEM-EDS mapping of the elements of Fe/TNTs@AC.

Table 5-2. Distribution of five elements for Fe/TNTs@AC in EDS.

element	weight, %	atomic, %

C	53.02	65.75
O	30.89	28.76
Na	1.51	0.98
Ti	13.99	4.35
Fe	0.59	0.16
Totals	*100.00*	

In TEM results, **Figure 5-3a** shows carbon nanoparticles (the dark dots) were attached on

the TNTs, with a particle size in the range of 5 to 20 nm, indicating that upon the alkaline

hydrothermal treatment, some carbon broke into nanoscale carbon particles. The carbon

nanoparticles not only facilitate adsorption of PFAS through enhanced hydrophobic interactions,

but facilitate electron transfer to result in enhanced photoactivity. **Figure 5-3b** present close-up

TEM images of the Fe- and carbon modified TNTs. The iron and carbon modifications are

expected to enhance both adsorption and photodegradation of PFAS. **Figure 5-3b** also reveal

that the TNTs have an outer diameter of ~20 nm and a length of ~100 nm. **Figure 5-3d** shows

the XRD patterns of F-400 GAC, TNTs@AC, and calcined Fe/TNTs@AC. **Table 5-3**

summarizes the six crystalline phases identified by the XRD analysis, where quartz-SiO2 and

moissanite (SiC) are likely due to the impurities from the parent AC. For F-400, two crucial

peaks at 26° and 43° can be assigned to the diffractions of crystal planes of graphite (002) and

(100), respectively (Le et al., 2012; Quiñones et al., 2014; Rey et al., 2012). For TNTs@AC, the peaks at 9.2°, 24.1°, 28.1°, 48.4°, and 61.4° are attributed to sodium trititanate (expressed as $Na_xH_{2-x}Ti_3O_7$) which are composed of corrugated ribbons of triple edge-sharing $[TiO_6]$ as skeletal structure with cation (*e.g.*, Na^+, H^+, Fe^{3+}) located at interlayer (Chen et al., 2002; Liu et al., 2016b; Ma et al., 2017). In particular, the peak located at 9.2° signifies the interlayer distance (crystal plane (020)) of sodium trititanate (Sun and Li, 2003). Furthermore, the peak located 26° represents crystal planes of graphite (002) suggesting that AC are intermingled with TNTs (Liu et al., 2016a). For Cal Fe/TNTs@AC, the peaks at 24.1°, 36.6°, 46.2°, 52.4°, 60.2°, and 73° are attributed to anatase(Li et al., 2018); the peaks at 26.1° and 31.4° can be assigned to graphite (crystal planes (002)) and hematite (α-Fe_2O_3, crystal plane (104)) (Sivula et al., 2011), respectively. Evidently, upon calcination and Fe-doping, the sodium tri-titanate of TNTs@AC was transformed to anatase. This observation agrees with the EDS mapping data. The HR-TEM images in Figure 11b display the layered crystalline structures of TNTs and Fe_2O_3 on the calcined Fe/TNTs@AC, revealing an interlayer distance of 0.35 nm for anatase and 0.27 nm for Fe_2O_3. The interlayer distance for anatase is much smaller than that for neat TNTs (0.75 nm for the crystal plane (020) of titanate), and 0.79 nm for unmodified TNTs@AC (Liu et al., 2016a), indicating the iron modification and calcination greatly altered the crystalline structure of TNTs@AC.
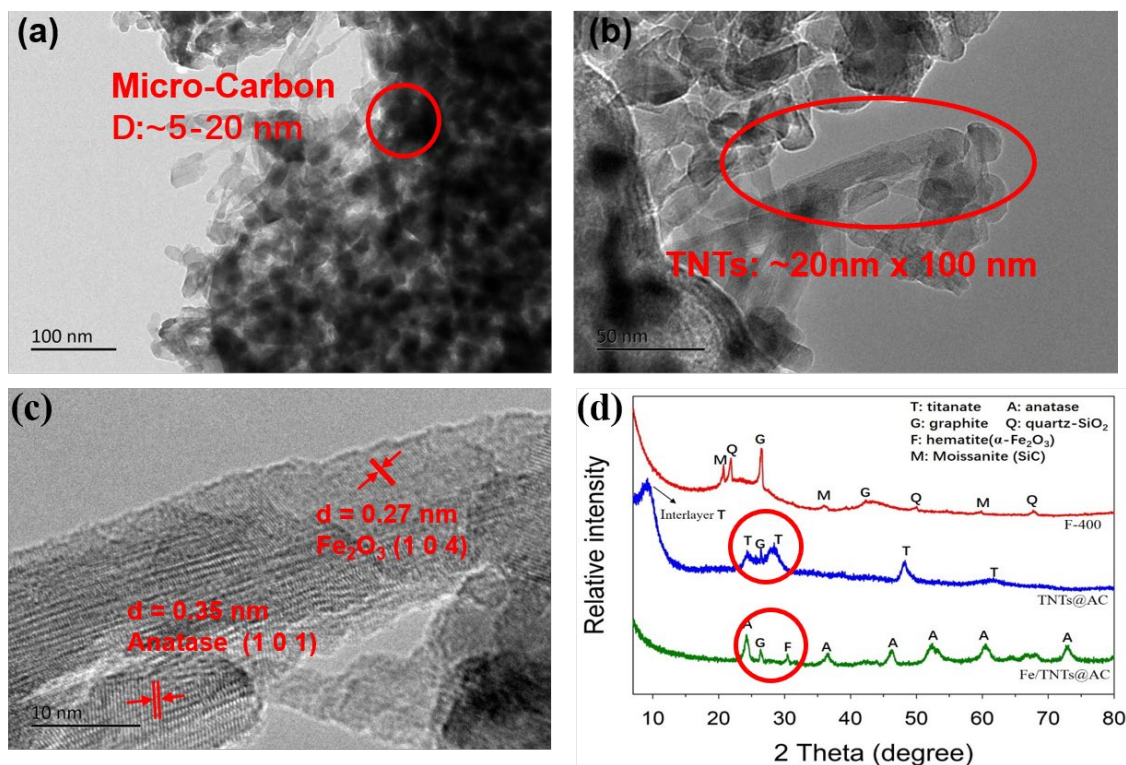
Figure 5-3. (a), (b), and (c) TEM image of Cal Fe/TNTs@AC and (d) XRD patterns of F-400, TNTs@AC, and Cal Fe/TNTs@AC.

Table 5-3. XRD pattern powder diffraction file (PDF).

composite	PDF #
graphite	41-1487
titanate	48-0693
anatase	21-1272
quartz-SiO_2	46-1045
moissanite(SiC)	42-1360
hematite(α-Fe_2O_3)	33-0664

Figure 5-4 displays X-ray photoelectron spectroscopy (XPS) spectra of Fe/TNTs@AC, and

Table 5-4 lists the corresponding atomic compositions of Fe/TNTs@AC and TNTs@AC. In a

previous work (Liu et al., 2016a), we identified that the formula of TNTs can be expressed as $Na_{0.7}H_{1.3}Ti_3O_7$. On the basis of carbon content in AC (60.11%) and Ti mass added, the overall mass ratio of AC to TNTs in the TNTs@AC is ~1.2:1. After Fe doping and calcination, the C content decreased from 60.11% to 51.08%, while the contents of Ti and O increased from 8.35% to 11.34% and from 24.40% to 30.52%, respectively. Meanwhile, the XPS data also indicated an Fe content of 0.68%, which was close to the EDS-based value (0.59%). **Figure 5-4b** shows the high resolution XPS spectra of Fe 2p, where the two main peaks, located at ~710 and ~723 eV, correspond to Fe $2p_{3/2}$ and Fe $2p_{1/2}$, respectively (Wu et al., 2015). This observation confirmed that Fe(II) was converted to Fe(III) resulting in the α-Fe_2O_3 phase, which is consistent with the TEM and XRD observations.
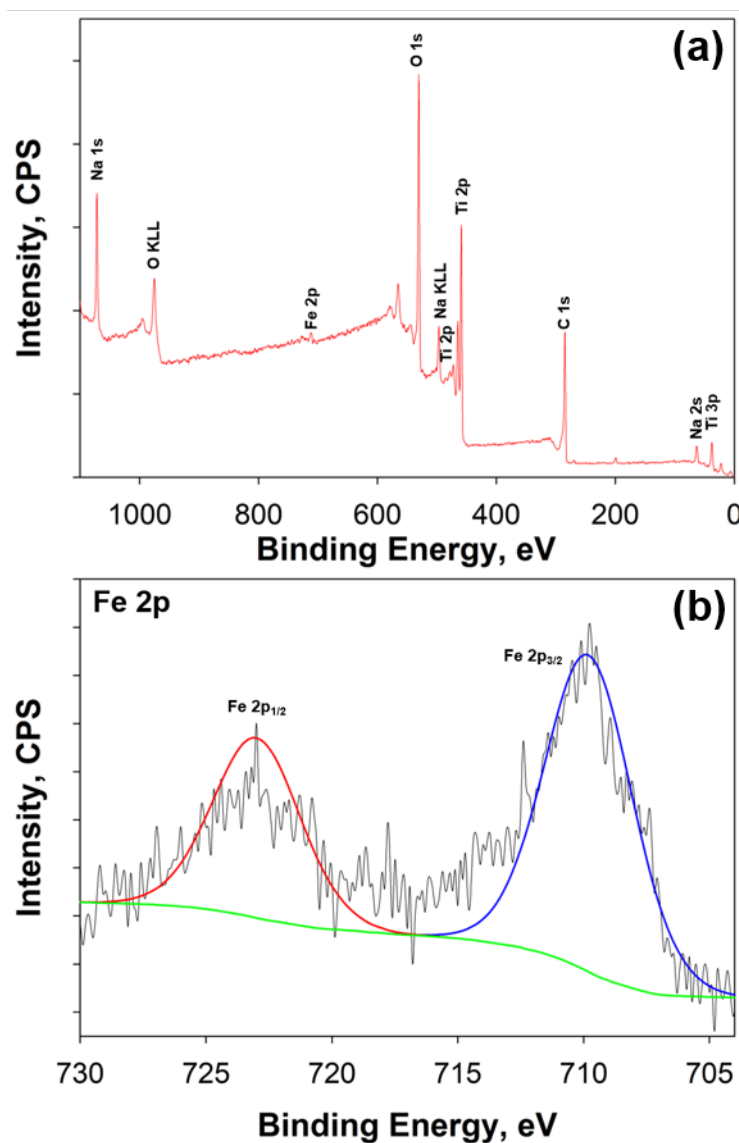
Figure 5-4. XPS spectra of Fe/TNTs@AC. (a) Survey XPS, and (b) high resolution of Fe 2p.

Table 5-4. Surface atomic percentage of AC and TNTs@AC obtained by XPS.

Materials	Element atomic percentage (%)					
	C	O	Na	Ti	Fe	Cl
TNTs@AC	60.11	24.40	5.14	8.35	0	2.01
Fe/TNTs@AC	51.08	30.52	5.42	11.34	0.68	0.95

Figure 5-5 shows pore size distribution of TNTs@AC and Fe/TNTs@AC. TNTs@AC displayed a bimodal pore size distribution profile with a primary peaking at ~4 nm and a secondary peaking at 2−2.5 nm. The pore size distribution from 4 to 10 nm mimics that of the parent AC, whereas the pore size distribution for <4 nm pores can be attributed to conversion of larger pores (>10 nm) of TNTs into more micropores in TNTs@AC. The similar distribution profile was observed for Fe/TNTs@AC. However, Fe/TNTs@AC showed a much higher change in dV/dD from ~4 nm to ~10 nm than TNTs@AC, suggesting that loading of Fe and calcination blocked some large and deep pores. Contrary to the BET surface area, the Fe loading and the calcination treatment of TNTs@AC increased the pore volume from 0.55 cm^3 /g for TNTs@AC to 0.61 cm^3 /g for Fe/TNTs@AC, which is in favor of rapid adsorption rate for PFOA.
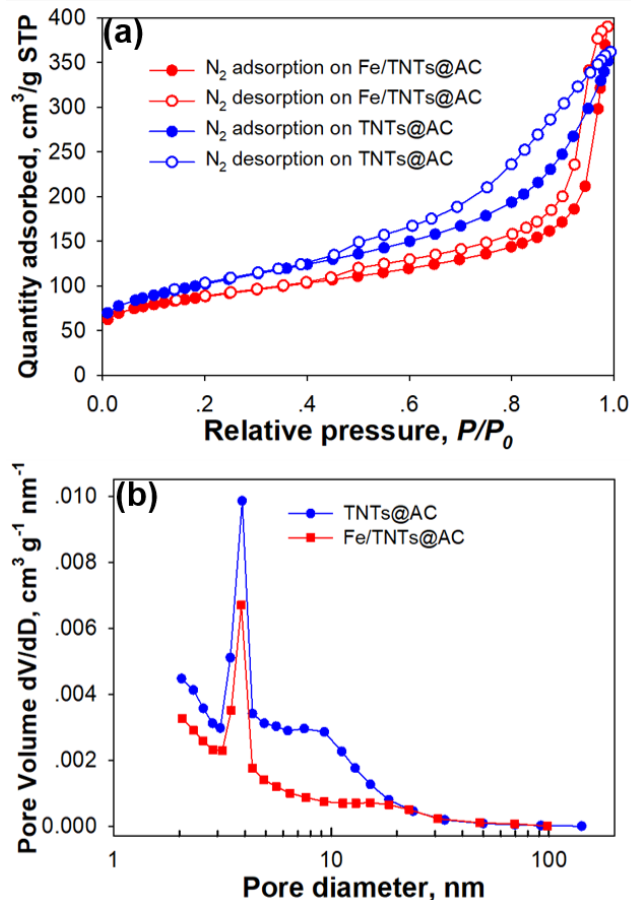
Figure 5-5. (a) N$_2$ adsorption-desorption isotherms, and (b) pore size distributions of unmodified TNTs@AC and Fe/TNTs@AC. V: Pore volume, and D: pore diameter.

5.3.2. Adsorption of PFOA

Adsorption kinetics and isotherm. Fe/TNTs@AC exhibited excellent adsorption rate for both PFOA. **Figure 5-6a** shows adsorption kinetics of PFOA. More than 95% of PFOA (100 µg /L) was rapidly adsorbed in 5 min using 1 g /L of Fe/TNTs@AC, and over 99% was adsorbed after 60 min. Concentrations of PFOA before and after adsorption were measured in experiments, and the uptake (q_t, mg g^{-1}) of PFOA on our composite materials and removal efficiency (R, %) were determined via:

$$q_t = \frac{(C_0 - C_t)V}{m} \qquad (5\text{-}5)$$

$$R = \frac{(C_0 - C_t)}{C_0} \times 100\% \qquad\qquad\qquad (5\text{-}6)$$

where q_t (mg g^{-1} or μg g^{-1}) is the uptake of PFOA at time t (min); C_0 and C_e (mg/L or μg/L)

stand for the PFOA concentrations at $t = 0$ and equilibrium, respectively; m (g) is the mass of

composite materials; and V (L) is the total volume of the solution.
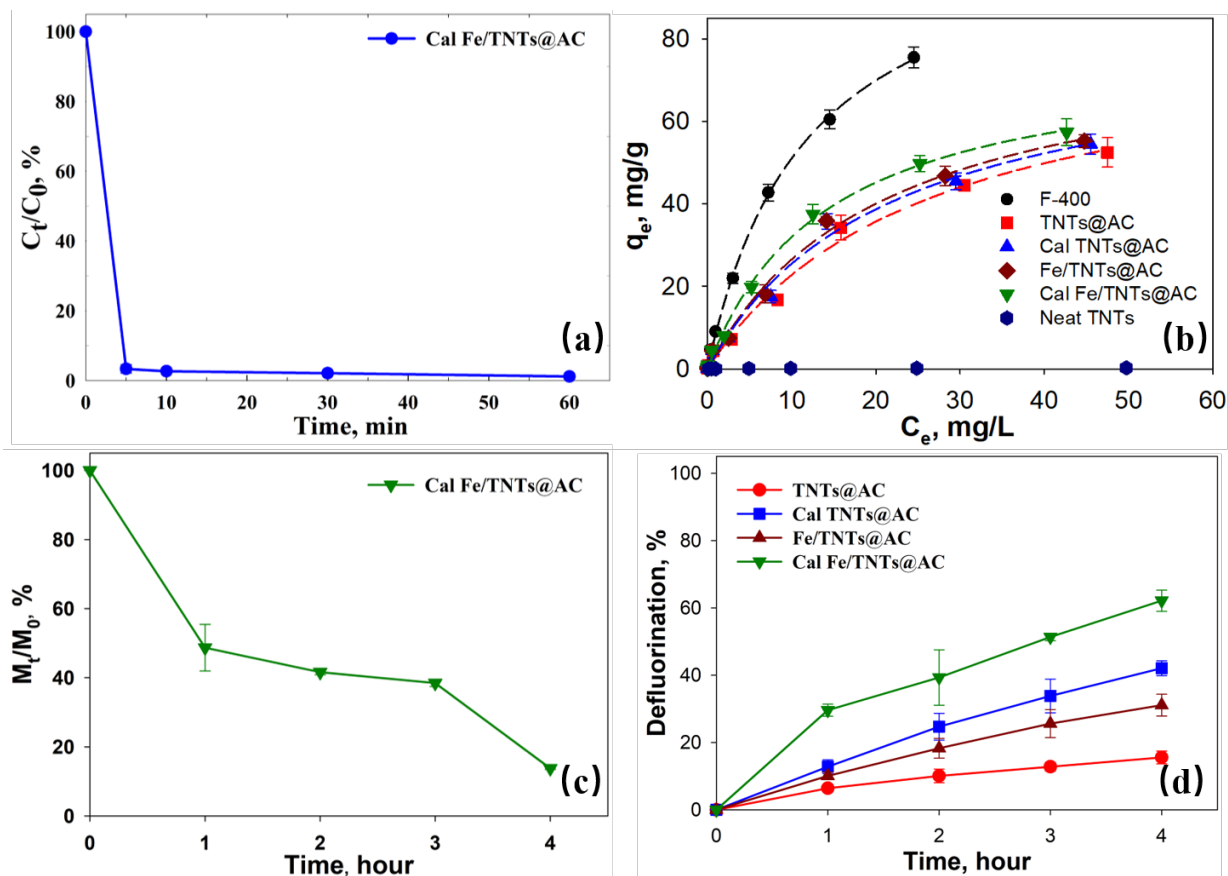
Figure 5-6. (a) Adsorption kinetics, (b) adsorption isotherms, (c) photodegradation kinetics, and (d) defluorination of PFOA. Experimental conditions: (a), (c), and (d) initial [PFOA] = 100 μg/L, material dosage = 1.0 g/L, solution volume = 40 mL, pH = 7.0 ± 0.3; (b) initial [PFOA] = 100 μg/L – 100 mg/L; material dosage = 1.0 g/L, solution volume = 40 mL, and pH = 7.0 ± 0.3, temperature = 25 °C and reaction time = 24 h.

The rapid adsorption allows for efficient removal of PFOA from bulk water with a small hydraulic residence time (HRT) (i.e., a small reactor). Moreover, the adsorption pre-concentrates PFOA from a large volume of water onto a small volume of Fe/TNTs@AC, enabling the subsequent photocatalytic degradation to be carried out in a much smaller volume of photo-reactor with much less energy consumption compared to directly treating the bulk raw water. For comparison (**Figure 5-7)**, original F-400 (AC) and alkline condition treated F-400 (AC) showed high removal of PFOA, but slower kinetics, *i.e.*, ~ 70% of PFOA were adsorbed in first 5 min and > 99% of PFOA were adsorbed within 2 h at equilibrium. In contrast, neat TNTs only adsorbed ~ 4% of PFOA. Thus, these observations indicate that the effective removal capacity of PFOA by composite materials was dominantly attributed to the excellent adsorption capability of Filtrasorb 400® AC (Ochoa-Herrera and Sierra-Alvarez, 2008). But modification induced new mechanism which greatly fasten adsorption kinetic rate. Furthermore, the pseudo first-order model (Eq. 5) and pseudo second-order model (Eq. 6) are employed to interpret the kinetic data (Ho and McKay, 1999):

Pseudo first-order model: $q_t = q_e - q_e^{-k_1 t}$ (5-7)

Pseudo second-order model: $\frac{t}{q_t} = \frac{1}{k_2 q_e^2} + \frac{t}{q_e}$ (5-8)

where q_t and q_e are the PFOA uptakes ($\mu g\ g^{-1}$) at time t (min) and equilibrium, respectively, k_1 is the first-order rate constant (min^{-1}), and k_2 is the second-order rate constant (g ($\mu g \cdot min$)$^{-1}$).
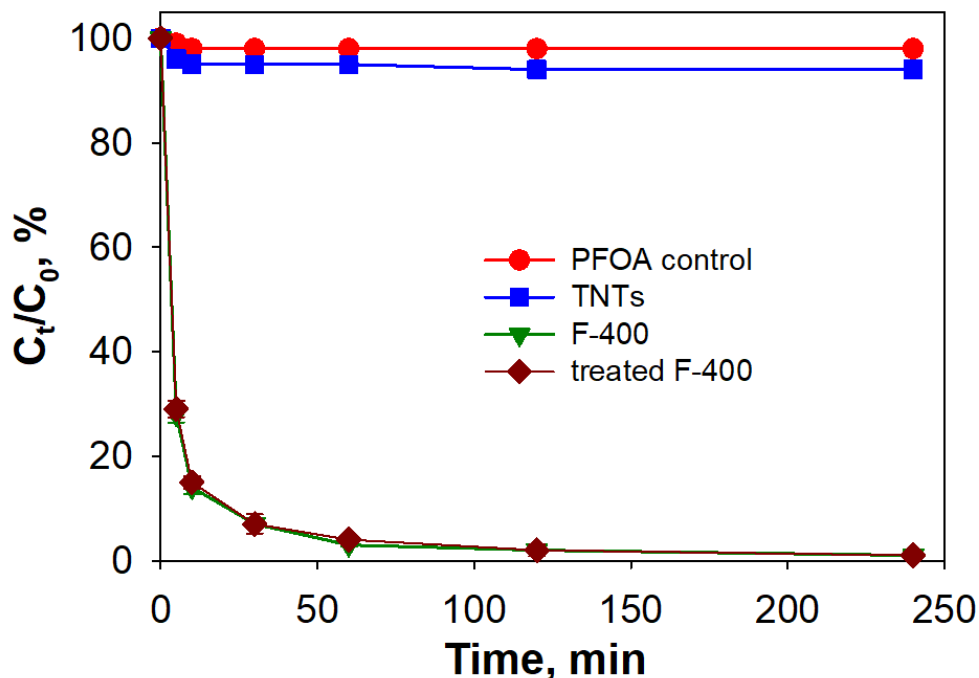
Figure 5-7. Adsorption kinetics of F-400, neat TNTs, and treated F-400. Conditions: Initial [PFOA] = 100 μg/L, material dosage = 1.0 g/L, solution volume = 40 mL, pH = 7.0 ± 0.3.

The pseudo first-order model can accurately describe adsorption kinetics during which diffusion through a boundary liquid film plays significant role, whilst the pseudo second-order model can better fit the adsorption kinetics that chemical interaction between two substances are dominant (Ho and McKay, 1999). As shown in **Table 5-5**, pseudo second-order model (R^2 = 0.997) fits the experimental kinetic data much better than the pseudo first-order (R^2 = 0.894) for Fe/TNTs@AC, whereas both model fit AC's experimental kinetic data very well (R^2 =0.996 vs. R^2 =0.976). Thus, the rate limit step in PFOA adsorption by Fe/TNTs@AC was possibly chemical interaction (*e.g.*, surface complexation with hydroxyl groups on iron oxide), rather than intraparticle diffusion (Han et al., 2015).

Table 5-5. Kinetic model parameters for adsorption of PFOA.

models	parameters	materials	
		Fe/TNTs@AC	F-400
pseudo	k_1 (min^{-1})	0.330	0.317
first-order	R^2	0.894	0.976
pseudo	k_2 (g (µg·min)$^{-1}$)	8.54×10^{-3}	9.06×10^{-3}
second-order	R^2	0.997	0.996

Figure 5-6b shows the adsorption isotherm of PFOA by raw and composite materials. It is

noted that neat TNTs showed only negligible PFOA adsorption capacity (< 10 μg g^{-1}) due to its

negatively charged surface (pH$_{pzc}$ = 2.57 for TNTs) (Liu et al., 2016b, 2013), which repulsed

anionic PFOA (C$_7$F$_{15}$COO$^-$). Both classic Langmuir model and Freundlich model were applied

to fit adsorption isotherm data. The Langmuir isotherm model assumptions include that the

homogeneous and equivalent adsorption sites are located on a monolayer surface and no

interactions between adsorbate molecules should be considered (Langmuir, 1918), whereas the

Freundlich isotherm model is an empirical equation describing the adsorption behavior on an

energetically heterogeneous surface(Freundlich, 1907). The Langmuir model and Freundlich

model are expressed as Eq. 5-9 and Eq. 5-10 below, respectively, and fitting parameters are

shown in **Table 5-6**:

Langmuir isotherm model: $q_e = \dfrac{Q_{max}bC_e}{1+bC_e}$ $\hspace{2cm}$ (5-9)

Freundlich isotherm model: $q_e = K_F C_e^{1/n}$ $\hspace{2cm}$ (5-10)

where C_e is the equilibrium concentration of PFOA, Q_{max} (mg g^{-1}) is the maximum

adsorption capacity of the adsorbent, and b (L mg^{-1}) is the Langmuir constant related to the

affinity of binding sites and is also a measure of free energy of adsorption; K_F (mg (g·(L mg$^-$

^{1})$^{1/n}$)$^{-1}$) is the Freundlich constant related to the adsorption capacity of the adsorbent, and n is the

heterogeneity factor indicating the adsorption intensity of the adsorbent.

Table 5-6. Adsorption isotherm model parameters for adsorption of PFOA.

models	parameters	materials					
		F-400	Cal Fe/TNTs @AC	5% Fe/TNTs @AC	Fe/TNTs @AC	Cal TNTs@ AC	TNTs(AC
Langmuir isotherm model	Q_{max} (mg g^{-1})	110.6	84.5	95.97	81.4	80.2	77.6
	b (L mg^{-1})	0.089	0.063	0.077	0.052	0.047	0.041
	R^2	0.999	0.992	0.996	0.994	0.991	0.997
Freundlich isotherm model	K_F mg (g·(L mg^{-1})$^{1/n}$)$^{-1}$	12.38	8.84	10.84	6.95	6.32	5.89
	n	1.75	1.96	1.88	2.08	1.84	1.81
	R^2	0.993	0.971	0.959	0.968	0.972	0.959

The fact that Langmuir model fits better for the AC-based photocatalyst ($R^2 > 0.99$)

demonstrated that homogeneous monolayer adsorption is the major manner for PFOA anions

(Foo and Hameed, 2010). The maximum Langmuir adsorption capacity of PFOA for

TNTs@AC, Fe/TNTs@AC (non-calcined), calcined (Cal) TNTs@AC, and calcined (Cal)

Fe/TNTs@AC were 77.6, 81.4, 80.2, and 84.5 mg g^{-1}, respectively. As comparison, F-400

showed excellent adsorption capacity of 110.6 mg g^{-1} similar to previously reported value of

112.1 mg g^{-1} (Ochoa-Herrera and Sierra-Alvarez, 2008). The decreased adsorption capacity for

adsorptive photocatalyst was anticipated since neat TNTs barely adsorbed any PFOA. However,

Fe doping and calcination can slightly enhanced the PFOA adsorption capacity. **Figure 5-8** compared the zeta potential of TNTs@AC, Fe/TNTs@AC (non-calcined), Cal TNTs@AC, and Cal Fe/TNTs@AC. The pH_{pzc} value of Cal Fe/TNTs@AC increased to 5.2 from 3.8 for TNTs@AC, suggesting Fe doping partially neutralized the negative surface charge of TNTs@AC and thus reduced the repulsive interaction between materials and PFOA anions. Therefore, increasing the Fe doping content from 1% to 5% significantly improved ~14% of PFOA adsorption based on Langmuir model fitted Q_{max} as shown in **Figure5-9** and **Table 5-6**.
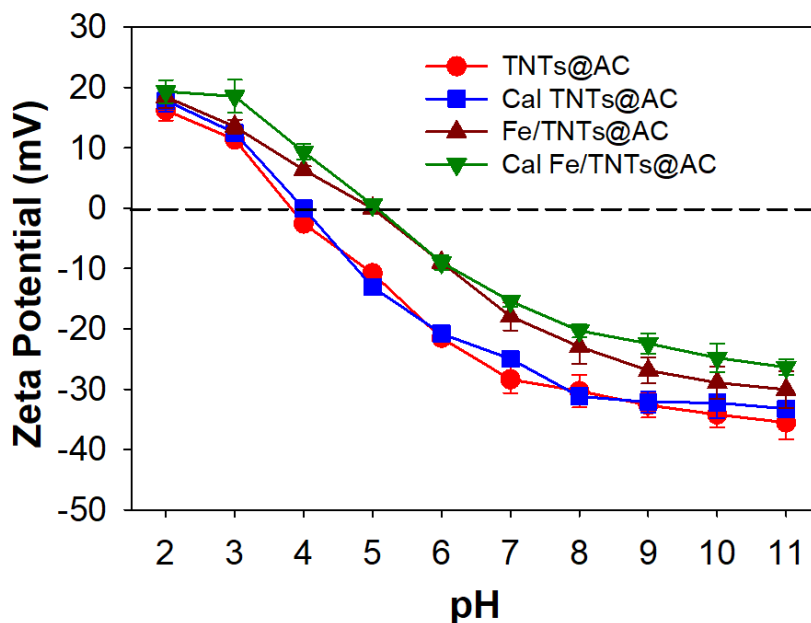
Figure 5-8. Zeta potential of Cal Fe/TNTs@AC, Cal TNTs@AC, Fe/TNTs@AC, and TNTs@AC.
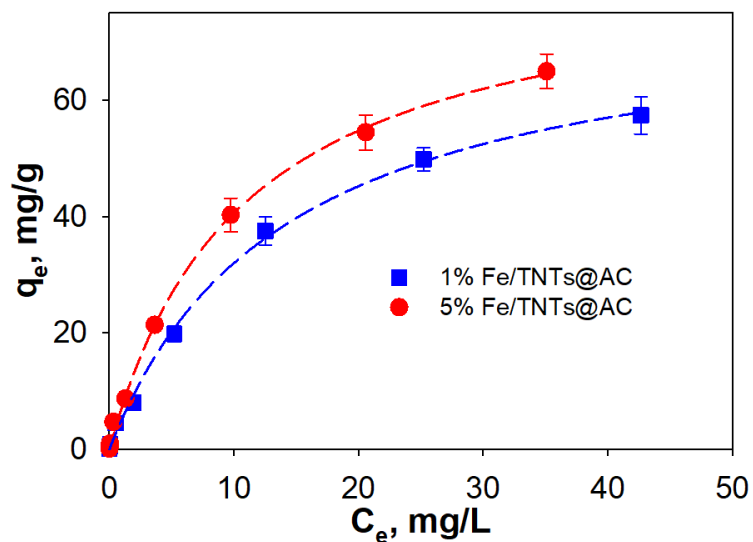
Figure 5-9. Adsorption isotherm of PFOA by 1% Fe/TNTs@AC and 5% Fe/TNTs@AC. Conditions: Initial [PFOA] = 100 μg/L – 100 mg/L; material dosage = 1.0 g/L, solution volume = 40 mL, and pH = 7.0 ± 0.3, temperature = 25 °C and reaction time = 24 h.

**Adsorption mechanisms.** As indicated by pseudo second-order model (Eq. 5-8), the rate limit step of PFOA adsorption was likely the chemical interaction on the surface of Cal Fe/TNTs@AC, rather than uptake by deep-pore sites on parent AC (also confirmed by BET data). Generally, PFOA adsorption process were controlled by hydrophobic interactions and electrostatic interactions (Deng et al., 2012; Higgins and Luthy, 2006). PFOA consists of a hydrophilic "head group" (carboxylate group) and a hydrophobic "tail group" ($-CF_3(CF_2)_6$ group). The tail group of PFOA is particularly inert to polar chemicals/solvents. Therefore, the tail group can strongly interact with the hydrophobic "micro carbon" on surface of Cal Fe/TNTs@AC (Liu et al., 2016a). Further, the α-Fe_2O_3 on surface carried positive charge at neutral pH (Breeuwsma and Lyklema, 1973) and thus attracted dissociated carboxylate group (COO^-, p$K_a \leq 3$ (Burns et al., 2008)) of PFOA anions. Therefore, such electrostatic attraction

would greatly improve the surface complexation of PFOA head on the surface of Cal

Fe/TNTs@AC. The dual role of Fe and "micro- carbon" could alter the spatial orientation of

PFOA molecules adsorbed on our novel adsorptive photocatalysts. Herein, we proposed a new

concept of "vertical adsorption" to "parallel adsorption" (shown in **Figure 5-10a**) as the

adsorption manner for PFOA anions, which is verified by the DFT calculation results (see details

in **Figure 5-11**). DFT calculations were employed to analyze the orientations of adsorbed PFOA

anions on Fe/TNTs@AC surface. **Figure 5-11** shows the resulting optimized molecular

orientations with minimum energy from the frequency and optimization calculations. The angle

between the hydroxyl group and carbon chain of PFOA is between 110º and 120º (**Figure 5-

11a**). The angles remain in the same range for mono- and bi-dentate complexed PFOA (**Figure

5-11b** and **c**). Based on the structural properties, PFOA adsorbed through mono-dentate

complexation is likely oriented "parallel" to the Fe(III) dimer, *i.e.*, the iron oxide surface; whilst

PFOA via bi-dentate complexation is "perpendicular" to the iron oxide surface in the head-in

mode. However, it should be noted that the "parallel" or "perpendicular" is not mathematically

strict-defined orientation, but with allowable range up to ~10º in difference. In both cases, the

head-in adsorption is expected to facilitate head-first decarboxylation reactions.

The parallel adsorption could bring several advantages including: 1) more stable interaction

to effectively concentrate PFOA onto the photocatalyst surface; 2) shorter distance between

PFOA and surface of adsorptive photocatalyst allows sufficient use of photo-generated h^+ or e^-

for PFOA decomposition and mineralization.
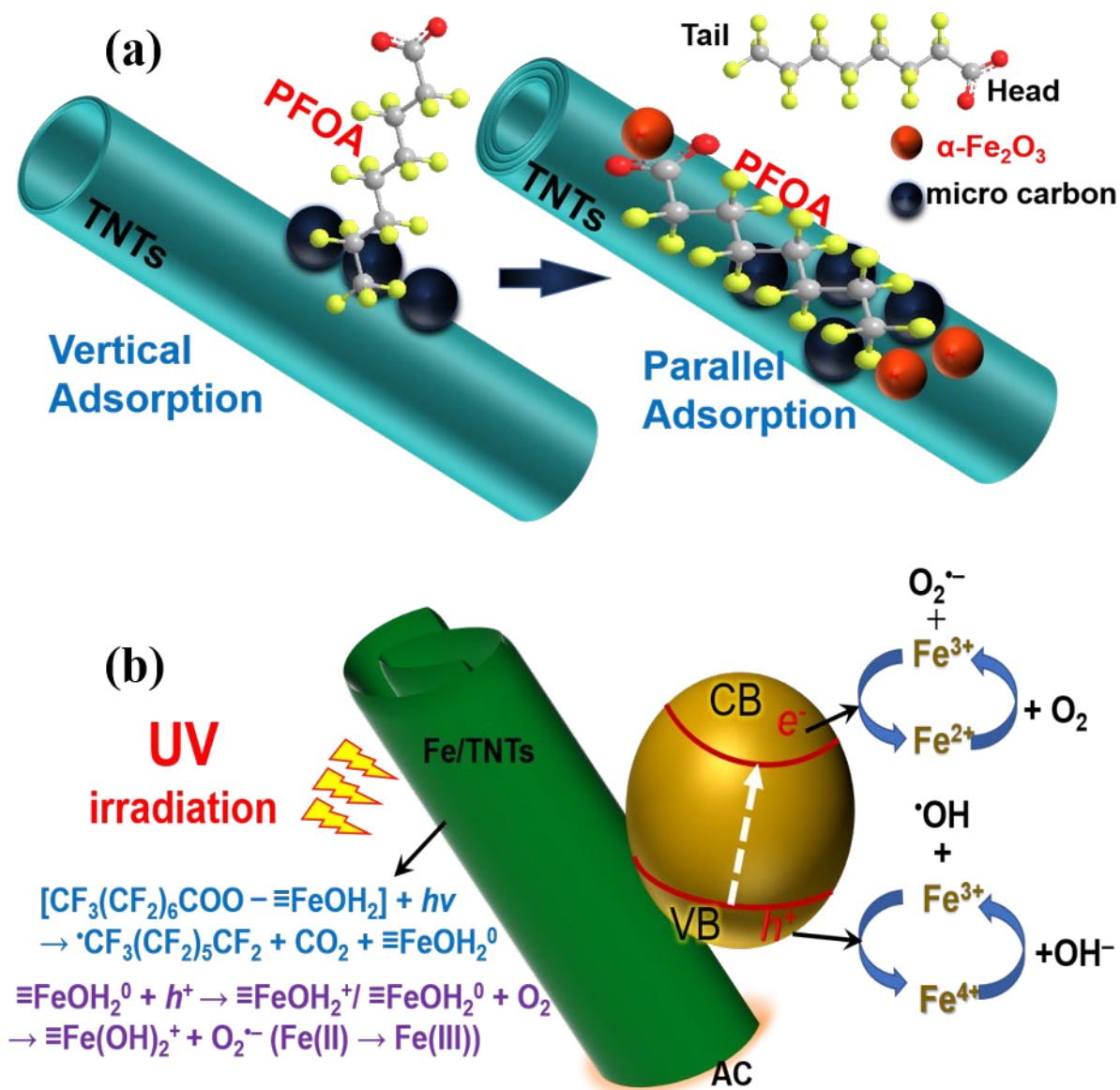
Figure 5-10. Schematic diagrams of PFOA adsorption (a) and photodegradation (b) mechanisms.
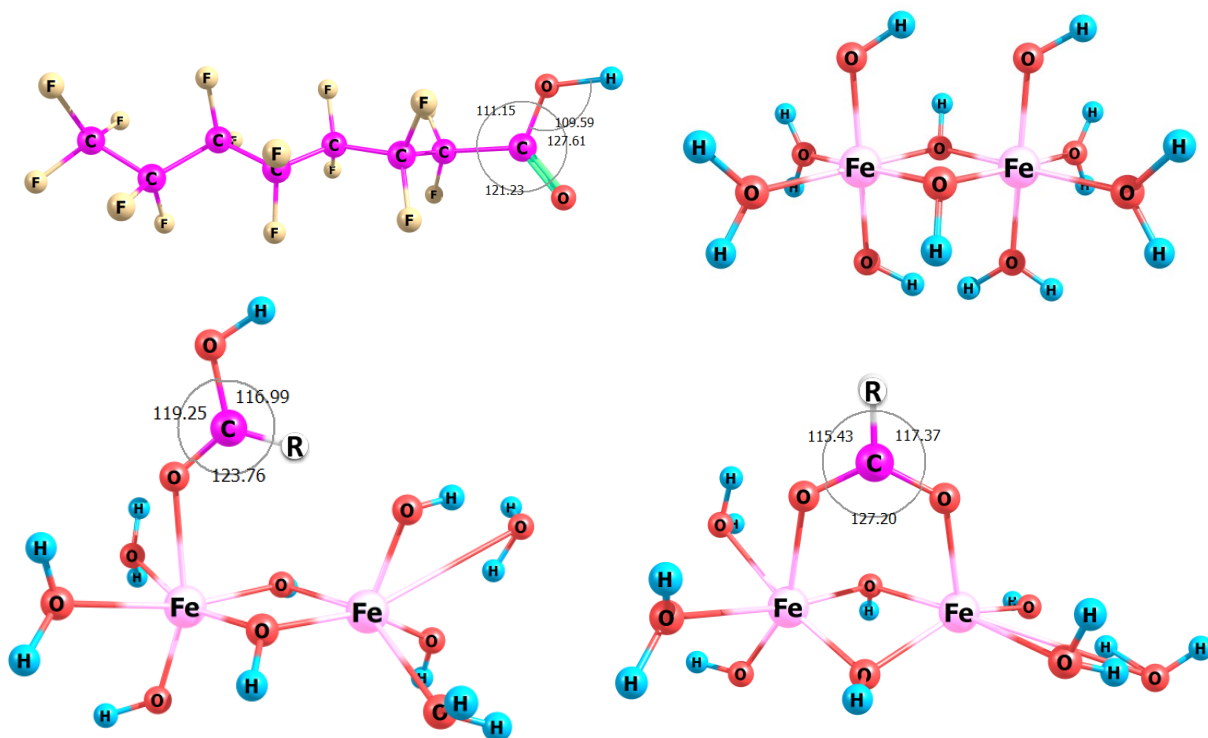
Figure 5-11. (a) PFOA, (b) Fe(III) dimer, (c) mono-complexation, and (d) bi-dentate complexation with optimized geometries calculated at B3LYP/6−311+G(d,p) level of theory. The numbers indicate angular values between bonds.

5.3.3. Photodegradation of PFOA

As shown in **Figure 5-12**, less than 3% of PFOA defluorination was observed in PFOA photolysis under dierect UV irradiation and on F-400 surface (PFOA pre-loaded on AC), confirming direct UV irradiation cannot efficiently photodegrade PFOA and F-400 has very limited photocatalytic activity. **Figure 5-6c** shows that Cal Fe/TNTs@AC was able to highly efficiently degrade PFOA (i.e., breakdown into other compounds), and >90% of pre-concentrated PFOA was photodegraded in 4 h. The pseudo first-order kinetic model and retarded first-order kinetic model were tested to fit the PFOA photodegradation by Cal Fe/TNTs@AC kinetic data, and **Table 5-7** presents the best fitted parameters.

126
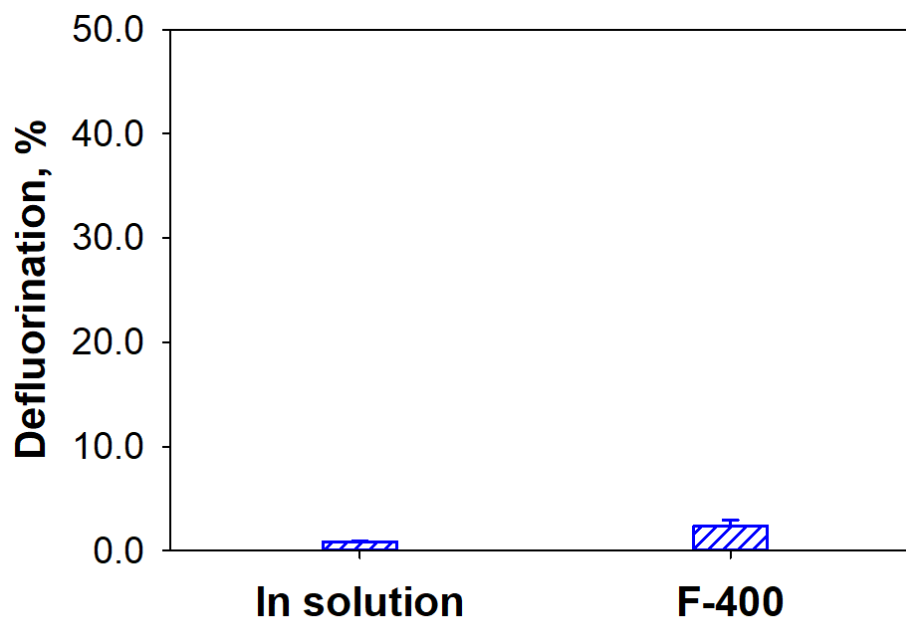
Figure 5-12. PFOA defluorination in solution and on F-400 in 4 h UV irradiation.
Conditions: Initial [PFOA] = 100 µg/L, material dosage = 1.0 g/L, solution volume = 40 mL, pH
= 7.0 ± 0.3.

Table 5-7. Kinetics model parameters for photodegradation of PFOA.

		materials	
models	**parameters**	Cal	
		Fe/TNTs@AC	
pseudo	k_1 (h^{-1})	1.27	
first-order	R^2	0.825	
retarded	α (h^{-1})	0.011	
	k_α (h^{-1})	0.26	
first-order	R^2	0.859	

Pseudo first-order kinetic model: $\ln\left(\frac{M_t}{M_0}\right) = -k_1 t$ (5-7)

Retarded first-order kinetic model: $\frac{M_0}{M_t} = \frac{1}{(1+\alpha t)^{-k_a/\alpha}}$ (5-8)

where M_0 and M_t are the PFOA mass (g) at time 0 and t (h), respectively, k_1 is the first-order rate constant (h^{-1}), k_a is the retarded first-order rate constant (h^{-1}), and α is the retardation factor indicating the extent of departure from the pseudo-first-order behavior.(Weber, 2001)

Retarded first-order model integrates the factor of α in the rate constant following an empirical approach and thus better describe the first-order kinetics with the gradual deviation (Han et al., 2015). The gradual deviation usually relates to gradually slowed reaction rate which caused by 1) diluted pollutant concentration when reaction keeps going on; and 2) stronger competition for reactive sites. The model fitting results suggested that retarded first-order model ($R^2 > 0.99$) interpreted the photodegradation kinetics slightly better than pseudo first-order. During UV irradiation, the concentration of PFOA adsorbed on/near photocatalytic sites on Cal Fe/TNTs@AC decreased with time, and therefore, the rate of PFOA photodegradation could slightly decrease. Meanwhile, a large amount of shorter chain perfluoroalkyl carboxylic acid were produced and competed for reactive sites, further reducing the photodegradation rates. These two reasons explained the better fitness of retarded first-order model to the photodegradation data.

Consistently, **Figure 5-6d** shows that Cal Fe/TNTs@AC converted ~69.5% of fluorine (F) in PFOA anions into F^- ions (*i.e.*, the defluorination process), which is 1.5, 2, and 4 times higher than Cal TNTs@AC, Fe/TNTs@AC (non-calcined), and TNTs@AC, respectively. UV-DRS result (**Figure 5-13**) shows that calcined Fe/TNTs@AC displayed a blue shift compare to TNTs@AC, indicating calcined Fe/TNTs@AC can absorb more ligh in visible light range

wavelength and further generate more reactive oxidative species (ROS) (i.e. hydroxl radical, proven by PL experimental result in **Figure 5-14**). Hence, the calcination and Fe-modification successfully enhanced the photocatalytic activity of the composite materials.
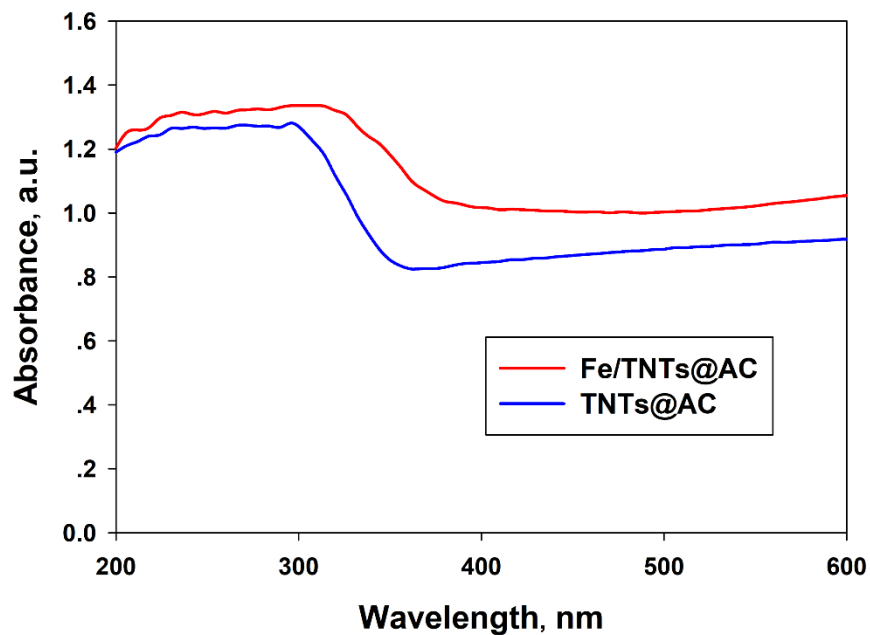
Figure 5-13. UV-DRS spectra of TNTs@AC and calcined Fe/TNTs@AC
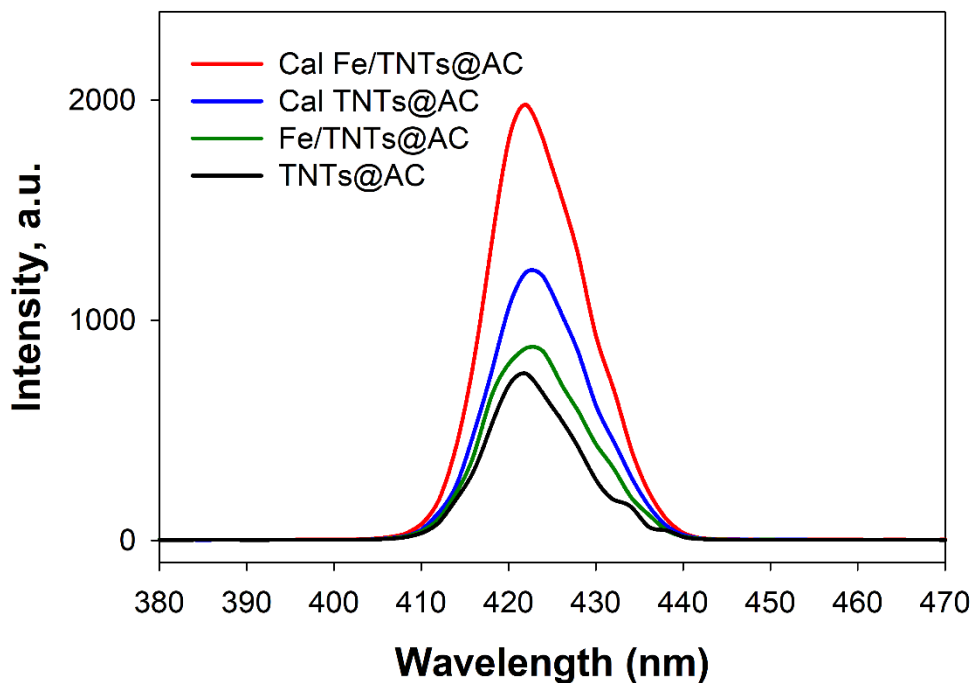
Figure 4-14. PL spectra of TNTs@AC, Fe/TNTs@AC (non-calcined), calcined TNTs@AC and calcined Fe/TNTs@AC in the presence of terephthalic acid after UV irradiation. Conditions: material dosage = 1g /L, NaOH = 0.4 M, Terephthalic Acid = 0.1 M, Irradiation time = 1 h, excitation = 315 nm, and emission = 360 – 490 nm

To optimize the photocatalytic performance of Cal Fe/TNTs@AC, different calcination temperature and Fe dope contents were tested for PFOA photodegradation. Adsorption of PFOA by Fe/TNTs@AC calcined at 300 °C, 550 °C, 650 °C, and 850 °C reached equilibrium in 2 hour with the >99% removal of PFOA. **Figure 5-15a** shows that Fe/TNTs@AC calcined at 550 °C displayed the highest defluorination rate, with ~62% fluorine in PFOA converted to F– ions in 4 h of UV irradiation. Increasing the temperature to 650 °C and 850 °C decreased the defluorinate to 57% and 16%, respectively. Conversely, lowering the calcination temperature to 300 °C resulted in only 37% defluorination. Thus, 550 °C was considered the optimal calcination

temperature for Fe/TNTs@AC prepared under the given recipe.   Thus, 550 °C is considered the best calcination temperature. It has been reported that titanate begins to be transferred into the anatase phase at at 190 °C (Mao and Wong, 2006). As the calcination temperature increases, the formed anatase phase would have larger crystallites with the ability to absorb a broader range of light (Le et al., 2012; Yang et al., 2008). However, when calcination temperature further increases to 600 °C, anatase starts to transform to the rutile phase, which has much lower photocatalytic activity than the anatase phase (Yang et al., 2008; Yoganarasimhan and Rao, 1962). Thus, the best calcination temperature range falls between 500 to 600 °C. However, the effect of the calcination temperature on the carbon coatings was not explored in this limited-scope study.
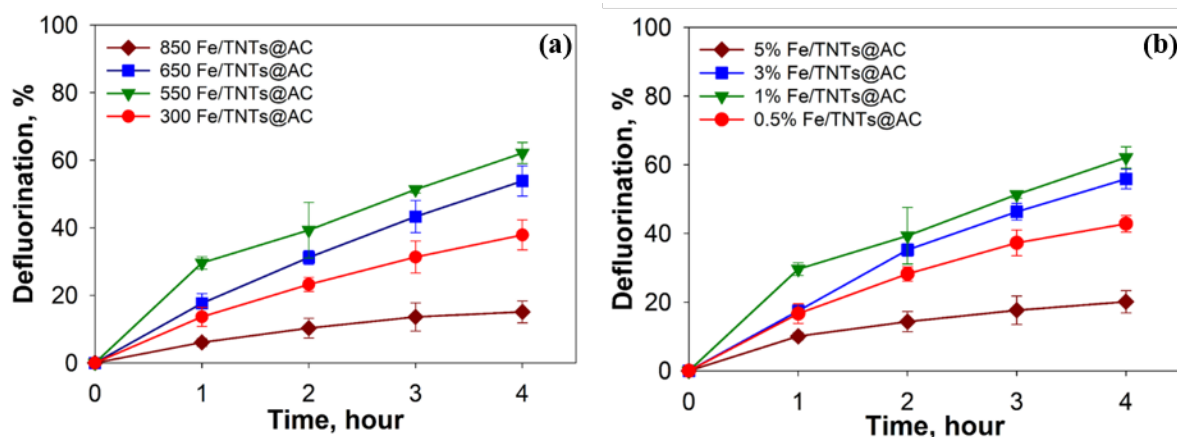
Figure 5-15. (a) Defluorination of PFOA by Fe/TNTs@AC calcined at 300 ℃, 550℃, 650℃, and 850℃, and (b) defluorination of PFOA by Fe/TNTs@AC with Fe content of 0.5%, 1%, 3%, and 5%. Experimental conditions: initial [PFOA] = 100 μg/L, material dosage = 1.0 g/L, solution volume = 40 mL, pH = 7.0 ± 0.3.

Similarly, more than 99% of PFOA were adsorbed by 0.5%, 1%, 3%, and 5% Fe/TNTs@AC (all calcinated at 550 ℃) within 2 h. **Figure 5-15b** shows that Fe/TNTs@AC

with 1% of Fe offered the highest defluorination rate, with a 4 h defluorination of ~62%.

However, further increasing the Fe content to 3%–5% decreased the defluorination extent to 57%

and 20%, respectively. Conversely, lowering the Fe content to 0.5% resulted in only 43% of

PFOA defluorinated. Although increasing Fe doping could neutralize the negatively charged

surface of TNTs@AC and facilitate PFOA adsorption, an excess of Fe would act as

recombination centers for the photo-generated electrons and holes due to quantum tunneling

effects (Zhang and Lei, 2008; Zhou et al., 2006, 2005), resulting in reduced photodegradation

rates. Moreover, excessive loading of Fe_2O_3 on the TNTs surface may hamper the photocatalytic

activity of anatase.

5.3.4. Stability and reusability of photocatalyst

The stability of Fe/TNTs@AC (1% and 550 °C) was tested at a broad range of solution pH.

First, **Figure 5-16** shows that about 99% of PFOA was adsorbed by Fe/TNTs@AC in the pH

range from 4.0 to 11.0. **Figure 5-17** shows the pH effect on PFOA photodegradation during 4 h

UV irradiation. The photodegradation activity significantly decreased under alkaline condition

(pH > 9), probably due to two reasons: 1) the iron oxides surface became more negative at high

pH (Wei et al., 2017a), resulting in less adsorption of PFOA anions and subsequent degradation

on the surface; and 2) more available hydroxyl ions could react with photogenerated holes to

produce hydroxyl radicals which are less effective to degrade PFOA (Lawless et al., 1991). Thus,

neutral or acidic conditions are preferred for PFOA photodegradation using Fe/TNTs@AC.

Given that composite material can be regenerated in small volume of water, it would be easy to

adjust pH. Therefore, this "concentrate-&-destroy" strategy shall be widely used in some alkline

pH water body.
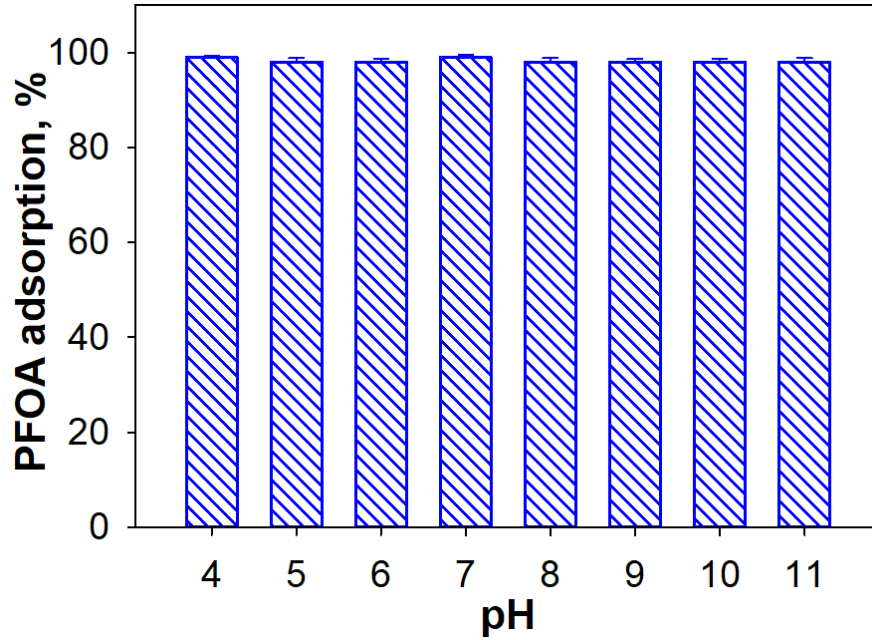
Figure 5-16. pH effects on PFOA adsorption at equilibrium. Experimental conditions: initial [PFOA] = 100 μg/L, material dosage = 1.0 g/L, solution volume = 40 mL, and reaction time = 2 h.
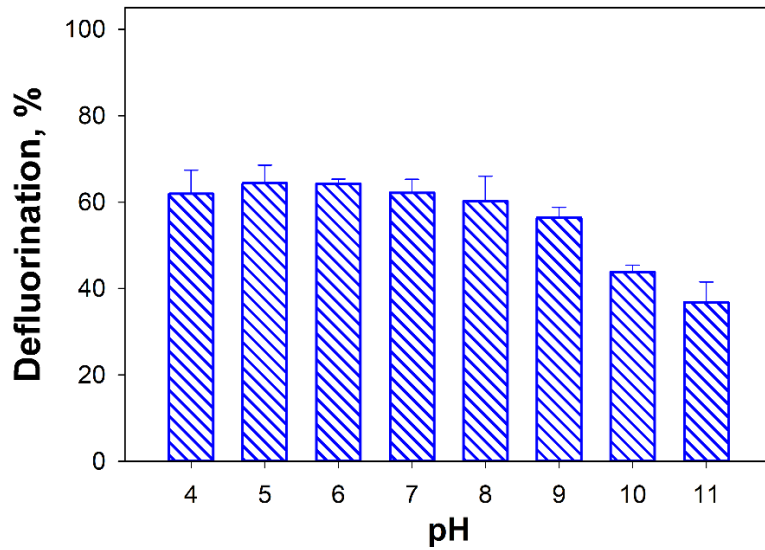
Figure 5-17. pH effect on PFOA defluorination. Experimental conditions: Initial [PFOA] = 100 μg/L, material dosage = 1.0 g/L, solution volume = 40 mL, and reaction time = 4 h.

Next, **Figure 5-18** shows that when Fe/TNTs@AC was repeatedly used in six consecutive cycles of adsorption-photodegradation without chemical regeneration, namely, the efficient photodegradation of pre-concentrated PFOA also regenerates the material. PFOA adsorption remained high (>99% removal), and the defluorination rate kept at ~60%. Evidently, Fe/TNTs@AC can be reused in multiple cycles without additional regeneration need. This important feature represents a great advancement of conventional adsorbents (AC or ion exchange resins), which require costly regeneration and subsequent treatment of the spent regenerant wastes. The slight increase in defluorination with the cycle time is attributed to the additional defluorination of intermediate products from the previous cycles. Indeed, short-chain PFAS were detected on Fe/TNTs@AC during the photodegradation process.
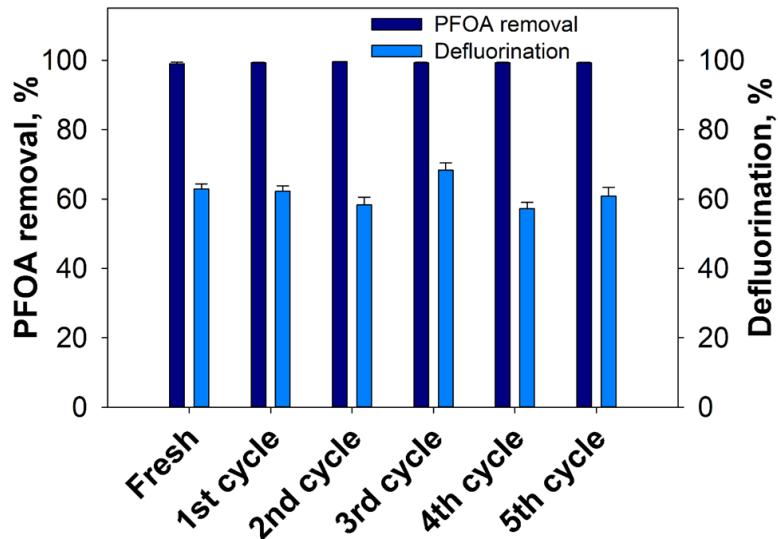
Figure 5-18. Reusability test of Fe/TNTs@AC. Experimental conditions: For each cycle, initial [PFOA] = 100 μg/L, material dosage = 1.0 g/L, solution volume = 40 mL, pH = 7.0 ± 0.3, adsorption time = 2 h, and photo-regeneration time = 4 h.

5.3.5. Photocatalytic degradation mechanisms of PFOA

To scrutinize the roles of ROS, *i.e.*, h^+, $^{\bullet}OH$, and $O_2^{\bullet-}$, in PFOA photodegradation, the classical scavenger quenching experiments (Li et al., 2018) were performed as shown in **Figure 5-19.** In this experiment, PFOA (100 µg/L) was pre-loaded on calcined Fe/TNTs@AC with >99% removal, followed by photodegradation in the presence of scavengers. The addition of KI, a scavenger for both h^+ and $^{\bullet}OH$ ($k \geq 1.1 \times 10^{10}\ M^{-1}\ s^{-1}$) (Buxton et al., 1988), inhibited PFOA defluorination efficiency from 62% to 51% (0.1mM KI) and 28% (1mM KI) at neutral pH. Yet, presence of isoproponal (IP, scavenger for $^{\bullet}OH$, $k = 1.9 \times 10^9\ M^{-1}\ s^{-1}$)(Buxton et al., 1988) only resulted in inhibition (62% vs. 51%) on PFOA defluorination. If substracting the $^{\bullet}OH$ contribution to PFOA inhibition in the preence of KI, h^+-driven reactions seem to be the most crucial mechanism for PFOA photodegradation in this study. Meanwhile, the addition of 0.1 or 1 mM benzoquinone (BQ; scavenger for $O_2^{\bullet-}$, $k = 3.7 \times 10^6\ M^{-1}\ s^{-1}$) (Sawada et al., 1975) also exhibited negligible influence to PFOA photodegradation. Results of the scavenger tests are consistent with previous observations that h^+ play a dominant role in various photocatalysis systems for PFOA oxidative photodegradation, rather than $^{\bullet}OH$ and $O_2^{\bullet-}$ (Li et al., 2013; Vecitis et al., 2009).
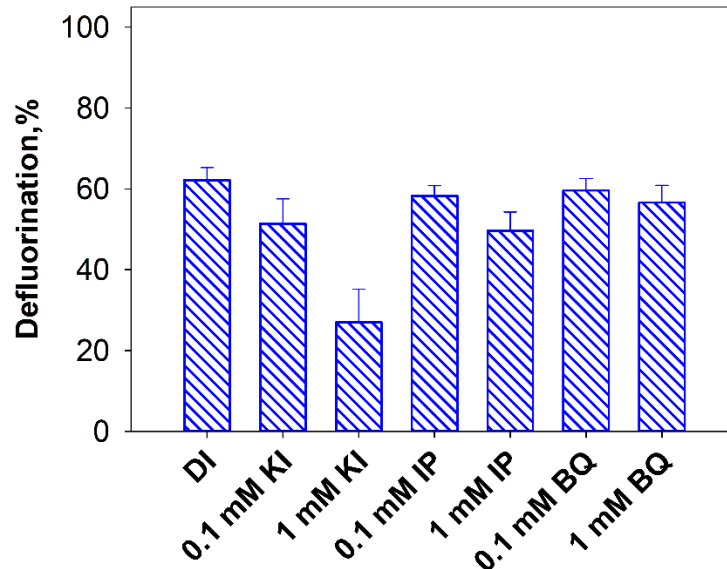
Figure 5-19. Classical scavenger quenching test of PFOA defluorination. Experimental conditions: Initial [PFOA] = 100 μg/L, material dosage = 1.0 g/L, solution volume = 40 mL, pH = 7.0 ± 0.3, isopropanol (IP), KI, and benzoquinone (BQ) concentration = 0.1 or 1 mM, and reaction time = 4 h.

Figure 5-20 shows a LC-QTOF-MS chromatogram displaying the intermediate products during the photodegradation of PFOA Fe/TNTs@AC. The peaks at the m/z values of 413, 363, 313, 263, 213, 163, and 113 were assigned to PFOA and various shorter chain PFCAs, including PFHpA, PFHxA, PFPeA, PFBA, PFPA, and TFA anions, respectively. In addition, the degradation products (daughter ion) of PFOA, namely PFHpA, PFHxA, PFPeA, PFBA, and PFPA were also identified at 369, 319, 269, 219, 169, and 119, respectively. This observation suggests that the PFOA degradation proceeds in the stepwise chain-shortening manner, which has been reported for conventional Ti- or anatase-based photocatalysts, and is consistent with observations by Tang et al. (2012) and Chen et al. (2007) (Jing et al., 2007; Tang et al., 2012).
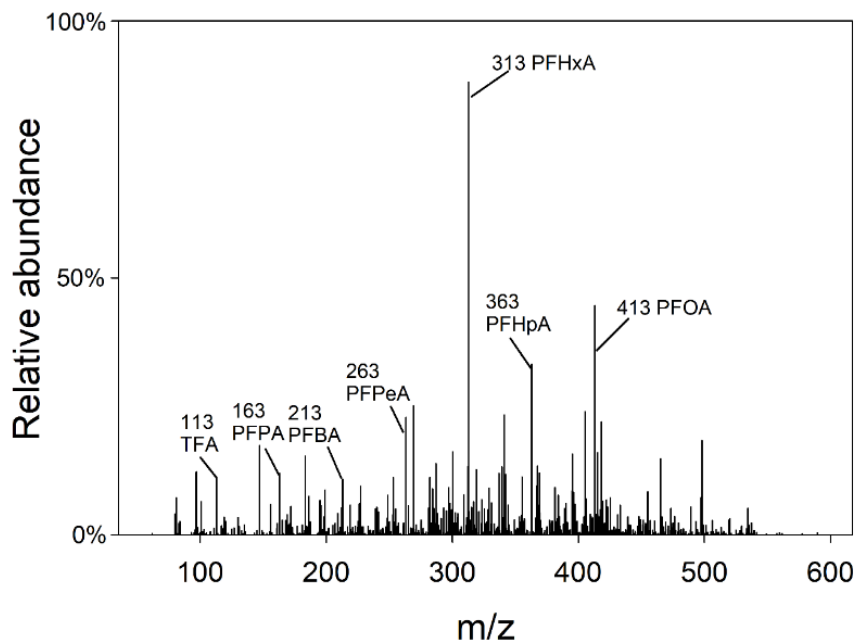
Figure 5-20. A LC-QTOF-MS chromatogram showing intermediate products during photodegradation of PFOA by Fe/TNTs@AC. Experimental conditions: Initial [PFOA] for adsorption = 1 mg/L (>95% PFOA was adsorbed), material dosage = 2.0 g/L, solution volume = 40 mL, pH = 7.0 ± 0.3, temperature = 23 ± 1 °C, and UV (λ=254 nm, 2.28 mW cm-2) irradiation time = 2 h.

Based on the latest theory for standard Ti-based materials (Panchangam et al., 2018; Peng et al., 2017) and the observed intermediates, the PFOA photodegradation by Fe/TNTs@AC proceeds through the following stepwise defluorination process:

$$CF_3(CF_2)_6COO^- + \equiv FeOH_2^+ \rightarrow CF_3(CF_2)_6COO^-\equiv FeOH_2^+ \tag{9}$$

$$TNTs + h\nu \rightarrow h^+ (VB) + e^- (CB) \tag{10}$$

$$CF_3(CF_2)_6COO^- + h^+ (VB) \rightarrow C_7F_{15}COO^\bullet \tag{11}$$

$$C_7F_{15}COO^\bullet \rightarrow {}^\bullet C_7F_{15} + CO_2 \tag{12}$$

$${}^\bullet C_7F_{15} + {}^\bullet OH \rightarrow C_7F_{15}OH \text{ or } {}^\bullet C_7F_{15} + H_2O \rightarrow C_7F_{15}OH + H^+ \tag{13}$$

$$C_7F_{15}OH \rightarrow C_6F_{13}COF + H^+ + F^- \tag{14}$$

$$C_6F_{13}COF + {}^{\bullet}OH \rightarrow C_6F_{13}COO^- + H^+ + F^- \tag{15}$$
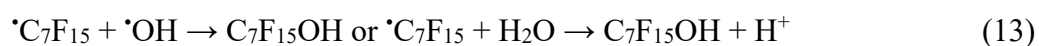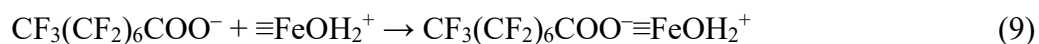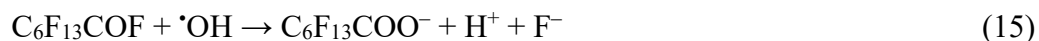
First, PFOA anions are adsorbed the impregnated iron (hydr)oxide nanoparticles through concurrent electrostatic and Lewis avid-base interactions (Eq. 9). Second, the adsorbed PFOA is oxidized by the photo-generated holes (h^+) (Eqs. 10-11) to form the unstable perfluoroalkyl radical ($C_7F_{15}COO^{\bullet}$), which decomposes into ${}^{\bullet}C_7F_{15}$ through a photo-Kolbe-like decarboxylation reaction with the head (COO^-) group cleaved (Eq. 12). The resulting ${}^{\bullet}C_7F_{15}$ radicals are further decomposed via reactions with OH• radicals and hydrolysis reaction (Eq. 13). The resulting $C_7F_{15}OH$ is highly unstable, leading to the cleavage of a C-F bond and release of one fluoride ion (Eq. 14). The intermediate product $C_6F_{13}COF$ is easily attacked by •OH radicals, which are produced abundantly by Fe/TNTs@AC, resulting in the shorter-chain PFCA (Eq. 15). The shorter-chain product $C_6F_{13}COO^-$ undergoes the same decarboxylation/defluorination cycle, each of which eliminating one carbon and two fluorine atoms (CF_2).

It should be noted that because the reaction starts with the head group decarboxylation, the introduction of iron plays a critical role as it can attract the head groups of PFOA to the vicinity of the photoactive sites, rendering the subsequent photodegradation much more favorable.

Natural bond orbital (NBO) analysis was further conducted to evaluate the active sites on PFOA (**Figure 5-21**). **Figure 5-21b** shows the ESP distribution on PFOA molecule. The reactive species (h^+, •OH and •O_2^-) in this system are all electron-deficient species and electrophilic reagents (Cai et al., 2019), which tends to attack the sites possessing more negative ESP. It is obvious that the carboxyl group of PFOA is more reactive. More accurate Fukui index indicating

electrophilic attack (f^-) based on DFT calculation was obtained. The O9 and O10 sites with the highest f^- values (0.420 and 0.407) preferred to be attacked by electrophilic species, which is consistent with the pathways determined through LC-QTOF-MS analysis (Eqs. 9-11). h^+ would attack on O10 site and oxidize PFOA anion to PFOA radical (Eq. 12), and further radicals attacking leaded to extrusion of CO_2 and formation of short-chain perfluorinated compounds. The electrophilic degradation pathway was widely reported by previous studies (Huang et al., 2016; Lin et al., 2012; Trojanowicz et al., 2018).

(c) Atom	No.	Charge (-1) (e/Å³)	Charge (-1) (e/Å³)	Charge (-1) (e/Å³)	f^+	f^-	f^0
C	1	1.07961	1.07991	1.04823	0.03138	0.0003	0.01584
C	2	0.64814	0.64848	0.59517	0.05297	0.00034	0.026655
C	3	0.67723	0.67782	0.57696	0.10027	0.00059	0.05043
C	4	0.67977	0.68086	0.56169	0.11808	0.00109	0.059585
C	5	0.67751	0.67994	0.59509	0.08242	0.00243	0.042425
C	6	0.67608	0.68417	0.63201	0.04407	0.00809	0.02608
C	7	0.62135	0.65295	0.60624	0.01511	0.0316	0.023355
C	8	0.73316	0.74526	0.70106	0.0321	0.0121	0.0221
O	9	-0.786	-0.36622	-0.80213	0.01613	0.41978	0.217955
O	10	-0.77216	-0.36505	-0.8029	0.03074	0.40711	0.218925
F	11	-0.34362	-0.34286	-0.36808	0.02446	0.00076	0.01261
F	12	-0.34846	-0.34813	-0.36101	0.01255	0.00033	0.00644
F	13	-0.34117	-0.34027	-0.37488	0.03371	0.0009	0.017305
F	14	-0.34422	-0.34365	-0.37252	0.0283	0.00057	0.014435
F	15	-0.34375	-0.34145	-0.39547	0.05172	0.0023	0.02701
F	16	-0.34413	-0.34086	-0.39607	0.05194	0.00327	0.027605
F	17	-0.34329	-0.34209	-0.39066	0.04737	0.0012	0.024285
F	18	-0.34584	-0.34076	-0.38756	0.04172	0.00508	0.0234
F	19	-0.36846	-0.33324	-0.38377	0.01531	0.03522	0.025265
F	20	-0.35216	-0.33993	-0.37902	0.02686	0.01223	0.019545
F	21	-0.35411	-0.34194	-0.38029	0.02618	0.01217	0.019175
F	22	-0.34487	-0.34455	-0.36222	0.01735	0.00032	0.008835
F	23	-0.34347	-0.34186	-0.39003	0.04656	0.00161	0.024085
F	24	-0.34711	-0.34077	-0.38709	0.03998	0.00634	0.02316
F	25	-0.37003	-0.33577	-0.38275	0.01272	0.03426	0.02349

Figure 5-21. NBO analysis for PFOA molecule at B3LYP/6-31+G (d,p) level. (a) Chemical structure of PFOA; (b) ESP mapped molecular surface of PFOA; and (3) Condensed Fukui index distribution of active sites on PFOA.

In addition to the anatase-facilitated photodegradation mechanism, Fe/TNTs@AC offers an additional degradation pathway thanks to the impregnation of iron (hydr)oxide as depicted by Eqs. (16)-(22). The holes generated from photo-activation of iron oxide can directly oxidize

PFOA, resulting in the $CF_3(CF_2)_5CF_2\bullet$ radical upon decarboxylation. In addition, the redox

reactions between Fe(III) and photo-generated holes/electrons also facilitate production of •OH

radicals and prevent electron-hole recombination, leading to much enhanced photodegradation

effectiveness.

$$CF_3(CF_2)_6COO^-\equiv Fe(OH)_2^+ + hv \rightarrow CF_3(CF_2)_5CF_2^\bullet + CO_2 + FeOH_2 \tag{16}$$

$$\equiv Fe(OH)_2 + h^+ \rightarrow \equiv Fe(OH)_2^+ \tag{17}$$

$$\equiv Fe(OH)_2 + O_2 \rightarrow \equiv Fe(OH)_2^+ + O_2^{\bullet-} \tag{18}$$

$$Fe^{3+} + h^+ \rightarrow Fe^{4+} \tag{19}$$

$$Fe^{4+} + OH^- \rightarrow Fe^{3+} + {}^\bullet OH \tag{20}$$

$$Fe^{3+} + e^- \rightarrow Fe^{2+} \tag{21}$$

$$Fe^{2+} + O_2 \rightarrow Fe^{3+} \tag{22}$$
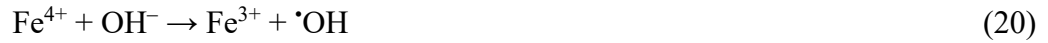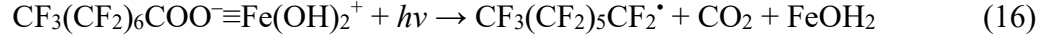
Earlier, Birben et al. (2017) (Birben et al., 2017) reporeted that Fe(III) can react with photo-

generated holes (h^+) to form Fe(IV), which can further react with hydroxide under alkaline

condition, producing Fe(III) and hydroxyl radicals (Eqs. 19-20) and this observation is agreed by

other researchers (Huo et al., 2011; Quici et al., 2007; Waite, 2005). Meanwhile, Fe(III) can react

with photo-generated electrons to form Fe(II) (Eq. 21), which can be further regenerated to

Fe(III) (Eq. 22). This Fe cycle plays an important role in facilitating the PFOA photodegradation.

Yet, the Fe concentration needs to be well controlled. If the concentration of Fe is too high,

Fe(III) may act as recombination centers through quantum tunneling (Zhang et al., 1998; Zhou et

al., 2005), resulting in reduced photo-activity; if the concentration is too low, the role of Fe may

not be fully utilized. Since the photodegradation of PFOA took place at neutral pH, dissolved O_2, rather than the hydroxyl radicals (which requires alkaline condition) should be the major oxidizing agent facilitating the Fe(III)-Fe(II) cycle (Yu et al., 2006; Zhou et al., 2006, 2005).

Overall, the enhanced adsorption and photodegradation are attributed to: 1) the carbon nanoparticles facilitate hydrophobic interactions with the PFOA tail, 2) the carbon coating also facilitates electron transfer and prevents electron-hole recombination in the photocatalyst, 3) the Fe(III) coating suppresses surface negative potential and enhances the interactions between the holes and the PFOA head groups (carboxylate), 4) the presence of Fe(III) also facilitates a series of redox reactions that facilitate production of •OH radicals and prevent e-h recombination, and 5) because of the lower band energy gap of iron oxide, the Fe-doping enhances absorption of more visible light.

5.4. Conclusion and environmental implication

In the present study, a novel adsorptive photocatalyst, Fe/TNTs@AC, was synthesized through a facile alkaline hydrothermal method follow by calcination. The composite materials exhibited excellent photocatalytic activity for degradation of PFOA under UV light, due to the following factors: 1) the supporting activated carbon (F-400), particularly the "micro carbon", played a dominant role in concentrating PFOA onto the surface of Fe/TNTs@AC via hydrophobic interaction, albeit Fe content could shift pH_{PZC} to neutral; 2) "parallel adsorption" as a prevalent adsorption manner for PFOA could occur, shortening the distance between the photogenerated h^+ (rather than $^{\bullet}OH$) and PFOA for improved oxidative photodegradation; and 3) the h^+ can withdraw an electron from carboxylate head group of PFOA to initiate the PFOA

photodegradation and further produce shorter chain perfluoroalkyl carboxylic acid till complete mineralization. Meanwhile, the stable performance of Fe/TNTs@AC in a wide pH range and excellent reusability at neutral pH allow a possible implementation of "concentrate-and-degradation" approach with this novel composite material. Such "concentrate-and-degradation" concept, yet being under development, has shown promising feasibility in scale-up water treatment processes.

Given the excellent adsorption and photodegradation performance, our novel composite material could be used to remove short-chain PFAS which are more mobile and more resistant to be photodegraded. Still, there are some critical issues that need to be addressed for the Fe/TNTs@AC-based treatment, such as effects of dissolved organic matter (DOM), inorganic cations (*e.g.*, Mg^{2+}, Cu^{2+}, Ca^{2+}, Al^{3+}, and Fe^{3+}), co-solutes (*e.g.*, competitive persistent organic pollutants), ionic strength, and *etc.* For instant, a low level of DOM may act as natural sensitizer which can enhance PFOA photodegradation, while high concentration DOM would compete for photocatalytic sites and inhibit PFOA photodegradation.(Vaalgamaa et al., 2011) In addition, suitable engineering design of the Fe/TNTs@AC-based treatment process are desired before seeing full-scale application of the technology. Further, economic assessment should be conducted to verify the "concentrate-and-degradation" approach is more cost-effective and eco-friendly than the conventional treatment technologies (i.e. AC/resin adsorption-regeneration approach).

Future Work

Based on the findings, I anticipate that the new technology will potentially equip the remedial project with a powerful on-site treatment approach in treating PFAS at hundreds of polluted sites. To this end, the following follow-on research activities are warranted:

- ✓ The adsorptive photocatalysts can be further optimized in terms of selectivity for PFAS and photoactivity by tuning the parent materials, the dopants, and synthesis conditions towards more efficient mineralization of PFAS, especially for PFAS in soil extracts;

- ✓ Composite materials that are more reactive under solar light should be further explored;

- ✓ Further investigations are needed to test the effectiveness under DoD field water/soil conditions to identify potential inhibitions of the water matrix and find out ways to overcome these inhibitive effects and to optimize the water chemistry conditions;

- ✓ Pilot-scale experiments should be carried out to facilitate more realistic assessment of the technical and economic effectiveness and to guide field application design;

- ✓ Desorption of PFAS from soil can be further optimized by adjusting the solution recipe and chemistry to facilitate more efficient desorption of PFAS and to promote subsequent photodegradation;

- ✓ Water chemistry conditions can be optimized to promote photocatalytic degradation of more persistent PFAS or PFAS from the dispersant solutions, including addition of proper photosensitizers and elevation of reaction temperature; and

- ✓ To promote earliest possible field adoption, various technology transition/transfer measures should be taken immediately following the pilot-testing, first towards the DoD

end users, and then the market at large (e.g., landfill leachate and groundwater sites).

References:

Bahnemann, D.W., Hilgendorff, M., Memming, R., 1997. Charge carrier dynamics at TiO2 particles: reactivity of free and trapped holes. The Journal of Physical Chemistry B 101, 4265–4275.

Beltran, F.J., 2003. Ozone reaction kinetics for water and wastewater systems. crc Press.

Bentel, M.J., Yu, Y., Xu, L., Li, Z., Wong, B.M., Men, Y., Liu, J., 2019. Defluorination of Per-and Polyfluoroalkyl Substances (PFASs) with Hydrated Electrons: Structural Dependence and Implications to PFAS Remediation and Management. Environmental science & technology.

Birben, N.C., Uyguner-Demirel, C.S., Kavurmaci, S.S., Gürkan, Y.Y., Turkten, N., Cinar, Z., Bekbolet, M., 2017. Application of Fe-doped TiO2 specimens for the solar photocatalytic degradation of humic acid. Catalysis Today 281, 78–84.

Breeuwsma, A., Lyklema, J., 1973. Physical and chemical adsorption of ions in the electrical double layer on hematite (α-Fe2O3). Journal of Colloid and Interface Science 43, 437–448.

Burns, D.C., Ellis, D.A., Li, H., McMurdo, C.J., Webster, E., 2008. Experimental p K a determination for perfluorooctanoic acid (PFOA) and the potential impact of p K a concentration dependence on laboratory-measured partitioning phenomena and environmental modeling. Environmental science & technology 42, 9283–9288.

Buxton, G.V., Greenstock, C.L., Helman, W.P., Ross, A.B., 1988. Critical review of rate constants for reactions of hydrated electrons, hydrogen atoms and hydroxyl radicals ($\cdot$ OH/$\cdot$ O- in aqueous solution. Journal of physical and chemical reference data 17, 513–886.

Cai, Z., Hao, X., Sun, X., Du, P., Liu, W., Fu, J., 2019. Highly active WO3@anatase-SiO2 aerogel for solar-light-driven phenanthrene degradation: Mechanism insight and toxicity assessment. Water Research 162, 369–382. https://doi.org/10.1016/j.watres.2019.06.017

Chen, M.-J., Lo, S.-L., Lee, Y.-C., Huang, C.-C., 2015. Photocatalytic decomposition of perfluorooctanoic acid by transition-metal modified titanium dioxide. Journal of hazardous materials 288, 168–175.

Chen, Q., Zhou, W., Du, G.H., Peng, L., 2002. Trititanate nanotubes made via a single alkali treatment. Advanced materials 14, 1208–1211.

Cho, I.-H., 2011. Degradation and reduction of acute toxicity of environmentally persistent perfluorooctanoic acid (PFOA) using VUV photolysis and TiO2 photocatalysis in acidic and basic aqueous solutions. Toxicological & Environmental Chemistry 93, 925–940.

Deng, S., Yu, Q., Huang, J., Yu, G., 2010. Removal of perfluorooctane sulfonate from wastewater by anion exchange resins: effects of resin properties and solution chemistry. Water Research 44, 5188–5195.

Deng, S., Zhang, Q., Nie, Y., Wei, H., Wang, B., Huang, J., Yu, G., Xing, B., 2012. Sorption mechanisms of perfluorinated compounds on carbon nanotubes. Environmental pollution 168, 138–144.

Dillert, R., Bahnemann, D., Hidaka, H., 2007. Light-induced degradation of perfluorocarboxylic acids in the presence of titanium dioxide. Chemosphere 67, 785–792.

Dudley, L.-A., 2012. Removal of Perfluorinated Compounds by Powdered Activated Carbon,

Superfine Powder Activated Carbon, and Anion Exchange Resin.

Estrellan, C.R., Salim, C., Hinode, H., 2010. Photocatalytic decomposition of perfluorooctanoic acid by iron and niobium co-doped titanium dioxide. Journal of hazardous materials 179, 79–83.

Foo, K.Y., Hameed, B.H., 2010. Insights into the modeling of adsorption isotherm systems. Chemical engineering journal 156, 2–10.

Frisch, M.J., Trucks, G.W., Schlegel, H.B., Scuseria, G.E., Robb, M.A., Cheeseman, J.R., Montgomery Jr, J.A., Vreven, T., Kudin, K.N., Burant, J.C., 2004. Gaussian 03, Revision C. 02 2003. There is no corresponding record for this reference.

Gu, Y., Yperman, J., Carleer, R., D'Haen, J., Maggen, J., Vanderheyden, S., Vanreppelen, K., Garcia, R.M., 2019. Adsorption and photocatalytic removal of Ibuprofen by activated carbon impregnated with TiO2 by UV–Vis monitoring. Chemosphere 217, 724–731.

Han, B., Zhang, M., Zhao, D., Feng, Y., 2015. Degradation of aqueous and soil-sorbed estradiol using a new class of stabilized manganese oxide nanoparticles. Water research 70, 288–299.

Higgins, C.P., Luthy, R.G., 2006. Sorption of perfluorinated surfactants on sediments. Environmental Science & Technology 40, 7251–7256.

Ho, Y.-S., McKay, G., 1999. Pseudo-second order model for sorption processes. Process biochemistry 34, 451–465.

Hu, X.C., Andrews, D.Q., Lindstrom, A.B., Bruton, T.A., Schaider, L.A., Grandjean, P., Lohmann, R., Carignan, C.C., Blum, A., Balan, S.A., 2016. Detection of poly-and perfluoroalkyl substances (PFASs) in US drinking water linked to industrial sites, military fire training areas, and wastewater treatment plants. Environmental science & technology letters 3, 344–350.

Huang, J., Wang, X., Pan, Z., Li, X., Ling, Y., Li, L., 2016. Efficient degradation of perfluorooctanoic acid (PFOA) by photocatalytic ozonation. Chemical Engineering Journal 296, 329–334.

Huo, P., Lu, Z., Wang, H., Pan, J., Li, H., Wu, X., Huang, W., Yan, Y., 2011. Enhanced photodegradation of antibiotics solution under visible light with Fe2+/Fe3+ immobilized on TiO2/fly-ash cenospheres by using ions imprinting technology. Chemical engineering journal 172, 615–622.

Jing, C., ZHANG, P., Jian, L.I.U., 2007. Photodegradation of perfluorooctanoic acid by 185 nm vacuum ultraviolet light. Journal of Environmental Sciences 19, 387–390.

Krusic, P.J., Marchione, A.A., Roe, D.C., 2005. Gas-phase NMR studies of the thermolysis of perfluorooctanoic acid. Journal of fluorine chemistry 126, 1510–1516.

Land, M., de Wit, C.A., Bignert, A., Cousins, I.T., Herzke, D., Johansson, J.H., Martin, J.W., 2018. What is the effect of phasing out long-chain per-and polyfluoroalkyl substances on the concentrations of perfluoroalkyl acids and their precursors in the environment? A systematic review. Environmental Evidence 7, 4.

Lawless, D., Serpone, N., Meisel, D., 1991. Role of hydroxyl radicals and trapped holes in photocatalysis. A pulse radiolysis study. The Journal of Physical Chemistry 95, 5166–5170.

Le, H.A., Chin, S., Jurng, J., 2012. Photocatalytic degradation of methylene blue by a combination of TiO2-anatase and coconut shell activated carbon. Powder Technology 225, 167–175.

Legrini, O., Oliveros, E., Braun, A.M., 1993. Photochemical processes for water treatment. Chemical reviews 93, 671–698.

Li, F., Du, P., Liu, W., Li, X., Ji, H., Duan, J., Zhao, D., 2018. Hydrothermal synthesis of graphene grafted titania/titanate nanosheets for photocatalytic degradation of 4-chlorophenol: Solar-light-driven photocatalytic activity and computational chemistry analysis. Chemical Engineering Journal 331, 685–694.

Li, F., Duan, J., Tian, S., Ji, H., Zhu, Y., Wei, Z., Zhao, D., 2019. Short-chain Per-and Polyfluoroalkyl Substances in Aquatic Systems: Occurrence, Impacts and Treatment. Chemical Engineering Journal 122506.

Li, M., Yu, Z., Liu, Q., Sun, L., Huang, W., 2016. Photocatalytic decomposition of perfluorooctanoic acid by noble metallic nanoparticles modified TiO2. Chemical Engineering Journal 286, 232–238.

Li, Z., Zhang, P., Shao, T., Li, X., 2012. In2O3 nanoporous nanosphere: a highly efficient photocatalyst for decomposition of perfluorooctanoic acid. Applied Catalysis B: Environmental 125, 350–357.

Li, Z., Zhang, P., Shao, T., Wang, J., Jin, L., Li, X., 2013. Different nanostructured In2O3 for photocatalytic decomposition of perfluorooctanoic acid (PFOA). Journal of hazardous materials 260, 40–46.

Lin, H., Niu, J., Ding, S., Zhang, L., 2012. Electrochemical degradation of perfluorooctanoic acid (PFOA) by Ti/SnO2–Sb, Ti/SnO2–Sb/PbO2 and Ti/SnO2–Sb/MnO2 anodes. Water research 46, 2281–2289.

Lin, J.-C., Hu, C.-Y., Lo, S.-L., 2016. Effect of surfactants on the degradation of perfluorooctanoic acid (PFOA) by ultrasonic (US) treatment. Ultrasonics sonochemistry 28, 130–135.

Liu, K., Zhang, S., Hu, X., Zhang, K., Roy, A., Yu, G., 2015. Understanding the adsorption of PFOA on MI/L01 (Cr)-based anionic-exchange metal–organic frameworks: comparing DFT calculations with aqueous sorption experiments. Environmental science & technology 49, 8657–8665.

Liu, W., Cai, Z., Zhao, X., Wang, T., Li, F., Zhao, D., 2016a. High-capacity and photoregenerable composite material for efficient adsorption and degradation of phenanthrene in water. Environmental science & technology 50, 11174–11183.

Liu, W., Sun, W., Borthwick, A.G., Wang, T., Li, F., Guan, Y., 2016b. Simultaneous removal of Cr (VI) and 4-chlorophenol through photocatalysis by a novel anatase/titanate nanosheet composite: synergetic promotion effect and autosynchronous doping. Journal of hazardous materials 317, 385–393.

Liu, W., Wang, T., Borthwick, A.G., Wang, Y., Yin, X., Li, X., Ni, J., 2013. Adsorption of Pb2+, Cd2+, Cu2+ and Cr3+ onto titanate nanotubes: competition and effect of inorganic ions. Science of the Total Environment 456, 171–180.

Ma, J., Li, F., Qian, T., Liu, H., Liu, W., Zhao, D., 2017. Natural organic matter resistant powder activated charcoal supported titanate nanotubes for adsorption of Pb (II). Chemical Engineering Journal 315, 191–200.

Mao, Y., Wong, S.S., 2006. Size-and shape-dependent transformation of nanosized titanate into

analogous anatase titania nanostructures. Journal of the American Chemical Society 128, 8217–8226.

Ochoa-Herrera, V., Sierra-Alvarez, R., 2008. Removal of perfluorinated surfactants by sorption onto granular activated carbon, zeolite and sludge. Chemosphere 72, 1588–1593.

Oláh, J., Van Alsenoy, C., Sannigrahi, A.B., 2002. Condensed Fukui functions derived from stockholder charges: assessment of their performance as local reactivity descriptors. The Journal of Physical Chemistry A 106, 3885–3890.

Panchangam, S.C., Yellatur, C.S., Yang, J.-S., Loka, S.S., Lin, A.Y.C., Vemula, V., 2018. Facile fabrication of TiO2-graphene nanocomposites (TGNCs) for the efficient photocatalytic oxidation of perfluorooctanoic acid (PFOA). Journal of Environmental Chemical Engineering 6, 6359–6369.

Parr, R.G., Yang, W., 1984. Density functional approach to the frontier-electron theory of chemical reactivity. Journal of the American Chemical Society 106, 4049–4050.

Peng, Y.-P., Chen, H., Huang, C., 2017. The synergistic effect of photoelectrochemical (PEC) reactions exemplified by concurrent perfluorooctanoic acid (PFOA) degradation and hydrogen generation over carbon and nitrogen codoped TiO2 nanotube arrays (CN-TNTAs) photoelectrode. Applied Catalysis B: Environmental 209, 437–446.

Quici, N., Morgada, M.E., Gettar, R.T., Bolte, M., Litter, M.I., 2007. Photocatalytic degradation of citric acid under different conditions: TiO2 heterogeneous photocatalysis against homogeneous photolytic processes promoted by Fe (III) and H2O2. Applied Catalysis B: Environmental 71, 117–124.

Quiñones, D.H., Rey, A., Álvarez, P.M., Beltrán, F.J., Plucinski, P.K., 2014. Enhanced activity and reusability of TiO2 loaded magnetic activated carbon for solar photocatalytic ozonation. Applied Catalysis B: Environmental 144, 96–106.

Radi, R., Beckman, J.S., Bush, K.M., Freeman, B.A., 1991. Peroxynitrite oxidation of sulfhydryls. The cytotoxic potential of superoxide and nitric oxide. Journal of Biological Chemistry 266, 4244–4250.

Rey, A., Quinones, D.H., Álvarez, P.M., Beltrán, F.J., Plucinski, P.K., 2012. Simulated solar-light assisted photocatalytic ozonation of metoprolol over titania-coated magnetic activated carbon. Applied Catalysis B: Environmental 111, 246–253.

Sahu, S.P., Qanbarzadeh, M., Ateia, M., Torkzadeh, H., Maroli, A.S., Cates, E.L., 2018. Rapid Degradation and Mineralization of Perfluorooctanoic Acid by a New Petitjeanite Bi3O(OH)(PO4)2 Microparticle Ultraviolet Photocatalyst. Environ. Sci. Technol. Lett. 5, 533–538. https://doi.org/10.1021/acs.estlett.8b00395

Sawada, Y., Iyanagi, T., Yamazaki, I., 1975. Relation between redox potentials and rate constants in reactions coupled with the system oxygen-superoxide. Biochemistry 14, 3761–3764.

Schwarz, H., Dodson, R., 1984. Equilibrium between hydroxyl radicals and thallium (II) and the oxidation potential of hydroxyl (aq). The Journal of Physical Chemistry 88, 3643–3647.

Sivula, K., Le Formal, F., Grätzel, M., 2011. Solar water splitting: progress using hematite (α-Fe2O3) photoelectrodes. ChemSusChem 4, 432–449.

Song, C., Chen, P., Wang, C., Zhu, L., 2012. Photodegradation of perfluorooctanoic acid by

synthesized TiO2–MWCNT composites under 365 nm UV irradiation. Chemosphere 86, 853–859.

Sun, X., Li, Y., 2003. Synthesis and characterization of ion-exchangeable titanate nanotubes. Chemistry–A European Journal 9, 2229–2238.

Tang, H., Xiang, Q., Lei, M., Yan, J., Zhu, L., Zou, J., 2012. Efficient degradation of perfluorooctanoic acid by UV–Fenton process. Chemical Engineering Journal 184, 156–162.

Trojanowicz, M., Bojanowska-Czajka, A., Bartosiewicz, I., Kulisa, K., 2018. Advanced Oxidation/Reduction Processes treatment for aqueous perfluorooctanoate (PFOA) and perfluorooctanesulfonate (PFOS)–A review of recent advances. Chemical Engineering Journal 336, 170–199.

Vaalgamaa, S., Vähätalo, A.V., Perkola, N., Huhtala, S., 2011. Photochemical reactivity of perfluorooctanoic acid (PFOA) in conditions representing surface water. Science of the total environment 409, 3043–3048.

Vecitis, C.D., Park, H., Cheng, J., Mader, B.T., Hoffmann, M.R., 2009. Treatment technologies for aqueous perfluorooctanesulfonate (PFOS) and perfluorooctanoate (PFOA). Frontiers of Environmental Science & Engineering in China 3, 129–151.

Waite, T.D., 2005. Role of iron in light-induced environmental processes, in: Environmental Photochemistry Part II. Springer, pp. 255–298.

Wang, Y., Niu, J., Li, Y., Zheng, T., Xu, Y., Liu, Y., 2015. Performance and mechanisms for removal of perfluorooctanoate (PFOA) from aqueous solution by activated carbon fiber. RSC Advances 5, 86927–86933.

Weber, W.J., 2001. Environmental systems and processes: principles, modeling, and design. Wiley-Interscience New York.

Wei, Z., Luo, S., Xiao, R., Khalfin, R., Semiat, R., 2017a. Characterization and quantification of chromate adsorption by layered porous iron oxyhydroxide: An experimental and theoretical study. Journal of hazardous materials 338, 472–481.

Wei, Z., Villamena, F.A., Weavers, L.K., 2017b. Kinetics and mechanism of ultrasonic activation of persulfate: an in situ EPR spin trapping study. Environmental Science & Technology 51, 3410–3417.

Wu, H., Wu, G., Wang, L., 2015. Peculiar porous α-Fe2O3, γ-Fe2O3 and Fe3O4 nanospheres: facile synthesis and electromagnetic properties. Powder technology 269, 443–451.

Yang, B., Jiang, C., Yu, G., Zhuo, Q., Deng, S., Wu, J., Zhang, H., 2015. Highly efficient electrochemical degradation of perfluorooctanoic acid (PFOA) by F-doped Ti/SnO2 electrode. Journal of hazardous materials 299, 417–424.

Yang, H.G., Sun, C.H., Qiao, S.Z., Zou, J., Liu, G., Smith, S.C., Cheng, H.M., Lu, G.Q., 2008. Anatase TiO 2 single crystals with a large percentage of reactive facets. Nature 453, 638.

Yoganarasimhan, S., Rao, C.R., 1962. Mechanism of crystal structure transformations. Part 3.—factors affecting the anatase-rutile transformation. Transactions of the Faraday Society 58, 1579–1589.

Yu, J., Yu, H., Ao, C., Lee, S., Jimmy, C.Y., Ho, W., 2006. Preparation, characterization and photocatalytic activity of in situ Fe-doped TiO2 thin films. Thin Solid Films 496, 273–280.

Zhang, X., Lei, L., 2008. Preparation of photocatalytic Fe2O3–TiO2 coatings in one step by metal organic chemical vapor deposition. Applied Surface Science 254, 2406–2412.

Zhang, Z., Wang, C.-C., Zakaria, R., Ying, J.Y., 1998. Role of particle size in nanocrystalline TiO2-based photocatalysts. The Journal of Physical Chemistry B 102, 10871–10878.

Zhao, D., Cheng, J., Vecitis, C.D., Hoffmann, M.R., 2011. Sorption of perfluorochemicals to granular activated carbon in the presence of ultrasound. The Journal of Physical Chemistry A 115, 2250–2257.

Zhou, M., Yu, J., Cheng, B., 2006. Effects of Fe-doping on the photocatalytic activity of mesoporous TiO2 powders prepared by an ultrasonic method. Journal of Hazardous Materials 137, 1838–1847.

Zhou, M., Yu, J., Cheng, B., Yu, H., 2005. Preparation and photocatalytic activity of Fe-doped mesoporous titanium dioxide nanocrystalline photocatalysts. Materials Chemistry and Physics 93, 159–163.

Ai, Z., Yang, P., Lu, X., 2005. Degradation of 4-chlorophenol by a microwave assisted photocatalysis method. Journal of hazardous materials 124, 147–152.

Bavykin, D.V., Friedrich, J.M., Walsh, F.C., 2006. Protonated titanates and TiO2 nanostructured materials: synthesis, properties, and applications. Advanced Materials 18, 2807–2824.

Chilom, G., Bruns, A.S., Rice, J.A., 2009. Aggregation of humic acid in solution: Contributions of different fractions. Organic Geochemistry 40, 455–460. https://doi.org/10.1016/j.orggeochem.2009.01.010

Dąbrowski, A., Podkościelny, P., Hubicki, Z., Barczak, M., 2005. Adsorption of phenolic compounds by activated carbon—a critical review. Chemosphere 58, 1049–1070. https://doi.org/10.1016/j.chemosphere.2004.09.067

Dionysiou, D.D., Khodadoust, A.P., Kern, A.M., Suidan, M.T., Baudin, I., Laîné, J.-M., 2000. Continuous-mode photocatalytic degradation of chlorinated phenols and pesticides in water using a bench-scale TiO2 rotating disk reactor. Applied Catalysis B: Environmental 24, 139–155.

Ho, Y.-S., McKay, G., 1999. Pseudo-second order model for sorption processes. Process biochemistry 34, 451–465.

Jones, K.C., De Voogt, P., 1999. Persistent organic pollutants (POPs): state of the science. Environmental pollution 100, 209–221.

Khuzwayo, Z., Chirwa, E.M.N., 2015. Modelling and simulation of photocatalytic oxidation mechanism of chlorohalogenated substituted phenols in batch systems: Langmuir–Hinshelwood approach. Journal of hazardous materials 300, 459–466.

Li, F., Du, P., Liu, W., Li, X., Ji, H., Duan, J., Zhao, D., 2018. Hydrothermal synthesis of graphene grafted titania/titanate nanosheets for photocatalytic degradation of 4-chlorophenol: Solar-light-driven photocatalytic activity and computational chemistry analysis. Chemical Engineering Journal 331, 685–694.

Libby, B., Monson, P.A., 2004. Adsorption/Desorption Hysteresis in Inkbottle Pores: A Density Functional Theory and Monte-Carlo Simulation Study. Langmuir 20, 4289–4294. https://doi.org/10.1021/la036100a

Lin, S.-H., Juang, R.-S., 2009. Adsorption of phenol and its derivatives from water using synthetic resins and low-cost natural adsorbents: A review. Journal of Environmental Management 90, 1336–1349. https://doi.org/10.1016/j.jenvman.2008.09.003

Liu, W., Cai, Z., Zhao, X., Wang, T., Li, F., Zhao, D., 2016a. High-capacity and photoregenerable composite material for efficient adsorption and degradation of phenanthrene in water. Environmental science & technology 50, 11174–11183.

Liu, W., Sun, W., Borthwick, A.G.L., Wang, T., Li, F., Guan, Y., 2016b. Simultaneous removal of Cr(VI) and 4-chlorophenol through photocatalysis by a novel anatase/titanate nanosheet composite: Synergetic promotion effect and autosynchronous doping. Journal of Hazardous Materials 317, 385–393. https://doi.org/10.1016/j.jhazmat.2016.06.002

Loeb, S.K., Alvarez, P.J.J., Brame, J.A., Cates, E.L., Choi, W., Crittenden, J., Dionysiou, D.D., Li, Q., Li-Puma, G., Quan, X., Sedlak, D.L., David Waite, T., Westerhoff, P., Kim, J.-H., 2019. The Technology Horizon for Photocatalytic Water Treatment: Sunrise or Sunset? Environ. Sci. Technol. 53, 2937–2947. https://doi.org/10.1021/acs.est.8b05041

Ou, H.-H., Lo, S.-L., 2007. Review of titania nanotubes synthesized via the hydrothermal treatment: Fabrication, modification, and application. Separation and Purification Technology 58, 179–191.

Pérez-Moya, M., Graells, M., del Valle, L.J., Centelles, E., Mansilla, H.D., 2007. Fenton and photo-Fenton degradation of 2-chlorophenol: Multivariate analysis and toxicity monitoring. Catalysis Today, Advanced Catalytic Oxidation Processes 124, 163–171. https://doi.org/10.1016/j.cattod.2007.03.034

Pi, Y., Zhang, L., Wang, J., 2007. The formation and influence of hydrogen peroxide during ozonation of para-chlorophenol. J. of Hazardous Materials 141, 707–712. https://doi.org/10.1016/j.jhazmat.2006.07.032

Pignatello, J.J., Kwon, S., Lu, Y., 2006. Effect of Natural Organic Substances on the Surface and Adsorptive Properties of Environmental Black Carbon (Char): Attenuation of Surface Activity by Humic and Fulvic Acids. Environ. Sci. Technol. 40, 7757–7763. https://doi.org/10.1021/es061307m

Slimen, H., Houas, A., Nogier, J.P., 2011. Elaboration of stable anatase TiO2 through activated carbon addition with high photocatalytic activity under visible light. Journal of Photochemistry and Photobiology A: Chemistry 221, 13–21. https://doi.org/10.1016/j.jphotochem.2011.04.013

Sorokin, A., Meunier, B., Séris, J.-L., 1995. Efficient oxidative dechlorination and aromatic ring cleavage of chlorinated phenols catalyzed by iron sulfophthalocyanine. Science 268, 1163–1166.

Sze, M.F.F., McKay, G., 2012. Enhanced mitigation of para-chlorophenol using stratified activated carbon adsorption columns. Water research 46, 700–710.

Takagahara, T., Takeda, K., 1992. Theory of the quantum confinement effect on excitons in quantum dots of indirect-gap materials. Phys. Rev. B 46, 15578–15581. https://doi.org/10.1103/PhysRevB.46.15578

Tuller, M., Or, D., Dudley, L.M., 1999. Adsorption and capillary condensation in porous media:

Liquid retention and interfacial configurations in angular pores. Water Resources Research 35, 1949–1964. https://doi.org/10.1029/1999WR900098

Wang, T., Liu, W., Xiong, L., Xu, N., Ni, J., 2013. Influence of pH, ionic strength and humic acid on competitive adsorption of Pb(II), Cd(II) and Cr(III) onto titanate nanotubes. Chemical Engineering Journal 215–216, 366–374. https://doi.org/10.1016/j.cej.2012.11.029

Wania, F., Mackay, D., 1996. Peer reviewed: tracking the distribution of persistent organic pollutants. Environmental science & technology 30, 390A–396A.

Xiong, L., Chen, C., Chen, Q., Ni, J., 2011. Adsorption of Pb(II) and Cd(II) from aqueous solutions using titanate nanotubes prepared via hydrothermal method. Journal of Hazardous Materials, Selected papers presented at the 2nd International Conference on Research Frontiers in Chalcogen Cycle Science and Technology, Delft, The Netherlands, May 31st-June 1st, 2010 189, 741–748. https://doi.org/10.1016/j.jhazmat.2011.03.006

Yang, K., Wu, W., Jing, Q., Jiang, W., Xing, B., 2010. Competitive Adsorption of Naphthalene with 2,4-Dichlorophenol and 4-Chloroaniline on Multiwalled Carbon Nanotubes. Environ. Sci. Technol. 44, 3021–3027. https://doi.org/10.1021/es100018a

Yin, X., Liu, W., Ni, J., 2014. Removal of coexisting Cr(VI) and 4-chlorophenol through reduction and Fenton reaction in a single system. Chemical Engineering Journal 248, 89–97. https://doi.org/10.1016/j.cej.2014.03.017

Zhang, Q., Chuang, K.T., 2001. Adsorption of organic pollutants from effluents of a Kraft pulp mill on activated carbon and polymer resin. Advances in Environmental Research 5, 251–258. https://doi.org/10.1016/S1093-0191(00)00059-9

Zhao, D., Hunter, M., Pignatello, J.J., White, J.C., 2002. Application of the dual-mode model for predicting competitive sorption equilibria and rates of polycyclic aromatic hydrocarbons in estuarine sediment suspensions. Environmental Toxicology and Chemistry 21, 2276–2282. https://doi.org/10.1002/etc.5620211104

Zhao, D., Pignatello, J.J., White, J.C., Braida, W., Ferrandino, F., 2001. Dual-mode modeling of competitive and concentration-dependent sorption and desorption kinetics of polycyclic aromatic hydrocarbons in soils. Water Resources Research 37, 2205–2212. https://doi.org/10.1029/2001WR000287

Kumar, S.G. and Devi, L.G. (2011) Review on modified TiO2 photocatalysis under UV/visible light: selected results and related mechanisms on interfacial charge carrier transfer dynamics. The Journal of Physical Chemistry A 115(46), 13211-13241.

Hashimoto, K., Irie, H. and Fujishima, A. (2005) TiO2 photocatalysis: a historical overview and future prospects. Japanese Journal Of Applied Physics 44(12R), 8269.

Schneider, J., Matsuoka, M., Takeuchi, M., Zhang, J., Horiuchi, Y., Anpo, M. and Bahnemann, D.W. (2014) Understanding TiO2 photocatalysis: mechanisms and materials. Chemical Reviews 114(19), 9919-9986.

Bavykin, D.V., Friedrich, J.M. and Walsh, F.C. (2006a) Protonated titanates and TiO2 nanostructured materials: synthesis, properties, and applications. Advanced Materials 18(21), 2807-2824.

Ou, H.-H. and Lo, S.-L. (2007) Review of titania nanotubes synthesized via the hydrothermal

treatment: fabrication, modification, and application. Separation And Purification Technology 58(1), 179-191.

Zhao, X., Cai, Z., Wang, T., O'Reilly, S., Liu, W. and Zhao, D. (2016) A new type of cobalt-deposited titanate nanotubes for enhanced photocatalytic degradation of phenanthrene. Applied Catalysis B: Environmental 187, 134-143.

Liu, W., Sun, W., Borthwick, A.G., Wang, T., Li, F. and Guan, Y. (2016a) Simultaneous removal of Cr (VI) and 4-chlorophenol through photocatalysis by a novel anatase/titanate nanosheet composite: Synergetic promotion effect and autosynchronous doping. Journal Of Hazardous Materials 317, 385-393.

Morales-Torres, S., Pastrana-Martínez, L.M., Figueiredo, J.L., Faria, J.L. and Silva, A.M. (2012) Design of graphene-based TiO2 photocatalysts—a review. Environmental Science And Pollution Research 19(9), 3676-3687.

Lee, J.S., You, K.H. and Park, C.B. (2012) Highly photoactive, low bandgap TiO2 nanoparticles wrapped by graphene. Advanced Materials 24(8), 1084-1088.

Pan, X., Zhao, Y., Liu, S., Korzeniewski, C.L., Wang, S. and Fan, Z. (2012) Comparing graphene-TiO2 nanowire and graphene-TiO2 nanoparticle composite photocatalysts. Acs Applied Materials & Interfaces 4(8), 3944-3950.

Perera, S.D., Mariano, R.G., Vu, K., Nour, N., Seitz, O., Chabal, Y. and Balkus Jr, K.J. (2012) Hydrothermal synthesis of graphene-TiO2 nanotube composites with enhanced photocatalytic activity. Acs Catalysis 2(6), 949-956.

Zhao, D., Sheng, G., Chen, C. and Wang, X. (2012) Enhanced photocatalytic degradation of methylene blue under visible irradiation on graphene@ TiO 2 dyade structure. Applied Catalysis B: Environmental 111, 303-308.

Liang, Y., Wang, H., Casalongue, H.S., Chen, Z. and Dai, H. (2010) TiO2 nanocrystals grown on graphene as advanced photocatalytic hybrid materials. Nano Research 3(10), 701-705.

Kasuga, T., Hiramatsu, M., Hoson, A., Sekino, T. and Niihara, K. (1999) Titania nanotubes prepared by chemical processing. Advanced Materials 11(15), 1307-1311.

Chen, Q., Zhou, W., Du, G. and Peng, L.-M. (2002) Trititanate nanotubes made via a single alkali treatment. Advanced Materials 14(17), 1208-1211.

Kim, I.Y., Park, S., Kim, H., Park, S., Ruoff, R.S. and Hwang, S.J. (2014a) Strongly-Coupled Freestanding Hybrid Films of Graphene and Layered Titanate Nanosheets: An Effective Way to Tailor the Physicochemical and Antibacterial Properties of Graphene Film. Advanced Functional Materials 24(16), 2288-2294.

Zhang, S., Li, J., Wang, X., Huang, Y., Zeng, M. and Xu, J. (2014) In situ ion exchange synthesis of strongly coupled Ag@ AgCl/g-C3N4 porous nanosheets as plasmonic photocatalyst for highly efficient visible-light photocatalysis. Acs Applied Materials & Interfaces 6(24), 22116-22125.

Sorokin, A., Seris, J.-L. and Meunier, B. (1995) Efficient oxidative dechlorination and aromatic ring cleavage of chlorinated phenols catalyzed by iron sulfophthalocyanine. Science 268(5214), 1163.

Sze, M.F.F. and McKay, G. (2012) Enhanced mitigation of para-chlorophenol using stratified

activated carbon adsorption columns. Water Research 46(3), 700-710.

Ahlborg, U.G., Thunberg, T.M. and Spencer, H.C. (1980) Chlorinated phenols: occurrence, toxicity, metabolism, and environmental impact. CRC Critical Reviews in Toxicology 7(1), 1-35.

Hirvonen, A., Trapido, M., Hentunen, J. and Tarhanen, J. (2000) Formation of hydroxylated and dimeric intermediates during oxidation of chlorinated phenols in aqueous solution. Chemosphere 41(8), 1211-1218.

Dąbrowski, A., Podkościelny, P., Hubicki, Z. and Barczak, M. (2005) Adsorption of phenolic compounds by activated carbon—a critical review. Chemosphere 58(8), 1049-1070.

Chowdhury, P. and Viraraghavan, T. (2009) Sonochemical degradation of chlorinated organic compounds, phenolic compounds and organic dyes–a review. Science Of The Total Environment 407(8), 2474-2492.

Gimeno, O., Carbajo, M., Beltrán, F.J. and Rivas, F.J. (2005) Phenol and substituted phenols AOPs remediation. Journal Of Hazardous Materials 119(1), 99-108.

Dionysiou, D.D., Khodadoust, A.P., Kern, A.M., Suidan, M.T., Baudin, I. and Laîné, J.-M. (2000) Continuous-mode photocatalytic degradation of chlorinated phenols and pesticides in water using a bench-scale TiO 2 rotating disk reactor. Applied Catalysis B: Environmental 24(3), 139-155.

Ai, Z., Yang, P. and Lu, X. (2005a) Degradation of 4-chlorophenol by a microwave assisted photocatalysis method. Journal Of Hazardous Materials 124(1), 147-152.

Khuzwayo, Z. and Chirwa, E. (2015) Modelling and simulation of photocatalytic oxidation mechanism of chlorohalogenated substituted phenols in batch systems: Langmuir–Hinshelwood approach. Journal Of Hazardous Materials 300, 459-466.

Jensen, F. (2017) Introduction to computational chemistry, John wiley & sons.

De Proft, F. and Geerlings, P. (2001) Conceptual and computational DFT in the study of aromaticity. Chemical Reviews 101(5), 1451-1464.

Di Valentin, C., Pacchioni, G., Selloni, A., Livraghi, S. and Giamello, E. (2005) Characterization of paramagnetic species in N-doped TiO2 powders by EPR spectroscopy and DFT calculations. The Journal of Physical Chemistry B 109(23), 11414-11419.

Li, X., Liu, W. and Ni, J. (2015) Short-cut synthesis of tri-titanate nanotubes using nano-anatase: Mechanism and application as an excellent adsorbent. Microporous And Mesoporous Materials 213, 40-47.

Satterfield, C.N. (1970) Mass transfer in heterogeneous catalysis, The MIT Press.

Liu, W., Ni, J. and Yin, X. (2014) Synergy of photocatalysis and adsorption for simultaneous removal of Cr (VI) and Cr (III) with TiO 2 and titanate nanotubes. Water Research 53, 12-25.

Liu, W., Zhao, X., Borthwick, A.G., Wang, Y. and Ni, J. (2015) Dual-enhanced photocatalytic activity of Fe-deposited titanate nanotubes used for simultaneous removal of As (III) and As (V). Acs Applied Materials & Interfaces 7(35), 19726-19735.

Guo, C., Xu, J., Wang, S., Zhang, Y., He, Y. and Li, X. (2013) Photodegradation of sulfamethazine in an aqueous solution by a bismuth molybdate photocatalyst. Catalysis Science & Technology 3(6), 1603-1611.

154

Frisch, M.J., Trucks, G.W., Schlegel, H.B., Scuseria, G.E., Robb, M.A., Cheeseman, J.R., Montgomery, J.A., Vreven, T., Kudin, K.N., Burant, J.C., Millam, J.M., Iyengar, S.S., Tomasi, J., Barone, V., Mennucci, B., Cossi, M., Scalmani, G., Rega, N., Petersson, G.A., Nakatsuji, H., Hada, M., Ehara, M., Toyota, K., Fukuda, R., Hasegawa, J., Ishida, M., Nakajima, T., Honda, Y., Kitao, O., Nakai, H., Klene, M., Li, X., Knox, J.E., Hratchian, H.P., Cross, J.B., Bakken, V., Adamo, C., Jaramillo, J., Gomperts, R., Stratmann, R.E., Yazyev, O., Austin, A.J., Cammi, R., Pomelli, C., Ochterski, J.W., Ayala, P.Y., Morokuma, K., Voth, G.A., Salvador, P., Dannenberg, J.J., Zakrzewski, V.G., Dapprich, S., Daniels, A.D., Strain, M.C., Farkas, O., Malick, D.K., Rabuck, A.D., Raghavachari, K., Foresman, J.B., Ortiz, J.V., Cui, Q., Baboul, A.G., Clifford, S., Cioslowski, J., Stefanov, B.B., Liu, G., Liashenko, A., Piskorz, P., Komaromi, I., Martin, R.L., Fox, D.J., Keith, T., Laham, A., Peng, C.Y., Nanayakkara, A., Challacombe, M., Gill, P.M.W., Johnson, B., Chen, W., Wong, M.W., Gonzalez, C. and Pople, J.A. (2003) Gaussian 03, Revision C.02.

Parr, R.G. and Yang, W.T. (1984) Density Functional-Approach to the Frontier-Electron Theory of Chemical-Reactivity. Journal Of The American Chemical Society 106(14), 4049-4050.

De Vleeschouwer, F., Van Speybroeck, V., Waroquier, M., Geerlings, P. and De Proft, F. (2007) Electrophilicity and Nucleophilicity Index for Radicals. Organic Letters 9(14), 2721-2724.

Olah, J., Van Alsenoy, C. and Sannigrahi, A.B. (2002) Condensed fukui functions derived from stockholder charges: Assessment of their performance as local reactivity descriptors. Journal of Physical Chemistry A 106(15), 3885-3890.

Yang, H.G., Sun, C.H., Qiao, S.Z., Zou, J., Liu, G., Smith, S.C., Cheng, H.M. and Lu, G.Q. (2008) Anatase TiO2 single crystals with a large percentage of reactive facets. Nature 453(7195), 638-641.

Sun, X. and Li, Y. (2003) Synthesis and characterization of ion-exchangeable titanate nanotubes. Chemistry–A European Journal 9(10), 2229-2238.

Liu, W., Wang, T., Borthwick, A.G., Wang, Y., Yin, X., Li, X. and Ni, J. (2013) Adsorption of Pb 2+, Cd 2+, Cu 2+ and Cr 3+ onto titanate nanotubes: Competition and effect of inorganic ions. Science Of The Total Environment 456, 171-180.

Hua, S., Yu, X., Li, F., Duan, J., Ji, H. and Liu, W. (2017) Hydrogen titanate nanosheets with both adsorptive and photocatalytic properties used for organic dyes removal. Colloids and Surfaces A: Physicochemical and Engineering Aspects 516, 211-218.

Chen, Y.-L., Hu, Z.-A., Chang, Y.-Q., Wang, H.-W., Zhang, Z.-Y., Yang, Y.-Y. and Wu, H.-Y. (2011) Zinc oxide/reduced graphene oxide composites and electrochemical capacitance enhanced by homogeneous incorporation of reduced graphene oxide sheets in zinc oxide matrix. The Journal of Physical Chemistry C 115(5), 2563-2571.

Wen, P., Itoh, H., Tang, W. and Feng, Q. (2007) Single nanocrystals of anatase-type TiO2 prepared from layered titanate nanosheets: Formation mechanism and characterization of surface properties. Langmuir 23(23), 11782-11790.

Brunauer, S., Deming, L.S., Deming, W.E. and Teller, E. (1940) On a theory of the van der Waals adsorption of gases. Journal Of The American Chemical Society 62(7), 1723-1732.

Thommes, M., Kaneko, K., Neimark, A.V., Olivier, J.P., Rodriguez-Reinoso, F., Rouquerol, J. and

Sing, K.S. (2015) Physisorption of gases, with special reference to the evaluation of surface area and pore size distribution (IUPAC Technical Report). Pure and Applied Chemistry 87(9-10), 1051-1069.

Yu, J., Jimmy, C.Y., Leung, M.K.-P., Ho, W., Cheng, B., Zhao, X. and Zhao, J. (2003) Effects of acidic and basic hydrolysis catalysts on the photocatalytic activity and microstructures of bimodal mesoporous titania. Journal Of Catalysis 217(1), 69-78.

Turki, A., Kochkar, H., Guillard, C., Berhault, G. and Ghorbel, A. (2013) Effect of Na content and thermal treatment of titanate nanotubes on the photocatalytic degradation of formic acid. Applied Catalysis B: Environmental 138, 401-415.

Ma, J., Li, F., Qian, T., Liu, H., Liu, W. and Zhao, D. (2017) Natural organic matter resistant powder activated charcoal supported titanate nanotubes for adsorption of Pb (II). Chemical Engineering Journal 315, 191-200.

Wang, S., Sun, H., Ang, H.-M. and Tadé, M. (2013) Adsorptive remediation of environmental pollutants using novel graphene-based nanomaterials. Chemical Engineering Journal 226, 336-347.

Jin, Z., Wang, X., Sun, Y., Ai, Y. and Wang, X. (2015) Adsorption of 4-n-nonylphenol and bisphenol-A on magnetic reduced graphene oxides: a combined experimental and theoretical studies. Environmental Science & Technology 49(15), 9168-9175.

Yu, H., Yu, J., Cheng, B. and Zhou, M. (2006) Effects of hydrothermal post-treatment on microstructures and morphology of titanate nanoribbons. Journal Of Solid State Chemistry 179(2), 349-354.

Lee, C.-K., Wang, C.-C., Lyu, M.-D., Juang, L.-C., Liu, S.-S. and Hung, S.-H. (2007) Effects of sodium content and calcination temperature on the morphology, structure and photocatalytic activity of nanotubular titanates. Journal Of Colloid And Interface Science 316(2), 562-569.

Kim, S., Kim, M., Kim, Y.K., Hwang, S.-H. and Lim, S.K. (2014b) Core–shell-structured carbon nanofiber-titanate nanotubes with enhanced photocatalytic activity. Applied Catalysis B: Environmental 148, 170-176.

Zhang, S., Li, J., Zeng, M., Zhao, G., Xu, J., Hu, W. and Wang, X. (2013) In situ synthesis of water-soluble magnetic graphitic carbon nitride photocatalyst and its synergistic catalytic performance. Acs Applied Materials & Interfaces 5(23), 12735-12743.

Zhang, S., Li, J., Wang, X., Huang, Y., Zeng, M. and Xu, J. (2015) Rationally designed 1D Ag@ AgVO 3 nanowire/graphene/protonated gC 3 N 4 nanosheet heterojunctions for enhanced photocatalysis via electrostatic self-assembly and photochemical reduction methods. Journal of Materials Chemistry A 3(18), 10119-10126.

Liu, W., Cai, Z., Zhao, X., Wang, T., Li, F. and Zhao, D. (2016b) High-capacity and photoregenerable composite material for efficient adsorption and degradation of phenanthrene in water. Environmental science & technology 50(20), 11174-11183.

Zhao, D., Yang, X., Chen, C. and Wang, X. (2013) Enhanced photocatalytic degradation of methylene blue on multiwalled carbon nanotubes–TiO 2. Journal Of Colloid And Interface Science 398, 234-239.

Kim, H.-i., Moon, G.-h., Monllor-Satoca, D., Park, Y. and Choi, W. (2011) Solar photoconversion

using graphene/TiO2 composites: nanographene shell on TiO2 core versus TiO2 nanoparticles on graphene sheet. The Journal of Physical Chemistry C 116(1), 1535-1543.

Stankovich, S., Dikin, D.A., Dommett, G.H., Kohlhaas, K.M., Zimney, E.J., Stach, E.A., Piner, R.D., Nguyen, S.T. and Ruoff, R.S. (2006) Graphene-based composite materials. Nature 442(7100), 282-286.

Cao, J., Luo, B., Lin, H., Xu, B. and Chen, S. (2012) Visible light photocatalytic activity enhancement and mechanism of AgBr/Ag 3 PO 4 hybrids for degradation of methyl orange. Journal Of Hazardous Materials 217, 107-115.

Ishibashi, K.-i., Fujishima, A., Watanabe, T. and Hashimoto, K. (2000) Detection of active oxidative species in TiO2 photocatalysis using the fluorescence technique. Electrochemistry Communications 2(3), 207-210.

Huang, G., Zhang, S., Xu, T. and Zhu, Y. (2008) Fluorination of ZnWO4 photocatalyst and influence on the degradation mechanism for 4-chlorophenol. Environ. Sci. Technol 42(22), 8516-8521.

Du, P., Zhao, H., Liu, C., Huang, Q. and Cao, H. (2016) Transformation and products of captopril with humic constituents during laccase-catalyzed oxidation: role of reactive intermediates. Water Research 106, 488-495.

Ai, Z.H., Yang, P. and Lu, X.H. (2005b) Degradation of 4-chlorophenol by a microwave assisted photocatalysis method. Journal Of Hazardous Materials 124(1-3), 147-152.

Johnson, S.K., Houk, L.L., Feng, J.R., Houk, R.S. and Johnson, D.C. (1999) Electrochemical incineration of 4-chlorophenol and the identification of products and intermediates by mass spectrometry. Environmental Science & Technology 33(15), 2638-2644.

Cheng, Y., Sun, H., Jin, W. and Xu, N. (2007) Photocatalytic degradation of 4-chlorophenol with combustion synthesized TiO2 under visible light irradiation. Chemical Engineering Journal 128(2-3), 127-133.

Zhao, J., Zhang, Y., Quan, X. and Chen, S. (2010) Enhanced oxidation of 4-chlorophenol using sulfate radicals generated from zero-valent iron and peroxydisulfate at ambient temperature. Separation And Purification Technology 71(3), 302-307.

Bavykin, D.V., Friedrich, J.M., Lapkin, A.A. and Walsh, F.C. (2006b) Stability of aqueous suspensions of titanate nanotubes. Chemistry Of Materials 18(5), 1124-1129.

Ahmaruzzaman, M., 2008. Adsorption of phenolic compounds on low-cost adsorbents: A review. Sci Adv. Colloid Interface Sci. 143(1-2), 48-67.

Ai, Z.H., Yang, P. and Lu, X.H., 2005. Degradation of 4-chlorophenol by a microwave assisted photocatalysis method. J. Hazard. Mater. 124(1-3), 147-152.

Aksu, Z. and Yener, J., 2001. A comparative adsorption/biosorption study of mono-chlorinated phenols onto various sorbents. Waste Manage. 21(8), 695-702.

Barrera-Diaz, C.E., Lugo-Lugo, V. and Bilyeu, B., 2012. A review of chemical, electrochemical and biological methods for aqueous Cr(VI) reduction. J. Hazard. Mater. 223, 1-12.

Bavykin, D.V., Friedrich, J.M. and Walsh, F.C., 2006. Protonated titanates and TiO2 nanostructured materials: Synthesis, properties, and applications. Adv. Mater. 18(21), 2807-2824.

Brunauer, S., Deming, L.S., Deming, W.E. and Teller, E., 1940. On a theory of the van der Waals adsorption of gases. J. Am. Chem. Soc. 62(7), 1723-1732.

Chen, Q., Zhou, W.Z., Du, G.H. and Peng, L.M., 2002. Trititanate nanotubes made via a single alkali treatment. Adv. Mater. 14(17), 1208-1211.

Cheng, Y., Sun, H., Jin, W. and Xu, N., 2007. Photocatalytic degradation of 4-chlorophenol with combustion synthesized TiO2 under visible light irradiation. Chem. Eng. J. 128(2-3), 127-133.

Correia, V.M., Stephenson, T. and Judd, S.J., 1994. Characterization of textile wastewaters-A review. Environ. Technol. 15(10), 917-929.

Costa, M., 1997. Toxicity and carcinogenicity of Cr(VI) in animal models and humans. Crit. Rev. Toxicol. 27(5), 431-442.

Crittenden, J.C., Liu, J.B., Hand, D.W. and Perram, D.L., 1997. Photocatalytic oxidation of chlorinated hydrocarbons in water. Water Res. 31(3), 429-438.

Daghrir, R., Drogui, P. and Robert, D., 2013. Modified TiO2 for environmental photocatalytic applications: A review. Ind. Eng. Chem. Res. 52(10), 3581-3599.

Doong, R.A., Chen, C.H., Maithreepala, R.A. and Chang, S.M., 2001. The influence of pH and cadmium sulfide on the photocatalytic degradation of 2-chlorophenol in titanium dioxide suspensions. Water Res. 35(12), 2873-2880.

Edwards, S.J. and Kjellerup, B.V., 2013. Applications of biofilms in bioremediation and biotransformation of persistent organic pollutants, pharmaceuticals/personal care products, and heavy metals. Appl. Microbiol. Biot. 97(23), 9909-9921.

Fan, X., Chen, X., Zhu, S., Li, Z., Yu, T., Ye, J. and Zou, Z., 2008. The structural, physical and photocatalytic properties of the mesoporous Cr-doped TiO2. J. Mol. Catal. A-Chem. 284(1-2), 155-160.

Gu, L., Wang, J., Cheng, H., Du, Y. and Han, X., 2012. Synthesis of nano-sized anatase TiO2 with reactive {001} facets using lamellar protonated titanate as precursor. Chem. Commun. 48(55), 6978-6980.

He, D., Guan, X., Ma, J., Yang, X. and Cui, C., 2010. Influence of humic acids of different origins on oxidation of phenol and chlorophenols by permanganate. J. Hazard. Mater. 182(1-3), 681-688.

He, X., Nie, X., Wang, Z., Cheng, Z., Li, K., Li, G., Wong, M.H., Liang, X. and Tsui, M.T.K., 2011. Assessment of typical pollutants in waterborne by combining active biomonitoring and integrated biomarkers response. Chemosphere 84(10), 1422-1431.

Hou, Y., Li, X., Zou, X., Quan, X. and Chen, G., 2009. Photoeletrocatalytic activity of a Cu2O-loaded self-organized highly oriented TiO2 nanotube array electrode for 4-chlorophenol degradation. Environ. Sci. Technol. 43(3), 858-863.

Huang, L., Chai, X., Quan, X., Logan, B.E. and Chen, G., 2012. Reductive dechlorination and mineralization of pentachlorophenol in biocathode microbial fuel cells. Bioresource Technol. 111, 167-174.

Johnson, S.K., Houk, L.L., Feng, J.R., Houk, R.S. and Johnson, D.C., 1999. Electrochemical incineration of 4-chlorophenol and the identification of products and intermediates by mass

spectrometry. Environ. Sci. Technol. 33(15), 2638-2644.

Kasuga, T., Hiramatsu, M., Hoson, A., Sekino, T. and Niihara, K., 1999. Titania nanotubes prepared by chemical processing. Adv. Mater. 11(15), 1307-+.

Kim, S. and Choi, W., 2005. Visible-light-induced photocatalytic degradation of 4-chlorophenol and phenolic compounds in aqueous suspension of pure titania: Demonstrating the existence of a surface-complex-mediated path. J. Phys. Chem. B 109(11), 5143-5149.

Ku, Y., Leu, R.M. and Lee, K.C., 1996. Decomposition of 2-chlorophenol in aqueous solution by UV irradiation with the presence of titanium dioxide. Water Res. 30(11), 2569-2578.

Liu, W., Chen, H., Borthwick, A.G.L., Han, Y. and Ni, J., 2013a. Mutual promotion mechanism for adsorption of coexisting Cr(III) and Cr(VI) onto titanate nanotubes. Chem. Eng. J. 232, 228-236.

Liu, W., Ni, J. and Yin, X., 2014a. Synergy of photocatalysis and adsorption for simultaneous removal of Cr(VI) and Cr(III) with TiO2 and titanate nanotubes. Water Res. 53, 12-25.

Liu, W., Sun, W., Borthwick, A.G.L. and Ni, J., 2013b. Comparison on aggregation and sedimentation of titanium dioxide, titanate nanotubes and titanate nanotubes-TiO2: Influence of pH, ionic strength and natural organic matter. Colloids Surf. A 434, 319-328.

Liu, W., Sun, W., Han, Y., Ahmad, M. and Ni, J., 2014b. Adsorption of Cu(II) and Cd(II) on titanate nanomaterials synthesized via hydrothermal method under different NaOH concentrations: Role of sodium content. Colloids Surf. A 452, 138-147.

Liu, W., Wang, T., Borthwick, A.G.L., Wang, Y., Yin, X., Li, X. and Ni, J., 2013c. Adsorption of Pb2+, Cd2+, Cu2+ and Cr3+ onto titanate nanotubes: Competition and effect of inorganic ions. Sci. Total. Environ. 456, 171-180.

Liu, W., Zhao, X., Borthwick, A.G.L., Wang, Y. and Ni, J., 2015. Dual-enhanced photocatalytic activity of Fe-deposited titanate nanotubes used for simultaneous removal of As(III) and As(V). ACS Appl. Mater. Interfaces 7(35), 19726-19735.

Liu, W., Zhao, X., Wang, T., Zhao, D. and Ni, J., 2016. Adsorption of U(VI) by multilayer titanate nanotubes: Effects of inorganic cations, carbonate and natural organic matter. Chem. Eng. J. 286, 427-435.

Lopez, R. and Gomez, R., 2012. Band-gap energy estimation from diffuse reflectance measurements on sol-gel and commercial TiO2: a comparative study. J. Sol-gel. Sci. Techn. 61(1), 1-7.

Ma, R.Z., Fukuda, K., Sasaki, T., Osada, M. and Bando, Y., 2005. Structural features of titanate nanotubes/nanobelts revealed by Raman, X-ray absorption fine structure and electron diffraction characterizations. J. Phys. Chem. B 109(13), 6210-6214.

Niu, G., Liu, W., Wang, T. and Ni, J., 2013. Absorption of Cr(VI) onto amino-modified titanate nanotubes using 2-Bromoethylamine hydrobromide through SN2 reaction. J. Colloid Interface Sci. 401, 133-140.

Qiu, R., Zhang, D., Diao, Z., Huang, X., He, C., Morel, J.-L. and Xiong, Y., 2012. Visible light induced photocatalytic reduction of Cr(VI) over polymer-sensitized TiO2 and its synergism with phenol oxidation. Water Res. 46(7), 2299-2306.

Quintelas, C., Sousa, E., Silva, F., Neto, S. and Tavares, T., 2006. Competitive biosorption of ortho-

cresol, phenol, chlorophenol and chromium(VI) from aqueous solution by a bacterial biofilm supported on granular activated carbon. Process Biochem. 41(9), 2087-2091.

Rizzo, L., Meric, S., Kassinos, D., Guida, M., Russo, F. and Belgiorno, V., 2009. Degradation of diclofenac by TiO2 photocatalysis: UV absorbance kinetics and process evaluation through a set of toxicity bioassays. Water Res. 43(4), 979-988.

Satterfield, C.N., 1970. Mass Transfer in Heterogeneous Catalysis. MIT Press, Cambridge, MA, UK.

Scott, J.P. and Ollis, D.F., 1995. Integration of chemical and biological oxidation processes for water treatment: Review and recommendations. Environ. Prog. 14(2), 88-103.

Serpone, N., Lawless, D. and Khairutdinov, R., 1995. Size effects on the photophysical properties of colloidal anatase TiO2 particles - Size quantization or direct transitions in this indirect semiconductor. J. Phys. Chem. 99(45), 16646-16654.

Sorokin, A., Seris, J.L. and Meunier, B., 1995. Efficient oxidative dechlorination and aromatic ring-cleavage of chlorinated phenols catalyzed by iron sulfophthalocyanine. Science 268(5214), 1163-1166.

Sun, X.M. and Li, Y.D., 2003. Synthesis and characterization of ion-exchangeable titanate nanotubes. Chem.-Eur. J. 9(10), 2229-2238.

Sze, M.F.F. and McKay, G., 2012. Enhanced mitigation of para-chlorophenol using stratified activated carbon adsorption columns. Water Res. 46(3), 700-710.

Tripathi, M. and Garg, S.K., 2014. Dechlorination of chloroorganics, decolorization, and simultaneous bioremediation of Cr6+ from real tannery effluent employing indigenous Bacillus cereus isolate. Environ. Sci. Pollut. R 21(7), 5227-5241.

Tripathi, M., Vikram, S., Jain, R.K. and Garg, S.K., 2011. Isolation and growth characteristics of chromium(VI) and pentachlorophenol tolerant bacterial isolate from treated tannery effluent for its possible use in simultaneous bioremediation. Indian J. Microbiol. 51(1), 61-69.

Valente, J.P.S., Padilha, P.M. and Florentino, A.O., 2006. Studies on the adsorption and kinetics of photodegradation of a model compound for heterogeneous photocatalysis onto TiO2. Chemosphere 64(7), 1128-1133.

Vinu, R. and Madras, G., 2008. Kinetics of simultaneous photocatalytic degradation of phenolic compounds and reduction of metal ions with nano-TiO2. Environ. Sci. Technol. 42(3), 913-919.

Wang, L., Liu, W., Wang, T. and Ni, J., 2013a. Highly efficient adsorption of Cr(VI) from aqueous solutions by amino-functionalized titanate nanotubes. Chem. Eng. J. 225, 153-163.

Wang, S.L., Chen, C.C., Tzou, Y.M., Hsu, C.L., Chen, J.H. and Lin, C.F., 2009. A mechanism study of light-induced Cr(VI) reduction in an acidic solution. J. Hazard. Mater. 164(1), 223-228.

Wang, T., Liu, W., Xiong, L., Xu, N. and Ni, J., 2013b. Influence of pH, ionic strength and humic acid on competitive adsorption of Pb(II), Cd(II) and Cr(III) onto titanate nanotubes. Chem. Eng. J. 215, 366-374.

Wang, T., Liu, W., Xu, N. and Ni, J., 2013c. Adsorption and desorption of Cd(II) onto titanate nanotubes and efficient regeneration of tubular structures. J. Hazard. Mater. 250, 379-386.

Wang, Y., Liu, W., Wang, T. and Ni, J., 2015. Arsenate adsorption onto Fe-TNTs prepared by a

novel water-ethanol hydrothermal method: Mechanism and synergistic effect. J. Colloid Interface Sci. 440, 253-262.

Xiong, L., Chen, C., Chen, Q. and Ni, J., 2011. Adsorption of Pb(II) and Cd(II) from aqueous solutions using titanate nanotubes prepared via hydrothermal method. J. Hazard. Mater. 189(3), 741-748.

Yang, H.G., Sun, C.H., Qiao, S.Z., Zou, J., Liu, G., Smith, S.C., Cheng, H.M. and Lu, G.Q., 2008. Anatase TiO2 single crystals with a large percentage of reactive facets. Nature 453(7195), 638-641.

Yin, X., Liu, W. and Ni, J., 2014. Removal of coexisting Cr(VI) and 4-chlorophenol through reduction and Fenton reaction in a single system. Chem. Eng. J. 248, 89-97.

Yu, J.G., Yu, H.G., Cheng, B. and Trapalis, C., 2006. Effects of calcination temperature on the microstructures and photocatalytic activity of titanate nanotubes. J. Mol. Catal. A-Chem. 249(1-2), 135-142.

Zhang, J., Zhang, Y., Lei, Y. and Pan, C., 2011. Photocatalytic and degradation mechanisms of anatase TiO2: a HRTEM study. Catal. Sci. Technol. 1(2), 273-278.

Zhang, S.M., Chen, Y.Y., Yu, Y., Wu, H.H., Wang, S.R., Zhu, B.L., Huang, W.P. and Wu, S.H., 2008. Synthesis, characterization of Cr-doped TiO2 nanotubes with high photocatalytic activity. J. Nanopart. Res. 10(5), 871-875.

Zhao, J., Zhang, Y., Quan, X. and Chen, S., 2010. Enhanced oxidation of 4-chlorophenol using sulfate radicals generated from zero-valent iron and peroxydisulfate at ambient temperature. Sep. Purif. Technol. 71(3), 302-307.

Zhu, J.F., Deng, Z.G., Chen, F., Zhang, J.L., Chen, H.J., Anpo, M., Huang, J.Z. and Zhang, L.Z., 2006. Hydrothermal doping method for preparation of Cr3+-TiO2 photocatalysts with concentration gradient distribution of Cr3+. Appl. Catal. B-Environ 62(3-4), 329-335.